ABSTRACT

Title of dissertation: LASER PULSE DRIVEN TERAHERTZ (THz) GENERATION IN INHOMOGENEOUS PLASMAS

Chenlong Miao, Doctor of Philosophy, 2016

Dissertation directed by: Professor Thomas M. Antonsen Jr.
Department of Electrical and Computer Engineering

Intense, short laser pulses propagating through inhomogeneous plasmas can ponderomotively drive terahertz (THz) radiation. Theoretical analysis and full format PIC simulations are conducted to investigate two mechanisms of laser pulse driven terahertz generation: (i) a resonant transition radiation (RTR) mechanism occurring as a pulse crosses a plasma boundary and (ii) a slow wave phase matching mechanism (SWPM) that occurs in corrugated plasma channels. These studies are the first to investigate ponderomotively driven THz self-consistently in the interesting situations in which the interaction occurs over a scale many wavelengths long.

For the resonant transition radiation mechanism, both theory and simulation results show the conical THz emission originates in regions of varying density and covers a broad spectrum with maximum frequency close to the maximum plasma frequency. In the case of a sharp vacuum-plasma boundary, the radiation is generated symmetrically at the plasma entrance and exit, and its properties are independent of plasma density when the density exceeds a characteristic value determined by the

product of the plasma frequency and the laser pulse duration. For a diffuse vacuum-plasma boundary, the emission from the plasma entrance and exit is asymmetric: increasing and decreasing density ramps enhance and diminish the radiated energy, respectively. Enhancements by a factor of 50 are found, and simulations show that a 1.66 J, 50 fs driver pulse can generate $\sim$400 μJ of THz radiation in a 1.2 mm increasing density ramp. We present a model that attributes this effect to a plasma resonance process in the density ramp. The results from the model match those of the simulations for ramp lengths less than 600 μm. For longer ramps for which simulations are too time consuming, the model shows that the amount of radiation reaches a maximum at a ramp length determined by collisional absorption.

For the slow wave phase matching mechanism, excitation of terahertz radiation by the interaction of an ultra-short laser pulse and the fields of a miniature, corrugated plasma waveguide is considered. Plasma structures of this type have been realized experimentally, and they can support electromagnetic (EM) channel modes with properties that allow for radiation generation. In particular, the modes have subluminal field components, thus allowing phase matching between the generated THz modes and the ponderomotive potential of the laser pulse. Theoretical analysis and full format PIC simulations are conducted. We find THz generated by this slow wave phase matching mechanism is characterized by lateral emission and a coherent, narrow band, tunable spectrum with relatively high power and conversion efficiency. We investigated two different types of channels, and a range of realistic laser pulses and plasma profile parameters were considered with the goal of increasing the conversion of optical energy to THz radiation. We find high laser intensities strongly

modify the THz spectrum by exciting higher order channel modes. Enhancement of a specific channel mode can be realized by using an optimum pulse duration and plasma density. As an example, simulation results show a fixed driver pulse (0.55 J) with spot size of 15 μm and pulse duration of 15 fs excites approximately 37.8 mJ of THz radiation in a 1.5 cm corrugated plasma waveguide with on axis average density of 1.4×10^{18} cm^{-3}, conversion efficiency exceeding 8% can be achieved in this case.

LASER PULSE DRIVEN TERAHERTZ (THz) GENERATION IN INHOMOGENEOUS PLASMAS

by

Chenlong Miao

Dissertation submitted to the Faculty of the Graduate School of the
University of Maryland, College Park in partial fulfillment
of the requirements for the degree of
Doctor of Philosophy
2016

Advisory Committee:
Professor Thomas M. Antonsen Jr., Chair/Advisor
Professor Phillip A. Sprangle
Professor Mario Dagenais
Professor Ki-Yong Kim
Professor Adil B. Hassam

Dedication

Dedicated to my parents for their support and my grandpa.

Acknowledgments

I owe my gratitude to all the people who have supported and helped me through out the years of pursing my Ph.D. degree and without them this thesis would never be possible.

First and foremost, I would like to thank my academic advisor, Dr. Antonsen for helping and inspiring me a lot during the past five years at Maryland. Every time I had difficulty in figuring out my research problems or felt frustrated about my naive mistakes in simulations, his door always remains open to me and he is always there to help me out and encourage me. I can't count how many times I stepped into his office in the middle of day and interrupted him, but he is patient as always. Dr. Antonsen is a person I respect and admire a lot, his experience and intelligence allows him to come up with new ideas and solutions very quickly and he can always explain them to me in a very clear way. It has been magic every time he brought some pages of solutions for the problem I was stuck on for days, shortly after I sought his help. In addition, he always makes sure that I improve my speaking and writing skills in English by sparing his precious time, talking with me, and revising my manuscripts patiently. Dr. Antonsen had a great impact on me not only by advising me in applied physics but also teaching me how to be a responsible person in complicated situations. I also appreciate him a lot for tolerating me leaving early on many Fridays to drive to meet my girlfriend in Durham.

I appreciate John Palastro for his frequent help during my first three years in the group and even now after his leaving to the Naval Research Lab, I still bother

him occasionally, and he always responsed very quickly. He makes sure I am in good shape for my research and it would take much longer without his help from time to time. He also taught me how to speak up in a conference and was always there encouraging me. I am grateful for him spending a lot of time dealing with my research and treating me as a friend.

I would also like to thank Dr. Sprangle for allowing me to work with him for some time and asking him a lot of questions. He is another person I admire a lot. He is very active in work but very kind and approachable in life. He even invited me to his farm and it was really a good time. I will remember the beer called La Fin Du Monde. I also want to to thank Dr. Gordon and Dr. Ting at NRL for allowing me to talk with them and help me with my research.

I appreciate the committee members: Dr. Thomas Antonsen, Dr. Phillip Sprangle, Dr. Mario Dagenais, Dr. Ki-Yong Kim and Dr. Adil Hassam for being so kind to spend their precious hours for my PhD work.

I would like to thank my officemates Luke, Thomas, Wenxi Jasmine, Mark, Shane, Josh and Zach for the precious months and years we spent together. I still remember the first day I arrived at the office, and they invited me out to the Barking Dog, which now is already memory in downtown College Park. I will never forget our group BBQs and the regular group get together even after graduation. We had a lot of good talk in the office and we helped each other in research. I also want to thank my collaborators from Dr. Milchberg's group, Sung, Andy and George for talking with me frequently about their experimental progress and it was always a great time with them at the major conferences.

I also appreciate the accompany and support from my girlfriend Yilin. It is always a comfort to know that there is someone who can share the same thoughts, both happiness and struggle. She motivates me a lot and encourages me to be a better person.

Last but certainly not the least, I appreciate my parents for their selfless and strong support for pursing what I like. We have not seen each other often since I left home for my undergraduate study. The situation became worse five years ago after I travelled abroad to the states for my graduate study. I only met them three times since then, and they never complained about it even though I was away during the traditional family reunion festivals. I feel like I owe them a lot, but they are always there on the phone, trying to encourage me, and help me out of any situation. I am grateful for their patience and unconditional love for me, and I will try my best to make them proud.

To complete it, I would also take this opportunity to thank all my friends in life. I owe my apology to anyone who is not listed here but certainly they are important for my graduate experience that I will cherish forever.

Table of Contents

List of Tables viii

List of Figures ix

List of Abbreviations xv

1 Introduction 1
- 1.1 Terahertz Sources Driven by Intense Laser Pulses . . . 1
  - 1.1.1 Existing Terahertz Sources and Recent Advances . . . 2
  - 1.1.2 Laser Driven: Ponderomotive Driver . . . 4
  - 1.1.3 Transition Radiation at the Plasma Vacuum Interface . . . 7
  - 1.1.4 Axially Modulated Plasma Waveguides . . . 9
- 1.2 Models and Simulation Techniques . . . 12
  - 1.2.1 Particle In Cell (PIC) Method . . . 12
  - 1.2.2 TurboWAVE . . . 14
  - 1.2.3 System Setup and Radiation Diagnostics . . . 14
- 1.3 Structure of the Thesis . . . 15

2 Terahertz Generation via Resonant Transition Radiation (RTR) in A Plasma Density Gradient 20
- 2.1 Overview . . . 20
- 2.2 THz generation via Transition Radiation at a sharp vacuum-plasma interface . . . 22
- 2.3 THz generation via Resonant Transition Radiation in diffuse plasma profiles . . . 35
- 2.4 Conclusions . . . 53
- 2.5 Appendix A: NUMERICAL METHOD FOR EQUATION (2.5) . . . 54

3 High-Power Tunable THz Generation in Corrugated Plasma Waveguides 58
- 3.1 Overview . . . 58
- 3.2 Excitation of THz modes in corrugated plasma channels . . . 60
  - 3.2.1 Ponderomotive Driver . . . 60
  - 3.2.2 Corrugated Plasma Channels . . . 63

3.2.3 Dispersion Relation and Mode Excitation 64
3.3 Simulation Results 67
3.3.1 Radial eigenmodes 67
3.3.2 PIC simulation results 68
3.3.2.1 THz Mode Excitation 68
3.3.2.2 Dependence on Plasma Density 74
3.3.2.3 Dependence on Laser Intensity 74
3.3.2.4 Dependence on Laser Pulse Duration 78
3.3.2.5 Scaling with Channel Length 79
3.3.2.6 Other parameters 91
3.4 Conclusions and Discussions 95
3.5 Appendix A: CALCULATING THE RADIAL EIGENMODES 98

4 Summary and Conclusions 103

Bibliography 108

List of Tables

3.1 Exact values of numerically calculated k_c and estimation from Eq. (3.6) for different radial modes. 68
3.2 Comparison of generated THz energy for different laser intensities and density profiles. 97

List of Figures

1.1 (a) Electrons only quiver at the laser frequency since the laser intensity is uniform transversely, i.e., $F_p = 0$. Each of the red curves represents the electron trajectory at a different transverse initial position. (b) For a laser pulse with a transverse Gaussian shape, the electrons quiver at the laser frequency as well as responding to the low frequency ponderomotive potential. The blue line indicates the slow varying trajectory of the electron. 8

2.1 (a) Diagram of simulation set up for transition radiation at the vacuum plasma boundary. The diagnostic box is set outside the plasma channel. The Poynting flux through each surface is calculated. (b) A snap shot of the Poynting flux $E_x B_y$ in PIC simulations using TurboWAVE. The transition radiation is generated at both boundaries when the laser travels through the plasma from left to right. 23

2.2 (a) Comparison of radiated spectral density. Shown are theoretical values (Eq. (2.11), black solid), and simulations using TuroWAVE for plasma length $L = 500$ μm (blue dashed) and $L = 100$ μm (green dashed). (b) Comparison of emerging radiation angle. Shown are theoretical values (Eq. (2.13), black solid), and simulations for plasma length $L = 500$ μm (blue dashed) and $L = 100$ μm (green dashed). Simulation results for plasma with a larger transverse size $W = 180$ μm (magenta dashed) are also provided in both figures. 30

2.3 (a) Radiated energy versus electron density (2D theory: line; TurboWAVE: squares.). Energy is insensitive to plasma density above 1.5×10^{18} cm^{-3}. (b) Radiation spectra for different plasma densities: (i) 1.5×10^{18} cm^{-3}, (ii) 2.8×10^{18} cm^{-3}, (iii) 4×10^{18} cm^{-3}, (iv) 6×10^{18} cm^{-3}. The red dotted line (v) is the spectrum of the laser envelope $\bar{V}_p$ with arbitrary units. 32

2.4 Scaling of radiated THz energy with laser intensities. The spot size and pulse duration remain the same as 15 μm and 50 fs, respectively. Theory predicts scaling to be $a_0^4/(1+a_0^2)$ based on ponderomotive effect. Simulation results (blue) from TurboWAVE agree with the a_0^4 scaling (red) in the weakly relativistic regime where $a_0 << 1$. The scaling is weaker where $a_0 >> 1$. 33
2.5 Radiated THz energy across the (a) left and (b) lateral diagnostic boundary as shown in Fig. 2.1(a), respectively. 34
2.6 Comparisons of (a) plasma density with sharp step boundaries and (c) plasma density with increasing and decreasing ramps ($\sim$25 μm). Simulation results, radiation spectrum as a function of the longitudinal distance and frequency showing that (b) the step boundary is symmetric while (d) the case with density ramps shows asymmetry. . 36
2.7 Comparisons of radiated spectral density using different increasing ramp lengths at a particular radiation frequency $\omega_1 = 0.6\omega_{p0}$. Shown are simulation results (square), numerical results of our model (diamond) and the scaling theory Eq. (11). Note from Fig. 2.2(a) the corresponding value in the sharp boundary case is $dU'/d\omega = 1.5 \times 10^{-17}$ (J/Hz·m). 37
2.8 Schematic plot for THz generation via resonant transition radiation in the density ramp region. Shown are plasma density profile (blue) and the characteristic solution of the electric field E_r (black). Plasma resonance in the ramp is expected. 38
2.9 Contours for evaluation of the integral in Eq. (2.21) for an increasing (a) and decreasing (b) density ramp. 43
2.10 THz generation via resonant transition radiation in a diffuse (a) increasing and (b) decreasing density ramp. Shown are numerical result of the electric field described by Eq. (2.5) (real part, blue solid and imaginary part, black dashed), and the electron density profile (red dashed) with a 200 μm ramp length starting at $z = 0$ to $z = 200$ μm . The Poynting flux, described by Eq. (2.8), is also shown (green solid). 45
2.11 Comparison of THz generation in different density ramps. Shown are numerical results of the generated electric field described by Eq. (2.5) in a sharp vacuum-plasma boundary (blue, solid), an upward/increasing density ramp (black dashed) and a downward/decreasing density ramp (green dashed). The density ramp has a 200 μm ramp length between $z = 0$ and $z = 200$ μm. 47

2.12 Comparisons of radiated spectral density between TurboWAVE and the proposed model for different increasing ramp lengths. Shown are TurboWAVE (TW) simulation results (dash, circle marker) and numerical results from the differential equation (DE) based on our developed model (solid) for different ramp lengths up to 3200 μm . Integration over frequency gives the total amount of radiated energy in 2D geometry; for example, the total energy is 0.1375 J/m for ramp length of 1200 μm , which is an enhancement of $\sim$50 times compared with 0.0027 J/m for the sharp boundary case. 48
2.13 (a) Comparisons of Sz (Eq. (2.8)) at a particular radiation frequency $\omega_1 = 0.6\omega_{p0}$ for different increasing ramp lengths. Shown are numerical results of our developed model (solid, cross marker) for different ramp lengths up to 3200 μm. (b) Peak radiation angle (corresponding k_x) agrees with our model $k_{x,peak}c/\omega \sim (c/L_0\omega)^{1/3} << 1$. 50
2.14 Wronskian described by Eq. (2.39) for a 200 μm increasing density ramp. 57

3.1 (a) Diagram of experimental setup for generation of an axially corrugated plasma channel. To create the plasma structures, a modulated cluster density can be used in conjunction with a uniform formation pulse or one can spatially modulate the formation pulse alternatively. (b) Snapshot of an experimentally generated axially modulated plasma channel (only 3 periods are shown here). 61
3.2 False color image of two example electron density profiles generated by Eq. (3.2): (a) a channel with maximum density at lateral edges, with $\delta_1 = \delta = 0.7$, $\overline{n}_1 = 1.3$, $r_c = 30\ \mu m$ and $r_0 = 40\ \mu m$. (b) a channel with maximum density at the center, with $\delta = 0.7$, $\overline{n}_1 = 1.3$, $\delta_1 = 0.1$. Both cut-off radius and channel radius are also modulated as $r_c[\mu m] = 22.5 - 7.5\sin(k_m z)$ and $r_0[\mu m] = r_c + 15$. 64
3.3 Dispersion relation curves of the lowest (fundamental) radial mode of a corrugated channel evaluated by Eq. (3.6) with $n_{00} = 1.4 \times 10^{18}\ cm^{-3}$, $\delta_1 = \delta = 0.9$, $\overline{n}_1 = 3$ and $r_c = 30\ \mu m$. The straight line (red) corresponds to the laser pulse moving at the speed of light, $\omega = k_z c$. 66
3.4 (a) Diagram of simulation set up. The diagnostic box is set outside the plasma channel and the Poynting flux through each surface is calculated. The plasma channel consists of 10 modulation periods with the following parameters: $\lambda_m = 50\ \mu m$, $n_{00} = 1.4 \times 10^{18}\ cm^{-3}$, $\delta_1 = \delta = 0.9$, $\overline{n}_1 = 3$, $r_c = 30\ \mu m$ and $r_0 = 40\ \mu m$. (b) A snap shot of the transverse component of Poynting flux $E_z B_y$ in PIC simulations after the laser propagates through the channel from left to right, with bright and dark streaks indicating lateral THz radiation is generated. 70

3.5 (a) Radiated THz energy across the lateral diagnostic boundary shows two different mechanisms of generating THz. (b) Simulation results of radiated THz spectral density across the lateral diagnostic boundary using the same channel parameters in Fig. 3.4(a) and $a_0 = 0.4$. Besides the low frequency, broad band THz radiation when laser pulse crosses the plasma interface, lateral THz radiation is also observed. (c) Radiated THz spectrum (only channel modes are considered in this plot) shows different channel modes are excited. The frequency of each excited mode matches well with the phase matching condition in Fig. 3.3. 72
3.6 (a) False color image of the spatial and temporal evolution of Poynting flux P_x across the lateral diagnostic boundary from PIC simulations. Lateral THz emission of channel modes is observed. (b) A typical temporal profile of the excited THz mode, with frequency ∼12.5 THz. 73
3.7 (a) THz radiation for different plasma densities. Simulation results include the broad band THz generated by resonant transition radiation (RTR) at the side end of plasma channel and the narrow band THz generated by the slow wave phase matching (SWPM) process as we discussed in this paper. For the latter case, when density is reduced until the optimal density $1.75 \times 10^{17}\ cm^{-3}$, more THz radiation leaks out the channel. (b) Radiated spectral density $dU'/d\omega$ of THz shows that as plasma density decreases, the frequency of excited THz decreases while at the same time, more THz radiation is generated until the optimal density $1.75 \times 10^{17}\ cm^{-3}$ is reached. 75
3.8 Radiated THz spectrum across the lateral diagnostic boundary for different laser intensities (a) $a_0 = 0.2$ (pulse energy 16.7 mJ) (b) $a_0 = 0.8$ (pulse energy 0.267 J) (c) $a_0 = 2.0$ (pulse energy 1.66 J). All other parameters remain the same in the simulation. As laser intensity increases, more THz energy is generated. In addition, high order channel modes are excited as well. 77
3.9 Efficiency $\eta = E_{THz}/\left|\Delta E_{laser}\right|$ for different laser intensities. Same channel parameters as shown in Fig. 3.4(a) are used. For $a_0 < 1$, η is independent of a_0 as expected. However, for $a_0 > 1$, scaling is enhanced since higher order channel modes are excited due to nonlinear currents. 78
3.10 Radiated THz spectrum across the lateral diagnostic boundary for different laser pulse durations (a) 100 fs (b) 30 fs (c) 15 fs. 80
3.11 Displayed is the comparison of radiated spectral density for these pulse durations as shown in Fig. 3.10. 81
3.12 (a) Pulse energy depletion of an initial laser with $a_0 = 2.0$ (0.55 J) during the propagation in a corrugated plasma channel. Simulation result shows that around 80% of the energy stored in the laser pulse is depleted within the propagation distance of 1.5 cm.(b) Scaling of Radiated THz energy versus plasma channel length. 85

3.13 Temporal profiles of on axis magnetic field B_y of the pump laser at the three different locations (initial, 4.5 mm, 7 mm) of the channel as displayed in Fig. 3.16(a) indicate that the front of the laser pulse is preferentially eroded during the interaction with the plasma channel. 87
3.14 (a) Transverse profiles of the magnetic field B_y of the pump laser at the three different locations (initial, 4.5 mm, 7 mm) remain a good Gaussian shape since the pulse is well guided by the channel structure. However, the peak filed on axis increases. (b) Fourier transform of the magnetic field B_y of the pump laser shows spectral modification of the pulse, the central frequency shifts from the initial 375 THz to 331.6 THz within a propagation distance of 7 mm. 88
3.15 Wave action defined in Eq. (3.12) as a 800nm laser pulse with pulse duration of 15 fs, transverse spot size of 15 μm and $a_0 = 2.0$ propagates through the same corrugated plasma channel in Fig. 3.2a. . . . 89
3.16 (a) Investigate THz generation during the pulse propagation in a corrugated plasma channel at three different locations, 0-500 μm (black), 4500-5000 μm (blue), and 7000-7500 μm (red), respectively. (b) Radiated THz energy dU'/dZ at these three different locations. The x axes are shifted to 0-500 μm so that the three simulation results can be aligned. The increase of a_0 explains why more THz is generated during the propagation despite of the same channel length. (c) Radiated spectral density dU'/dω for the corresponding three locations shows that the THz spectrum becomes broader during the propagation. 90
3.17 (a) Pulse energy depletion of an initial laser with $a_0 = 0.4$ (44.5 mJ) during the propagation in a corrugated plasma channel. Simulation result shows that only 10% of the energy stored in the laser pulse is depleted within the propagation distance of 1.5 cm. (b) Scaling of Radiated THz energy versus plasma channel length indicates that only 1.1% of the depleted laser energy is concerted into THz radiation in this case. 92
3.18 False color image of radiated THz spectrum across the lateral diagnostic boundary for two different laser pulses (a) $a_0 = 0.4$ (b) $a_0 = 2.0$. The integral over all boundary locations yields to the total THz spectrum dU'/dz and is also included in the plot (white, dashed). The plasma density profile used in the simulations is shown in Fig. 3.2b and has a local maximum in the center of the channel. Simulation result shows that an ideal narrow band THz spectrum is excited and higher THz energy is preferentially generated in this type of channel. 94
3.19 Nyquist Theory: Cauchy's principle. 100
3.20 $\Phi(0)$ encircles origin (red dot) twice as k_c scans from 0.301 μm to 0.402 μm. The density profile in this case is: $n_{00} = 1.4 \times 10^{18}\ cm^{-3}$, $\delta_1 = \delta = 0.9$, $\overline{n}_1 = 3$, $r_c = 30\ \mu m$ and $r_0 = 40\ \mu m$. 101

3.21 (a) k_c of the fundamental radial mode is found to between 0.301 μm^{-1} and 0.303 μm^{-1}. (b) k_c of the second order radial mode is found to between 0.36 μm^{-1} and 0.37 μm^{-1}. Applying linear interpolation can help narrow the range of k_c and we find $k_c = 0.30195$ μm^{-1} for the first radial mode and $k_c = 0.3638$ μm^{-1} for the second radial mode. . 102

List of Abbreviations

THz	Terahertz Waves
CW	Continuous Waves
OR	Optical Rectification
TW	TurboWAVE
DE	Differential Equation
EM	Electromagnetic
PIC	Particle In Cell
IREAP	Institute for Research in Electronics and Applied Physics
UMD	University of Maryland, College Park
NRL	Naval Research Laboratory
RTR	Resonant Transition Radiation
SWPM	Slow Wave Phase Matching

Chapter 1: Introduction

1.1 Terahertz Sources Driven by Intense Laser Pulses

Terahertz radiation, also known as THz or T-ray, is a sub-millimeter electromagnetic wave with frequencies spanning from 300 GHz to 20 THz (1 mm - 15 μm) [1]. It lies between microwave and infrared in the electromagnetic spectrum. Below the THz frequency, electronics is the dominant paradigm for technology and scientific instrumentation. Above the THz frequency, photonics is the dominant paradigm. Since optics and electronics converge at this widely acknowledged "THz gap" , sources and detectors of electromagnetic radiation have attracted much interest during recent decades. The THz frequency range opens a new frontier for research and development in physics, chemistry, biology, material science and medical imaging. A wide range of new technologies and applications has been proposed and developed including time domain spectroscopy (TDS) [2] , remote detection [3], and medical and biological imaging [4]. One of the most widely used technologies is the millimeter wave/THz scanners [5, 6] used in nearly every airport. The materials of clothing are transparent to THz waves, thus allowing security checking, and causing far fewer radiation effects to the human body compared with X-rays. Other examples include using THz radiation to probe nonlinear effects in materials

[7] since the peak THz field typically exceeds 100 kV/cm, therefore it can be used to measure optical properties with hundred μm resolution since it is non-ionizing electromagnetic radiation. THz can also be employed to induce large transient current, for example, to exceed critical current in the film superconductors [8, 9]. New THz sources can lead to science and technology advances in various areas. Thus THz radiation has attracted much interest as the opportunities for research progress.

1.1.1 Existing Terahertz Sources and Recent Advances

Terahertz radiation sources are now available in both continuous wave (CW) [10, 11] and pulsed form [12, 13]; down to single cycle pulses, with peak power up to Gigawatt levels. Conventional higher power THz pulses can be generated at large accelerator facilities via synchrotron [14] or transition radiation [15]. Such facilities are relatively large and expensive to operate. This motivates the interest in research into small-scale, high efficiency terahertz sources.

Existing small scale THz sources based on laser-solid interaction are limited to μJ/pulse levels due to material damage [16] although the recent discovery using optical rectification (OR) [17–19] in organic crystals can exceed this limit by generating hundreds of μJ max pulse energy. Plasmas, on the other hand, can withhold large amplitude optical pulses, which has led to the consideration of THz generation via laser-plasma interactions [20–22] and THz peak energy of tens of μJ can be achieved.

Research has been actively conducted to investigate THz radiation generation

by laser pulses propagating into plasmas since it was first demonstrated by Hamster et al. [12, 13]. In this case, the source of the radiation is the current driven by the ponderomotive force of a laser pulse at the vacuum plasma interface and the generation of THz radiation is typically minimal. The generated THz pulses via transition radiation in this case and the detected THz pulse properties can be utilized to diagnose the incident optical pulses or partible beams [23, 24]. Many new THz sources based on laser-plasma interactions have been proposed and demonstrated over time. A first example is the transition radiation generated by a laser accelerated electron bunch passing from plasma to vacuum [20, 25–28]. In an experiment reported in Ref. [20], coherent radiation in the range of 0.3-3 THz was produced by this mechanism using nC, femtosecond electron bunches. The THz energy collected within a limited 30 mrad angle was ∼3-5 nJ and was observed to increase quadratically with the bunch charge. A more recent experiment [22], performed with intense laser pulses (up to 5×10^{19} W/cm^2) irradiating thin metal foil targets, resulted in the observation of THz pulses with energies > 436 μJ from a laser driven ion accelerator. A second example is the radiation produced by gas undergoing ionization by two-color laser pulses [29–31]. In these experiments, fundamental and second harmonic optical field, combined with correct relative phase, produce a slow, directed, photoionization current that can drive THz radiation. This mechanism has been shown to routinely produce peak THz energy in excess of 5 μJ with pump pulse energy of tens of mJ. The emission is conical with an angle determined by an optical Cherenkov radiation process [32]. It is well established that the generation of radiation by a laser pulse propagating through a uniform plasma is generally min-

imal. The is because the electromagnetic modes excited have a polarization that doesn't couple to radiation and they are superluminal. In order for these electromagnetic modes to efficiently couple to the driving source which travels at its group velocity, the plasma must be inhomogeneous or a strong background magnetic field is required. A third example is the coherent radiation involving a laser pulse propagating through a plasma channel with an axially periodic density profile [33, 34]. The channel can be viewed as a slow wave structure that supports electromagnetic modes with subluminal phase velocities, and further allows phase matching between the laser driver and the modes, which provides the possibility of high conversion efficiency. Simulation shows THz energy of 6 mJ is generated with a pulse energy of 0.5 J with a depletion length of less than 20 cm [34].

Other schemes to significantly enhance the generated THz radiation include using ultra-short laser pulses propagating through a increasing plasma density gradient [35, 36] or axially modulated plasma channels [37]. Both mechanisms are included and discussed in detail in this thesis. The former involves enhanced transition radiation via plasma resonance in the increasing plasma density gradient, while the latter allows a better phase matching between the generated THz modes and the laser pulse, as well as providing spectrum tunability and high conversion efficiency.

1.1.2 Laser Driven: Ponderomotive Driver

During laser pulse propagation through plasmas, the plasma electrons interact with the laser fields in two ways. First, the electrons quiver at the high laser

frequency. Second, due to the time average of the quiver motion, they experience a low frequency ponderomotive force [38–40]. The force is the gradient of a potential proportional to the square of the envelop of the electric field of the laser. Through this the electrons are pushed out off axis and the plasma wakefields are generated.

To better understand the origin of the ponderomotive force, one can refer to the electron fluid momentum equation of motion in CGS units,

$$\frac{d\boldsymbol{p}}{dt} = -e\left(\boldsymbol{E} + \frac{\boldsymbol{v}\times\boldsymbol{B}}{c}\right) , \tag{1.1}$$

where $\boldsymbol{p}$, $\boldsymbol{v}$ and $-e$ are the electron momentum, velocity and charge, respectively. c is the speed of light in vacuum. Considering the Coulomb gauge, the laser electric and magnetic fields can be written as $\boldsymbol{E} = -\partial\boldsymbol{A}/c\partial t$ and $\boldsymbol{B} = \nabla\times\boldsymbol{A}$, respectively, where $\boldsymbol{A}$ is the vector potential of the laser pulse. In the weakly relativistic limit, the single electron momentum can be considered as the sum of the rapid oscillating response $\boldsymbol{p}_q$ to the the high frequency laser filed and the slow varying nonlinear response $\delta\boldsymbol{p}$ to the podenromotive potential which is essentially the $\boldsymbol{v}\times\boldsymbol{B}$ term in Eq. (1.1), i.e., $\boldsymbol{p} = \boldsymbol{p}_q + \delta\boldsymbol{p}$. The rapid response component of the electron momentum satisfies $\partial\boldsymbol{p}_q/\partial t = -e\boldsymbol{E}$, therefore the laser vector potential is found to be $\boldsymbol{p}_q = e\boldsymbol{A}/c$. The nonlinear ponderomotive force is determined by the second order approximation in the laser field,

$$\frac{d\delta \boldsymbol{p}}{dt} = \frac{\partial \delta \boldsymbol{p}}{dt} + (\boldsymbol{v} \cdot \nabla)\, \boldsymbol{p}_q \tag{1.2a}$$

$$= -mc^2 \left(\boldsymbol{a} \times (\nabla \times \boldsymbol{a}) + (\boldsymbol{a} \cdot \nabla)\, \boldsymbol{a}\right) \tag{1.2b}$$

$$= -mc^2 \nabla \left|\boldsymbol{a}\right|^2 /2 \tag{1.2c}$$

where $\boldsymbol{a} = e\boldsymbol{A}/mc^2$ refers to the normalized laser vector potential and m is the electron mass. The weakly relativistic condition is generally defined by $|\boldsymbol{a}| << 1$. The laser ponderomotive force is determined by the time average of the right side of Eq. (1.2), which is essentially related to the laser pulse intensity, i.e., $\boldsymbol{F}_p = -mc^2 \nabla \big\langle \left|\boldsymbol{a}\right|^2 \big\rangle_t /2 \sim -\nabla I$, where $\langle\ \ \rangle_t$ denotes to the time average.

In the relativistic limit generally defined by $|\boldsymbol{a}| >> 1$ where the particles, most of the time electrons, become relativistic, the ponderomotive force has the form,

$$F_p = -\left(mc^2/\gamma\right) \nabla \left|\boldsymbol{a}\right|^2 /2\ , \tag{1.3}$$

where $\gamma = \sqrt{1 + \left|\big\langle \boldsymbol{p} \big\rangle_t\right|^2 /m^2c^2 + \big\langle \left|\boldsymbol{a}\right|^2 \big\rangle_t}$ is the time averaged relativistic factor of the electrons and the quantity $\big\langle \boldsymbol{p} \big\rangle_t$ is the momentum averaged over time. The $\big\langle \left|\boldsymbol{a}\right|^2 \big\rangle_t$ term represents the contribution of the jitter motion of the electron to the transverse momentum.

Shown in Figs. 1.1(a) and 1.1(b) are two schematic examples illustrating how the ponderomotive force affects the electron motions. The laser pulse propagates in the $+z$ direction and we only consider the transverse (x direction displayed in

figures) component of the electron motion. Fig. 1.1(a) displays an example of a plane wave propagating through the plasmas. Each of the red curves represents the electron trajectory at a different transverse initial position. Since the laser intensity is uniform transversely in this case, $F_p = 0$, therefore, we only observe electrons quiver at the very high laser frequency. However, if the laser pulse has a transverse shape, as displayed in Fig. 1.1(b), the electrons quiver as well as responding to the low frequency laser ponderomotive potential. The blue line here shows the slow varying trajectory of the electron, indicating that electrons are pushed off axis, through which the plasma wave field (the electron bubbles) is created.

1.1.3 Transition Radiation at the Plasma Vacuum Interface

Transition radiation occurs as a laser pulse or a electron bunch cross the interface separating two media with different dielectric properties. When a charged particle crosses the interface between two different materials, the fields around the charge reorganize, thus generating electromagnetic radiation. This phenomenon was predicted theoretically [41] in early 1940s and the emitted waves came to be called the transition radiation. It was mentioned also that the transition radiation at an interface between two media can be generated not only by charged particles but also by electric and magnetic dipoles, laser pulses, charged particle bunches, and other objects capable of polarizing the medium. These driving sources excite electron current in the inhomogeneous plasma, thus generating radiation.

Interest in transition has recently increased considerably based on the possibil-

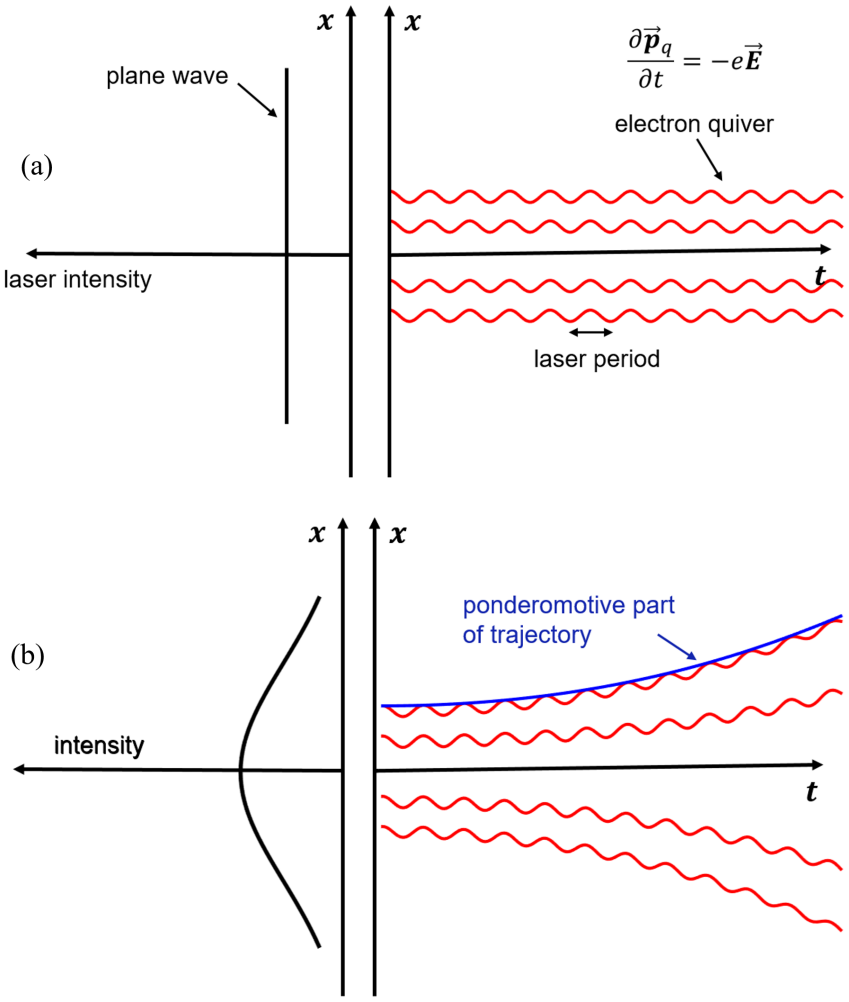

Figure 1.1: (a) Electrons only quiver at the laser frequency since the laser intensity is uniform transversely, i.e., $F_p = 0$. Each of the red curves represents the electron trajectory at a different transverse initial position. (b) For a laser pulse with a transverse Gaussian shape, the electrons quiver at the laser frequency as well as responding to the low frequency ponderomotive potential. The blue line indicates the slow varying trajectory of the electron.

ity of using this mechanism to generated terahertz radiation. A first example is the THz radiation generation by laser pulses propagating into plasmas demonstrated by Hamster et al. [12, 13]. In this case, the source of the radiation is the current driven by the ponderomotive force of a laser pulse at the vacuum plasma interface. A sec-

ond example is the transition radiation emitted by energetic electrons produced by an intense short laser pulse focused on a neutral gas jet. This radiation was detected experimentally and interpreted theoretically [20, 25–28]. The laser ionizes the gas and produces a plasma wave wake that accelerates an electron bunch. When the electron bunch crosses the plasma vacuum interface, it drives the THz transition radiation.

Transition radiation usually occurs at the plasma vacuum boundary. However, uniform plasmas commonly have varying density regions at the vacuum plasma interface. Plasma resonance may occur when laser pulses propagate through the plasma density gradient and excite electromagnetic radiation with frequency less than the maximum plasma frequency. In particular, it is found that enhanced THz radiation is generated in an increasing plasma density ramp compared with the sharp boundary case. In this thesis, we will discuss this effect in Chapter 2.

Besides generating THz waves, another application of the transition radiation produced at the plasma vacuum interface is as a diagnostic of the incident optical pulses or particle beams by indirectly detecting the properties of the emitted waves [23, 24]. Because of the fact that transition radiation is readily generated, it has been widely utilized in many laboratories.

1.1.4 Axially Modulated Plasma Waveguides

Plasmas are generated by supplying sufficient energy to a neutral gas to produce ionization. There are a number of methods to do this and these vary depending

on the application [42]. The most commonly used method of generating and sustaining a low-temperature plasma utilizes the electrical breakdown of a neutral gas in the presence of an external electric field. Other methods include injection of charged particle beams, especially electrons, or laser pulses into a neutral gas. Discharge devices such microwave discharges are also widely employed to generate plasmas. Each of these methods creates a plasma with different properties. Not all are suitable for THz generation. Uniform plasmas are not suited for ponderomotively driven THz. A laser pulse in a uniform plasma excites plasma waves which generate only electrostatic fields. Further, the waves in a uniform plasma are superluminal, making it hard to be phase matched to the laser pulse. A slow wave plasma structure is required in order to produce electromagnetic modes with subluminal phase velocities.

The realization of corrugated slow wave plasma guiding structures has been reported in [43, 44]. The method employed experimentally uses an axicon to line focus an intense laser pulse on a cluster gas jet. The hydrodynamic expansion of the hot column of plasma results in the creation of an electron density profile with density minimum on the axis for the benefit of optical guiding. Axially modulated plasma waveguides have been demonstrated by two different techniques. The first method is to modulate the optical heating on a uniform cluster jet by applying a fixed transmissive ring gating to pattern the channel formation pulse. The second method is to corrugate the neutral gas density by using an array of fine wires at the gas nozzle exit. Corrugated plasma waveguides up to several centimeters in length with modulation period as short as 35 μm can be created. Recent experimental progress [44] has been reported using a 2D spatial light modulator (SLM) to impose

the transverse phase front modulations on the heater pulse, making a programmable structure with tunable channel parameters. Deep axial modulation with periods down to tens of μm as well as centimeter scale channel length can be achieved. With properties similar to the conventional slow wave copper waveguides, such modulated plasma structures can be used for direct laser acceleration for charged particles [45–49] and quasi-phase-matched coherent electromagnetic (EM) wave generation, for example, THz generation [33, 34].

The application of corrugated plasma waveguides to direct laser acceleration of electrons can be realized considering the quasi phase matching condition when an intense short laser pulse co-propagates with a nearly relativistic electron beam in a preformed plasma channel. In uniform plasmas, direct energy gain by an electron beam interacting with a laser pulse is limited due to the fact that the laser electric field is transverse to the propagation direction, and the phase velocity is superluminal. However, a laser pulse propagating through axially corrugated plasma waveguides is composed of different spatial harmonics with subluminal phase velocities and the channel supports modes with axial electric field. With the right choice of laser pulse polarizations and plasma parameters, the phase velocity of a specific harmonic can be phase matched to the speed of an realistic electron beam, thus allowing electron acceleration directly by the guided laser field in the plasma waveguide. In a standard laser wakefield accelerator, the dephasing length, by which means the trapped electrons gain longitudinal momentum sufficient to outrun the acceleration phase of the plasma wakefield, ultimately limits the final electron energy gain. However, in an axially corrugated plasma waveguide, the guide mode

is composed of spatial modes whose associated phase velocities can be tuned by varying the density modulation period. By matching the modulation period to the dephasing length, the quasi phase matching condition can be satisfied and a relativistic electron can undergo energy gain over several dephasing length, thus an increase of the final energy gain can be achieved.

The application of corrugated plasma waveguides to generate THz radiation will be examined and discussed in detail in Chapter 3. In an axially uniform plasma, the currents driven by the ponderomotive force are steady in a frame moving at the group velocity of the laser pulse. Thus, THz radiation will not be generated. If there is radiation in one frame, there must be radiation in all frames. However, if the plasma is axially corrugated, then the currents are time dependent in all frames and the radiation is possible. Further, axially modulated channels support electromagnetic modes with subluminal phase velocities that can be phase matched to the velocity of the ponderomotive potential associated with laser pulse, and with electric field polarizations that make significant THz generation possible as well as high conversion efficiency from the optical pulse energy into THz radiation.

1.2 Models and Simulation Techniques

1.2.1 Particle In Cell (PIC) Method

The Particle In Cell (PIC) method [50, 51] is one of the most comprehensive and commonly used simulation approaches in the field of plasma physics including laser plasma interactions. It self consistently solves Maxwell's equations along with

the equation of motion for charged particles as well as the excited electrostatic and electromagnetic waves in the simulation domain. Quantities such as particle charges and current densities are accumulated on the simulation grids (Yee grids) [52] based on the spatial position and velocities of the charged particles and are updated during the interaction with the electric and magnetic fields self consistently according to their relativistic equations of motion. The particle charges and current densities further serve as the source terms in Maxwell's equations and are used to update the electric and magnetic fields during each iteration. When computing the particle charges and current densities, each simulation particle, also called macro particles, represents a number of real particles to reduce the simulation effort. Therefore, the number of charged particles used in the simulation is typically much less than the actual number in real situation.

Since Most PIC simulations of laser plasma interactions have to resolve time scales down to the laser period, a full format, three dimensional PIC simulation is always computationally expensive [53–56]. High Performance Computation (HPC), such as parallel simulation [57, 58] has been developed to accelerate the simulation process, based on the technology development of multicore CPU clusters and the Graphical Processing Units (GPUs) with thousands of threads. A number of the fully parallelized, explicit simulation codes have been developed for the demanding needs in laser plasma interactions including OSIRIS [59, 60], Vorpal [61] and TurboWAVE [62, 63].

1.2.2 TurboWAVE

Most of the PIC simulations in this thesis are conducted using the full format, multi dimensional code TurboWAVE [62, 63], which was developed by D. Gordon et. al. at the US Naval Research Laboratory. The numerical framework for TurboWAVE uses parallel processing and can work in any number of dimensions with different geometries. It provides a 3D fully self consistent PIC simulation tool with a number of field solver modules such as the explicit direct electromagnetic module and contains reduced models including ponderomotive guiding center and fluid module. Different coordinate systems such as 2D/3D cartesian, 2D azimuthally symmetric cylindrical coordinates as well as moving coordinates are allowed in TurboWAVE.

1.2.3 System Setup and Radiation Diagnostics

To simulate the laser pulse driven THz generation in inhomogeneous plasmas, we set up a region occupied by the preformed plasmas or neutral gases in a 2D cartesian simulation domain. A laser pulse is initially focused close to the interface of the plasma region and later propagates through the plasma. The pulse interacts with the inhomogeneous plasma and the ponderomotive potential drives electron currents, thus generating electromagnetic radiation. THz continues to radiate after the laser pulse leaves the region, therefore a relatively large simulation domain is required in order to collect all the THz radiation. To diagnose the properties of the generated THz, several simulation boxes enclosing the plasma region were employed and the Poynting flux across these prescribed surfaces as a function of time was

saved and later analyzed to determine the spectrum of THz radiation as well as the total radiated THz energy. Simulation results show that the amount of radiated THz energy is conserved across each of these enclosed diagnostic surfaces, which validates the setup of the simulation.

Simulation of small volumes, a plasma with 500 μm longitudinal length, can be realized on our own desktop computer workstations. In this case, a 2D planar cartesian geometry is employed in the simulation domain. However, to let the laser pulse propagate through the plasma for a realistic long distance, typically several centimeters, the simulation becomes highly time comsuming. To overcome this, a relatively large moving frame is setup on high performance computer clusters such as NERSC Edison and the Deepthought2 at UMD. The fully parallelized simulations utilizing thousands of computation threads allows us to investigate the THz generation by passing an intense short laser pulse through inhomogeneous plasmas with realistic lengths.

1.3 Structure of the Thesis

This dissertation mainly includes studies of two different mechanisms of ponderomotively driven THz generation. The first mechanism is the enhanced laser pulse driven THz generation via resonant transition radiation originating in regions of varying plasma density, which will be discussed in detail in Chapter 2. The generated THz radiation covers a broad frequency spectrum with maximum frequency close to the maximum plasma frequency. The radiation pattern is conical. It is

found that in the case of sharp plasma boundary, THz radiation is generated symmetrically at the plasma entrance and exit, and its properties are independent of the plasma density when the density exceeds a characteristic value determined by the product of the plasma frequency and the laser pulse duration. However, the results are different for a diffuse plasma boundary, the emission from the plasma entrance and exit is asymmetric. In particular, the radiation energy from an increasing density ramp is greater than for a decreasing ramp. Further, comparison of the increasing and decreasing density cases shows that the power radiated in the increasing ramp exceeds that of the sharp boundary radiation, which in turn, exceeds the power radiated in the decreasing ramp. Simulation results show enhancement by a factor of 50 can be achieved by using an increasing density gradient compared with the sharp boundary. We developed a model that attributes this effect to a resonant plasma wave process in the varying density region. Since the frequency of the generated THz is below the maximum of the plasma frequency defined as $\omega_p = \sqrt{4\pi q_e^2 n_e/m_e}$, where q_e, n_e and m_e are the electron charge, density and mass, respectively, the plasma resonance occurs at the varying density region where the dielectric function $\epsilon(z) \sim 1 - \omega_p^2(z)/\omega^2$ equals zero. In other words, the THz radiation of a specific frequency is generated via the plasma resonance at a point where $\epsilon = 0$, where its frequency matches the local plasma frequency. To escape the plasma, the THz radiation must first tunnel to the turning point where the wavenumber k equals zero before it leaves the plasma and propagates into the vacuum, where the wavenumber k is defined as $k(z) = \sqrt{\omega^2\epsilon(z) - \omega_p^2(z)}/c$. Subsequently, this picture is further utilized to develop a scaling formula for the radiated THz energy versus the

length of density ramps. The results from the model match those of the simulation for ramp lengths less than 600 μm. For longer ramps where simulations are too time consuming, the model shows that the amount of radiation reaches a maximum at a ramp length determined by collisional absorption. As an example, the simulation results show that a 1.66 J, 50 fs driver pulse can generate $\sim$400 μJ of THz radiation in a 1.2 mm increasing density ramp.

In Chapter 3, THz generation via the slow wave phase matching mechanism is explored. Excitation of the THz modes by the interaction of an ultra-short laser pulse and the fields of a miniature , axially corrugated plasma waveguide is discussed in detail. Such plasma structures have been demonstrated experimentally and they can support electromagnetic (EM) channel modes with properties that allow for radiation generation. In particular, these corrugated structures have Floquet type dispersion relations. Therefore, the EM modes have subluminal field components, thus allowing phase matching between the generated THz modes and the ponderomotive potential of the laser pulse. Both theoretical analysis and full format PIC simulations are included and compared. THz generation by this slow wave phase matching mechanism is characterized by lateral emission and a coherent, narrow band, tunable spectrum with relatively high power and conversion efficiency. Two different types of axially modulated plasma channels are considered, one has a maximum density at the lateral edges and another has the maximum density at the center of the channel. Both types of channels can be created experimentally. The channel with the maximum density at the lateral edges is more suitable for laser guiding purposes, especially for higher laser intensities (larger a_0). Therefore most

of the laser pulse energy can be guided inside the channel during the propagation and more of the pulse energy can be converted into THz radiation. The channel with the maximum density at the center is better to excite a narrow spectrum of THz modes and the enhancement of THz radiation is observed especially for the laser pulses with lower intensities (small a_0). A range of laser pulse and plasma profile parameters are considered with the goal of maximizing the conversion of optical energy to THz radiation. It is found that higher laser intensities strongly modify the THz spectrum by exciting higher order channel modes. Enhancement of a specific channel mode can be realized by using an optimum pulse duration and plasma density. The laser pulse evolution is also studied to estimate the pulse depletion length, which can be helpful in designing the length of the corrugated plasma channel. In addition, a spectral red shift of the driver pulse is observed during the propagation in the plasma channel. As long as the laser pulse is well guided in the plasma channel without side energy leaking, the wave action of the pulse is conserved during propagation and the normalized vector potential a_0 increases. Therefore, more THz radiation is generated at a later channel position and the amount of THz energy is above the linear scaling with the channel length. To be able to simulate the propagation of a laser pulse through a realistic centimeter scale plasma channel and collect all the radiated THz, we apply a relatively large moving frame in the simulation domain and a number of fully parallel simulations are implemented on CPU clusters such as NERSC Edison and Deepthought2 at UMD. As an example, a fixed driver pulse (0.55 J, $a_0 = 2$) with spot size of 15 μm and pulse duration of 15 fs excites approximately 37.8 mJ of THz radiation in a 1.5 cm corrugated plasma waveguide

with on axis average density of 1.4×10^{18} cm^{-3}, conversion efficiency exceeding 8% is achieved according to the simulation.

Chapter 4 summarizes this thesis and gives conclusions.

Chapter 2: Terahertz Generation via Resonant Transition Radiation (RTR) in A Plasma Density Gradient

2.1 Overview

Electromagnetic terahertz radiation (THz) spans frequencies from 300 GHz to 20 THz and has a wide variety of applications [1] including spectroscopy [2], remote detection [3], and medical and biological imaging [4]. Intense THz pulses can be generated at large scale accelerator facilities via synchrotron or transition radiation, but the size and cost of such facilities can be prohibitive for widespread use. Laser-solid interactions provide a small-scale alternative, but material damage limits the THz radiation to several μJ per pulse [16]. Plasmas, on the other hand, can withstand large amplitude optical pulses, motivating laser-plasma interactions as a path to high efficiency small- scale THz sources [12, 13].

There are a number of schemes in which THz radiation is generated via laser plasma interactions as introduced in Chapter 1. Here, through theory and simulation, we investigate ponderomotively driven THz radiation that occurs as a laser pulse crosses a plasma boundary [64]. We will refer to this mechanism as transition radiation in analogy with the charged particle beam counterpart. The resulting

THz radiation is characterized by conical emission and a broad spectrum with maximum frequency occurring near the maximum plasma frequency [65]. We find that the amount of THz radiation is substantially enhanced when the laser pulse passes through a gradual increasing density ramp. In particular, a 1.66 J, 50 fs driver pulse can generate 400 μJ of THz radiation in a 1.2 mm increasing density ramp, comparing quite favorably with existing THz generation schemes.

The organization of this chapter is as follows. In Sec. 2.2 , we introduce the transition radiation mechanism in the case a laser pulse normally incident on a sharp plasma boundary. A differential equation describing the radiation excitation in 2D planar geometry with an arbitrary density profile is presented. This equation can be solved for a sharp boundary, providing an integral expression for the radiated spectrum. Sec. 2.3 presents analysis and simulations of THz generation when a laser pulse is incident on a diffuse plasma boundary. An increasing density ramp results in resonant transition radiation, which enhances the radiation relative to the sharp plasma boundary. We derive a scaling law describing how the radiation depends on the plasma and laser parameters. We also show that substantially less radiation is generated in a decreasing density ramp. In Sec. 2.4 we present our conclusions and discuss future directions.

2.2 THz generation via Transition Radiation at a sharp vacuum-plasma interface

We begin by demonstrating the THz generation mechanism using the full format PIC simulation TurboWAVE [62]. The simulations, conducted in the lab frame, consist of a finite sized target plasma illuminated by a laser pulse incident from the left. Fig. 2.1(a) displays an example for the case of a sharp boundary, uniform plasma. A range of laser pulse and plasma parameters is considered. To quantify the radiation emitted from the plasma, we calculate the Poynting flux through prescribed surfaces outside the plasma region. This captures the radiation emitted in the forward, backward and lateral directions.

As an example, we consider a uniform plasma with sharp step boundaries as illustrated in Fig. 2.1(a). A laser pulse of duration (FWHM) $\tau_p = 50$ fs traverses the plasma from left to right. The plasma is 500 μm long and 90 μm wide with a density of $n = 2.8 \times 10^{18}\ cm^{-3}$. The transverse plasma dimension is chosen mainly for the convenience of simulation. Fig. 2.1(b) shows a false color image of the longitudinal component of the Poynting flux after the laser pulse traverses the entire plasma from left to right. Plasma wave excitation can be observed as the rapid longitudinal oscillations in the Poynting flux. The alternate positive and negative values of Poynting flux indicate a small average flux. However, at both ends outside the plasma, we observe transition radiation as the red and blue streaks denoting forward and backward Poynting flux, respectively.

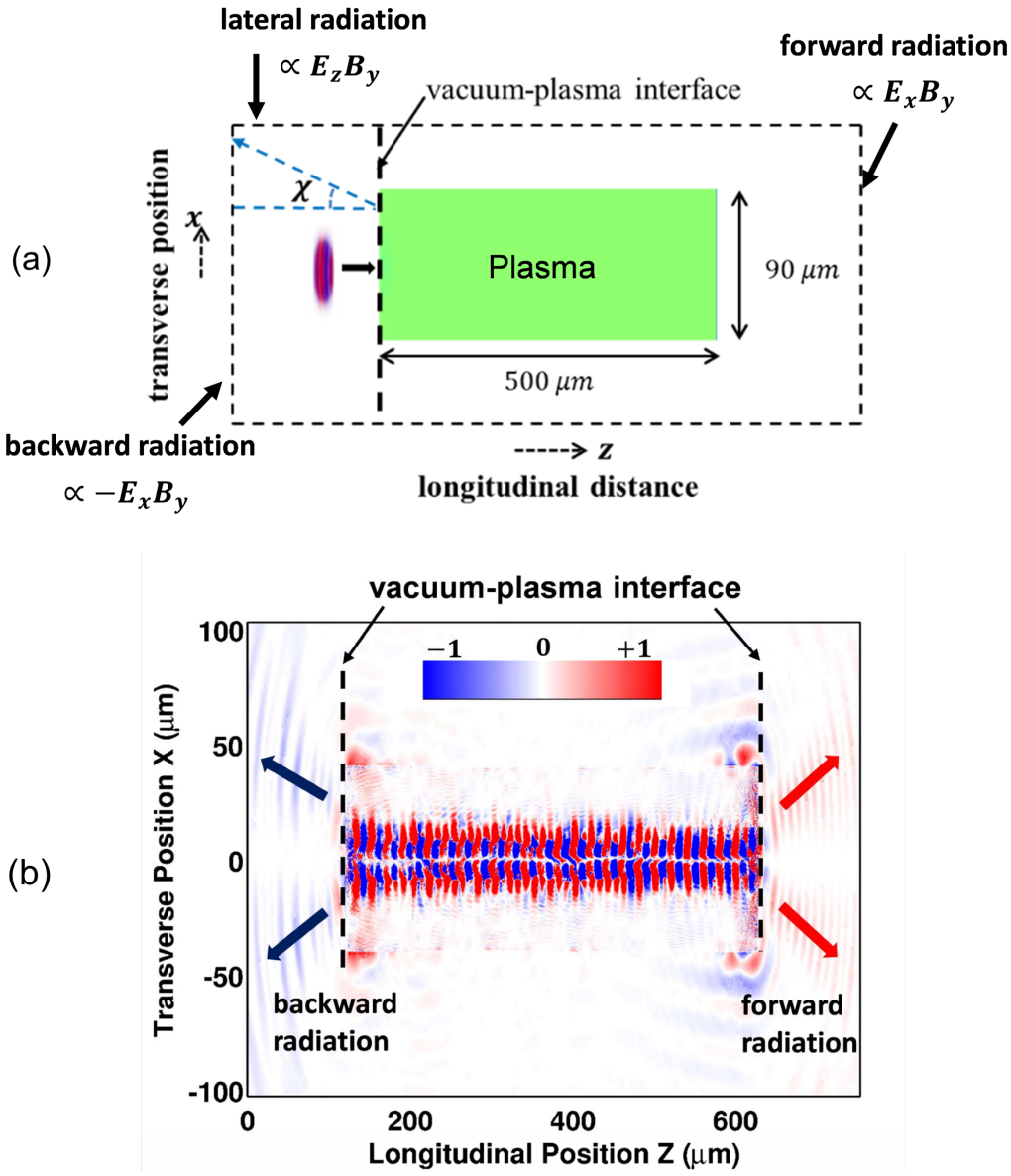

Figure 2.1: (a) Diagram of simulation set up for transition radiation at the vacuum plasma boundary. The diagnostic box is set outside the plasma channel. The Poynting flux through each surface is calculated. (b) A snap shot of the Poynting flux $E_x B_y$ in PIC simulations using TurboWAVE. The transition radiation is generated at both boundaries when the laser travels through the plasma from left to right.

The laser pulse produces a low frequency ponderomotive force, which is proportional to the gradient of the laser pulse intensity, $F_P \sim -\nabla I$. This force drives

the ponderomotive currents that produce the THz radiation. We note that a key element that is required for coherent ponderomotively driven THz generation is that the plasma currents be dynamic in all inertial reference frames. This occurs in Refs. [33] and [34] by virtue of the fact that the driving laser pulse propagates in a spatially periodic plasma channel. It occurs in Refs. [64], [65] and the present work due to the fact that the ponderomotively driven transition radiation is generated at the boundary of the plasma. Thus, transition radiation is a possible explanation for the results of the Refs. [12] and [13]. However, THz radiation will not be generated by the currents in the steady wake following a laser pulse in a uniform plasma as suggested by the analysis of Refs. [12] and [13]. In such a case, all currents are steady in a frame moving with the group velocity of the laser pulse, and consequently no radiation occurs.

Following Ref. [64], we can derive an expression for the radiated energy per unit frequency (ω) and per unit angle in 2D planar geometry. We start from Maxwells equations and the following cold plasma fluid equation,

$$m_e \frac{\partial \boldsymbol{J}}{\partial t} = q_e^2 n_e \boldsymbol{E} - q_e n_e \boldsymbol{\nabla} V_p \ , \tag{2.1}$$

where m_e, q_e are the electron mass and charge, respectively. The quantity n_e is the electron density, and V_p is the averaged ponderomotive potential associated with the incident pulse.

As the pulse propagates through the vacuum plasma interface, the electric

field of the low frequency radiation can be obtained from the following expression,

$$\frac{\partial^2 \boldsymbol{E}}{\partial t^2} + \omega_p^2 \boldsymbol{E} + c^2 \nabla \times (\nabla \times \boldsymbol{E}) = \frac{\omega_p^2}{q_e} \boldsymbol{\nabla} V_p \,, \tag{2.2}$$

where $\omega_p = \left(4\pi q^2 n_e / m_e\right)^{1/2} = 5.64 \times 10^4 \times \sqrt{n_e \; [cm^{-3}]}$ is the plasma frequency and c is the speed of light in vacuum. An axisymmetric laser pulse with ponderomotive potential V_p is described by Eq. (2.3). We take the laser pulse intensity and hence ponderomotive potential to be described by a spatio-temporal Gaussian profile,

$$V_p = V_{p0} \exp\left(-\frac{-x^2}{R_L^2} - \frac{\xi^2}{L_p^2}\right) , \tag{2.3}$$

where $V_{p0} = m_e c^2 a_0^2/4$ is the maximum of the laser ponderomotive potential in terms of the normalized laser vector potential $a_0 = eE_0/(m_e c\omega_0)$ with the laser central frequency ω_0 and field amplitude E_0. The quantities $\sqrt{ln2}R_L$ and $2\sqrt{ln2}L_p$ are the FWHM laser spot size and pulse duration respectively. The quantity $L_p = c\tau_p$ is the length and $\xi = z - ct$ is the shifted longitudinal coordinate.

To solve Eq. (2.2) in 2D planar geometry, one can apply Fourier transform to Eq. (2.2) with respect to both time t and transverse coordinate x according to the

following definition,

$$\bar{E}(k_x, z, \omega) = \int_{-\infty}^{\infty} dt dx \boldsymbol{E}(x, z, t) \exp\left(i\omega t - ik_x x\right) , \tag{2.4a}$$

$$\boldsymbol{E}(x, z, t) = \frac{1}{(2\pi)^2} \int_{-\infty}^{\infty} d\omega dk_x \bar{E}(k_x, z, \omega) \exp\left(-i\omega t + ik_x x\right) . \tag{2.4b}$$

By simple calculations, one can obtain a differential equation as described by Eq. (2.2) for the Fourier transformed transverse component of the electric field $\bar{E}_x(k_x, z, \omega)$, which is driven by the ponderomotive potential of the laser pulse,

$$\frac{d}{dz}\left(\frac{\epsilon(z)}{k^2(z)}\frac{d}{dz}\bar{E}_x\right) + \epsilon(z)\bar{E}_x \equiv S(z) = -i\frac{d}{dz}\left(\frac{k_x}{k^2(z)}\frac{\omega_p^2(z)}{\omega^2}\frac{d}{dz}\frac{\bar{V}_p}{q_e}\right) - ik_x\frac{\omega_p^2(z)}{\omega^2}\frac{\bar{V}_p}{q_e} , \tag{2.5}$$

where $\epsilon = 1 - \omega_p^2(z)/\omega(\omega + i\nu)$ is the frequency dependent dielectric function of the plasma and ν is the collision frequency, which in our case is much less than the radiation frequency ω. In obtaining Eq. (2.5) we have assumed the electron density depends only on the longitudinal direction z. That is, the plasma has infinite transverse extent. The longitudinal wavenumber is defined as $k^2 = \omega^2\epsilon/c^2 - k_x^2$ and $k_z = \omega/c$. The quantity $\bar{V}_p = \hat{V}_p(\omega, k_x)\exp\left(ik_z z\right)$ is the Fourier transformed amplitude of the laser pulse V_p with $\hat{V}_p$ given by the following expression,

$$\hat{V}_p = V_{p0}\pi R_L \tau_p \exp\left(-\frac{\omega^2\tau_p^2}{4} - \frac{k_x^2 R_L^2}{4}\right) . \tag{2.6}$$

The radiated energy per unit length U' can be obtained in the form of a spectral density in (ω, k_x),

$$\frac{dU'}{d\omega} = \int_{-\infty}^{\infty} dk_x S_z(\omega, k_x) \ , \tag{2.7a}$$

$$U' = \int_0^{\infty} d\omega \frac{dU'}{d\omega} \ . \tag{2.7b}$$

The spectral density Sz is given by

$$S_z(\omega, k_x) = \frac{c}{8\pi^2} \frac{1}{2\pi} \big(E_x(\omega, k_x) B_y^*(\omega, k_x) + c.c. \big) \ , \tag{2.8}$$

where B_y is the transverse component of the magnetic field, which in turn is given by [64],

$$B_y = i \frac{\omega}{c} \frac{1}{k^2(z)} \left(k_z k_x \frac{\omega_p^2(z)}{\omega^2} \frac{V_p}{q_e} - \epsilon(z) \frac{dE_x}{dz} \right) \ . \tag{2.9}$$

In 2D planar geometry the nonzero field components are (E_x, B_y, E_z) and in 2D cylindrical geometry the field components are (E_r, B_θ, E_z). Thus, in an experiment one expects the radiated THz will be polarized with electric field E in the $r - z$ plane.

We now consider a sharp vacuum plasma interface in 2D planar geometry such that the plasma density $n_e = 0$ for $z < 0$ (vacuum) and $n_e = n_0$ for $z \geq 0$ with an infinite transverse size. We solve Eq. (2.5) in the two uniform regions described above separately and note that the transverse component of electric and magnetic

field are continuous at the boundary. We then inverse Fourier transform the field back to the space domain and obtain the following expression for the radiated electric field in vacuum ($z < 0$),

$$\bar{E}(x,z,\omega) = -i\sqrt{2\pi}\frac{\omega_p^2 R_L \tau_p}{8}\frac{m_e}{q_e}a_0^2\frac{\sin\chi\cos^2\chi}{\sqrt{i\omega r/c}}\cdot\frac{\exp\left(i\frac{\omega}{c}r - \frac{\omega^2\tau_p^2}{4} - \frac{\omega^2 R_L^2\sin^2\chi}{4c^2}\right)}{\epsilon\cos\chi + \sqrt{\epsilon - \sin^2\chi}}\ , \tag{2.10}$$

where χ is the observation angle in Fig. 2.1(a), $r = \sqrt{x^2+z^2}$ is the distance in 2D planar geometry and the dielectric function is given by $\epsilon = 1 - \omega_{p0}^2/\omega^2$ since $\nu << \omega$. The resulting radiated energy per unit frequency (ω) and length radiated backward in 2D planar geometry can be obtained using Eq. (2.7a) and is expressed as,

$$\frac{dU'}{d\omega} = \frac{L_p^2 R_L^2}{|\omega|}\frac{\omega_{p0}^2}{32\pi}\frac{m_e^2}{q_e^2}a_0^4\int_0^1 d\alpha\frac{\alpha^2\sqrt{1-\alpha^2}\times\exp\left[-\frac{\omega^2}{2c^2}\left(L_p^2 + R_L^2(1-\alpha^2)\right)\right]}{\left|\epsilon(\omega)\alpha + \sqrt{\alpha^2 - \omega_{p0}^2/\omega^2}\right|^2}\ . \tag{2.11}$$

The integration over α can be viewed as an integration over all possible transverse wavenumbers k_x since $\alpha = \cos\chi = \sqrt{1 - k_x^2c^2/\omega^2}$, where χ is the observation angle as shown in Fig. 2.1(a). Thus the integrand in Eq. (2.11) approximates the angular distribution of the radiation. We note that the integrand vanishes for both $\alpha = 0$ and $\alpha = 1$. Therefore the emerging radiation will have a conical distribution. The angular distribution of the radiated energy can be obtained by,

$$\frac{dU'}{d\chi} = \cos\chi\int_{-\infty}^{\infty} d\omega\frac{\omega}{c}S_z(\omega,k_x)\ . \tag{2.12}$$

In the simulation setup as shown in Fig. 2.1(a), a formula describing the radiated energy flux across the transverse boundary x can be derived to investigate the radiated energy angle by simply applying Eq. (2.10) to Eq. (2.13),

$$\frac{dU'}{dx} = \frac{\omega_{p0}^4 L_p^2 R_L^2}{64\pi} \frac{m_e^2}{q_e^2} a_0^4 \left(\frac{\sin^3\chi \cos^3\chi}{|x|} \right) \int_0^\infty \frac{d\beta}{\beta} \frac{\exp\left[-\frac{\beta^2 \omega_{p0}^2}{2c^2} \left(L^2 + R_L^2 \sin^2\chi \right) \right]}{\left| (1-\beta^{-2})\cos\chi + \sqrt{\cos^2\chi - \beta^{-2}} \right|}, \tag{2.13}$$

where $\beta = \omega/\omega_{p0}$ represents the normalized radiation frequency.

In Fig. 2.2(a) backward radiation spectra predicted by the simulation are compared with Eq. (2.11). For this comparison, the laser pulse energy is 66 mJ ($a_0 = 0.4$) with a 800 nm wavelength, 15 μm spot size and 50 fs pulse duration. Below the maximum plasma frequency, a broad spectrum of radiation is observed. Results are shown for two different length plasma slabs demonstrating that, as expected, the radiation is insensitive to the plasma length. This is consistent with the radiation originating from the left boundary. Comparing the theory and simulation one notices a large deviation around $\omega/\omega_p = 0.4$ in the simulation results labeled $L = 500$ μm and $L = 100$ μm, which is not observed in the 2D theory. This deviation is dependent on the transverse size of the target plasma. In particular, if we increase the transverse size from 90 μm to 180 μm, we obtain the curve labelled $W = 180$ μm in Fig. 2.2(a) in which the deviation is partially suppressed. We speculate that the deviation is due to the interference between ray paths involving reflection from

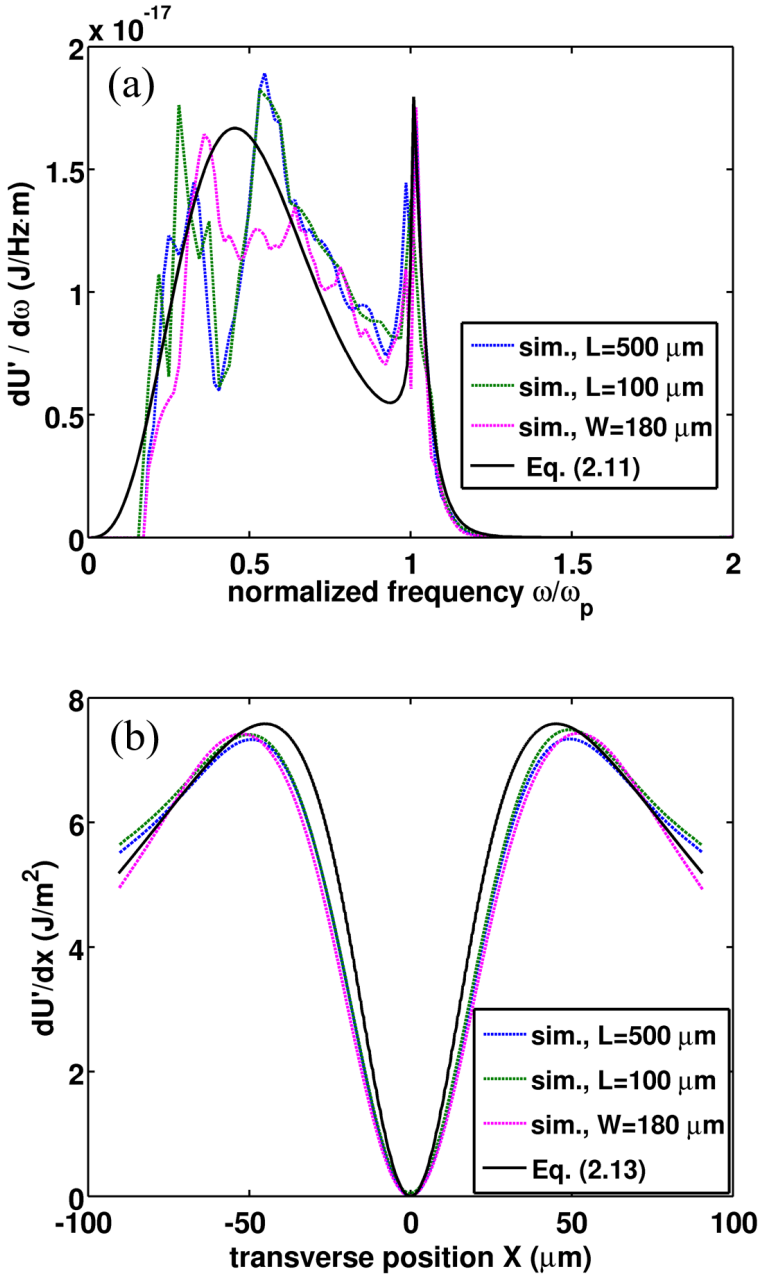

Figure 2.2: (a) Comparison of radiated spectral density. Shown are theoretical values (Eq. (2.11), black solid), and simulations using TuroWAVE for plasma length $L = 500$ μm (blue dashed) and $L = 100$ μm (green dashed). (b) Comparison of emerging radiation angle. Shown are theoretical values (Eq. (2.13), black solid), and simulations for plasma length $L = 500$ μm (blue dashed) and $L = 100$ μm (green dashed). Simulation results for plasma with a larger transverse size $W = 180$ μm (magenta dashed) are also provided in both figures.

the side boundary. One may also notice a low frequency cut-off ($\omega/\omega_p = 0.15$) for the simulation which is due to the finite size of the simulation domain. The simulation using the same parameters as in Fig. 2.2(b) shows that the radiation peeks at an angle $\chi = 25°$, indicating that the THz emission is conical. In particular, the conical radiation angle is determined by the spot size of the laser pulse as well as the plasma density.

Figure 2.3 displays the dependence of the total energy per unit length U' on plasma density. The radiated energy is nearly constant for densities above $1.5 \times 10^{18}\ cm^{-3}$. In the inset Fig. 2.3(b), the spectra of radiated energy for different densities is displayed, along with the frequency spectrum of the ponderomotive potential. The spectra of the ponderomotive potential limits the radiated energy spectrum, explaining the saturation of the radiated energy with density. For densities above the characteristic density determined by the laser pulse duration, the laser pulse excites a current at the boundary that depends primarily on the properties of the laser pulse. For example in Fig. 2.3 , the peak radiated energy occurs at an electron density of $1.5 \times 10^{18}\ cm^{-3}$, and we have $\omega_{p0}\tau_p \sim \pi$.

We have also conducted simulations to examine the scaling of radiated energy with laser intensity. According to Eq. (2.11), the radiated energy should scale as a_0^4 when $a_0 << 1$. The simulations verified this scaling. However, as a_0 increases into the relativistic regime, the radiation saturates possibly due to the increase in effective electron mass resulting from the quiver velocity. As an example, the radiated energy is about 140 μJ with $a_0 = 4$ and 48 nJ with $a_0 = 0.4$.

We use the pre-formed plasma in the simulations. However, for practical

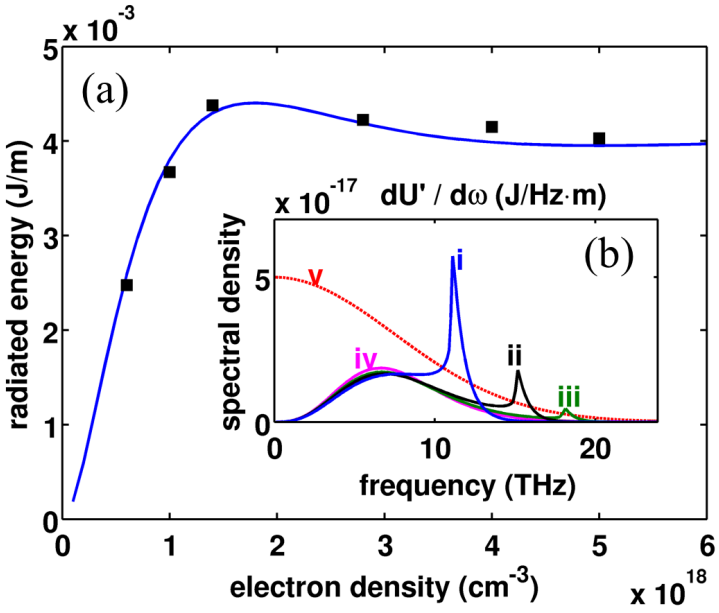

Figure 2.3: (a) Radiated energy versus electron density (2D theory: line; TurboWAVE: squares.). Energy is insensitive to plasma density above $1.5 \times 10^{18}\ cm^{-3}$. (b) Radiation spectra for different plasma densities: (i) $1.5 \times 10^{18}\ cm^{-3}$, (ii) $2.8 \times 10^{18}\ cm^{-3}$, (iii) $4 \times 10^{18}\ cm^{-3}$, (iv) $6 \times 10^{18}\ cm^{-3}$. The red dotted line (v) is the spectrum of the laser envelope $\bar{V}_p$ with arbitrary units.

setup in the experiment, one can simply shine one single laser pulse into the gas, for example, hydrogen. Since the laser intensity is so high ($> 10^{17}\ W/cm^2$), the front of the pulse will fully ionize the gas and form the electron plasmas while the peak of the pulse will drive the transition radiation. Shown in Figs. 2.5(a) and 2.5(b) are the radiated THz energy across the left and lateral diagnostic boundary as shown in Fig. 2.1(a), respectively. Simulation results indicate that the radiated THz energy and spatial distribution are almost identical. Therefore, a pre-formed plasma is not necessary, which simplifies the experiment setup.

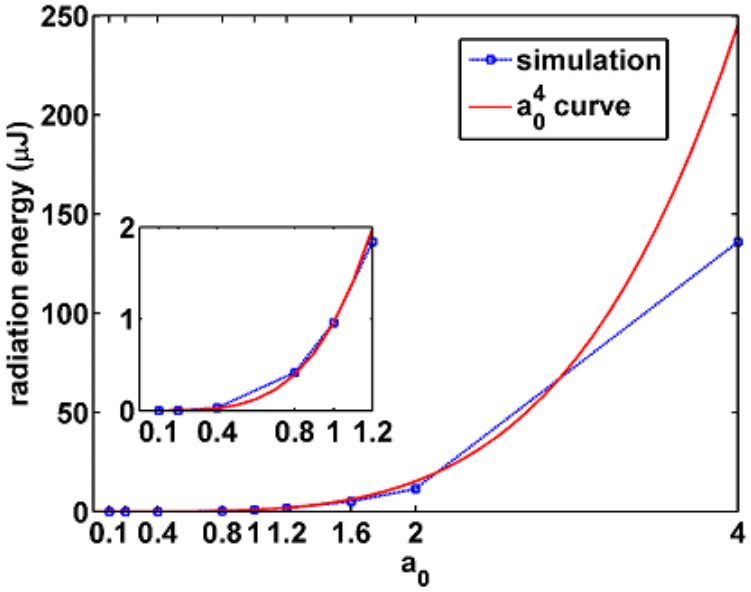

Figure 2.4: Scaling of radiated THz energy with laser intensities. The spot size and pulse duration remain the same as 15 μm and 50 fs, respectively. Theory predicts scaling to be $a_0^4/(1+a_0^2)$ based on ponderomotive effect. Simulation results (blue) from TurboWAVE agree with the a_0^4 scaling (red) in the weakly relativistic regime where $a_0 << 1$. The scaling is weaker where $a_0 >> 1$.

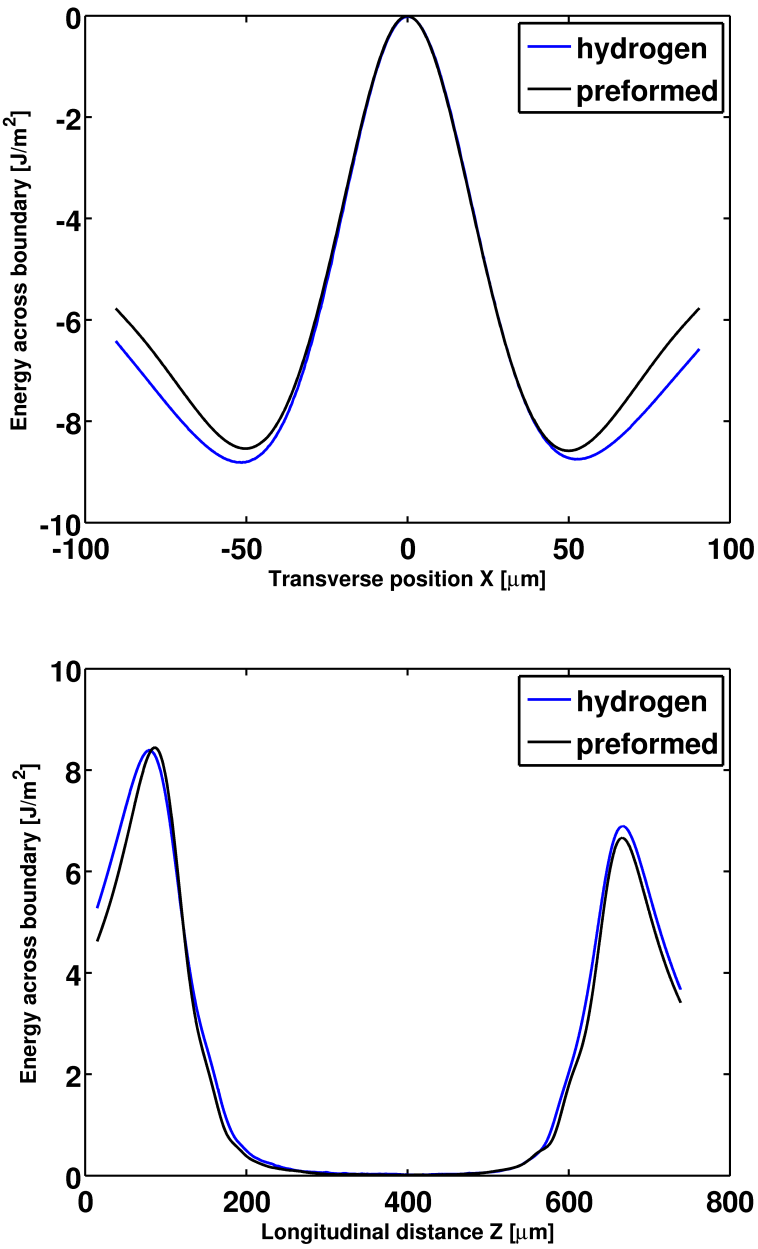

Figure 2.5: Radiated THz energy across the (a) left and (b) lateral diagnostic boundary as shown in Fig. 2.1(a), respectively.

2.3 THz generation via Resonant Transition Radiation in diffuse plasma profiles

The results in Sec. 2.2 are for the case of a sharp plasma-vacuum. When the density transition has a ramp the results change in two ways. First there is an asymmetry between radiation generated when the laser enters and leaves the plasma. Second, the amount of radiation generated as a pulse enters the plasma increases as the length of the transition region increases. The asymmetry is shown in Fig. 2.6, where false color images of the spectrum of the Poynting flux through the lateral simulation boundary are displayed. For a sharp boundary 2.6(a), as discussed in Sec. 2.2, the radiation generated by the laser pulse entering and leaving the plasma is the same as evidenced by the equal size patches in 2.6(b). However, when the ramp is added 2.6(c), the amount of energy radiated when the laser enters the plasma goes up while the amount radiated upon leaving goes down as displayed in 2.6(d).

In Fig. 2.7 we plot the total energy per unit length radiated from the increasing density transition for several ramp lengths. Also shown in this figure are the results obtained by solving Eq. (2.5) and evaluating Eq. (2.7a). The solid line in Fig. 2.7 is a scaling formula that will be derived subsequently.

We develop a model to describe THz generation in a density ramp via the process of resonant transition radiation. According to our theory, the radiation at a given frequency is generated at the point in the plasma where its frequency matches

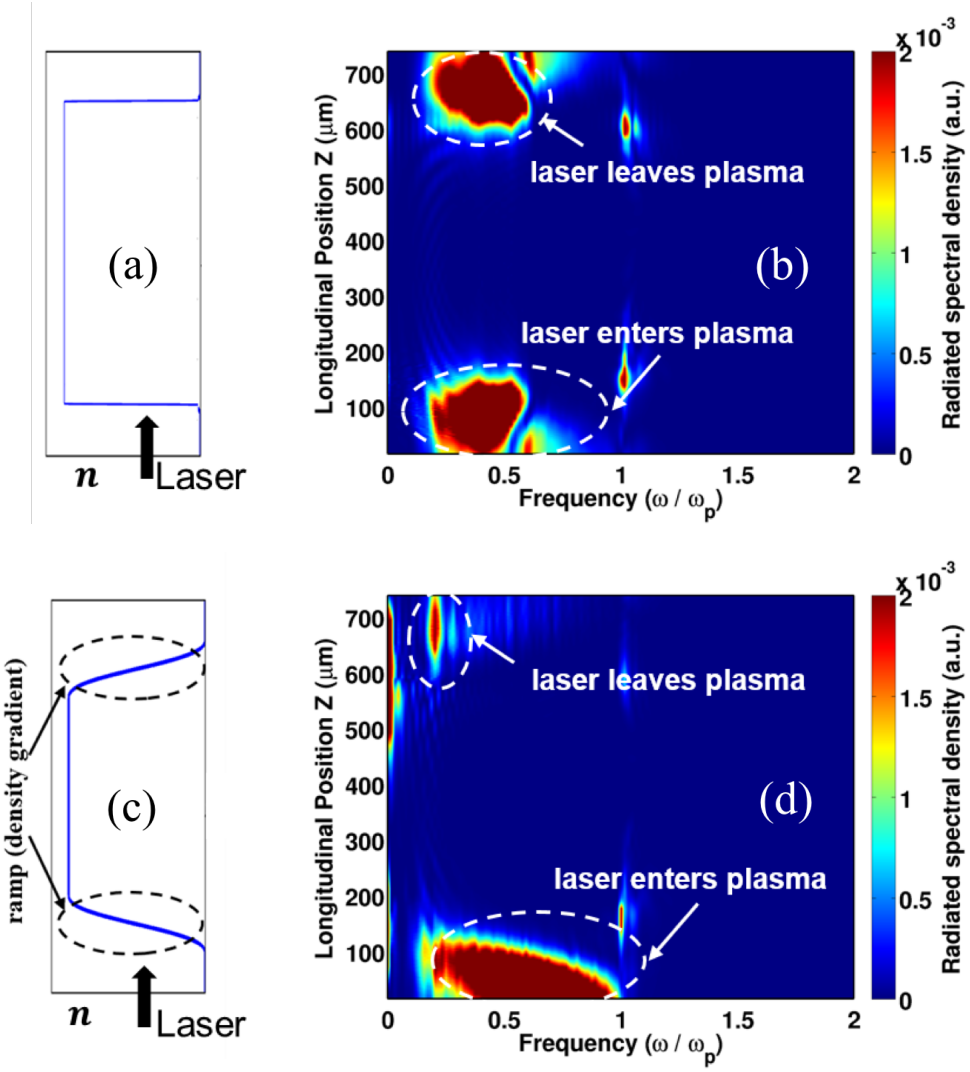

Figure 2.6: Comparisons of (a) plasma density with sharp step boundaries and (c) plasma density with increasing and decreasing ramps (∼25 μm). Simulation results, radiation spectrum as a function of the longitudinal distance and frequency showing that (b) the step boundary is symmetric while (d) the case with density ramps shows asymmetry.

the local plasma frequency and with a range of transverse wavenumbers. The radiation must then tunnel out of the plasma to the point where it can propagate. The process has many similarities to the resonant absorption in a diffuse plasma profile. A schematic plot is shown in Fig. 2.8 to illustrate this process. As the laser pulse

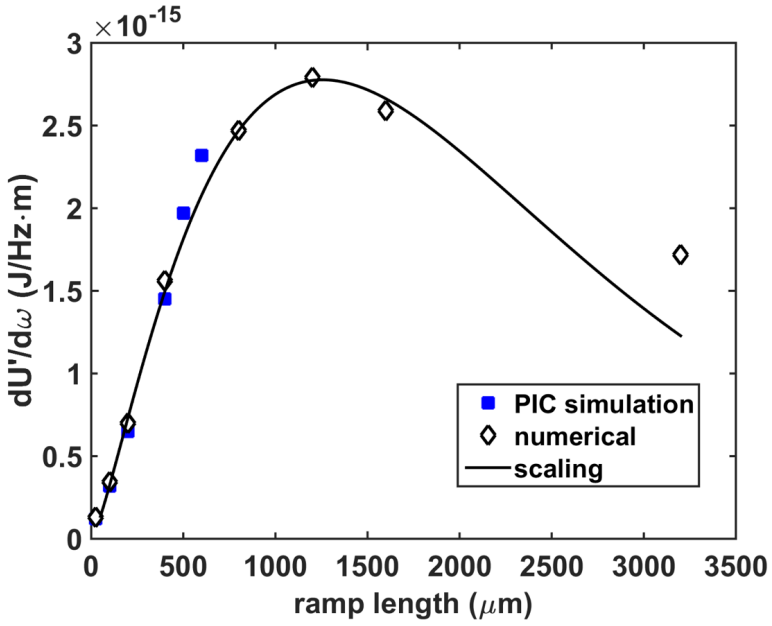

Figure 2.7: Comparisons of radiated spectral density using different increasing ramp lengths at a particular radiation frequency $\omega_1 = 0.6\omega_{p0}$. Shown are simulation results (square), numerical results of our model (diamond) and the scaling theory Eq. (11). Note from Fig. 2.2(a) the corresponding value in the sharp boundary case is $dU'/d\omega = 1.5 \times 10^{-17}$ (J/Hz·m).

propagates through the increasing density gradient, the THz generated during the transition process is below the plasma frequency, thus the plasma resonance exists in the ramp. Radiation of frequency ω is generated at the plasma resonance at z_1 (where the dielectric function ϵ is zero), but needs to transit to the turning point z_2 (where the wavenumber k equals zero) to escape the plasma.

Note that the solution to Eq. (2.5) is a combination of a homogeneous solution (by simply setting the driver $S(z) = 0$) and a particular solution associate with the driver which describes the excitation of potential plasma wave fields. This particular solution in a uniform plasma can be analytically expressed as,

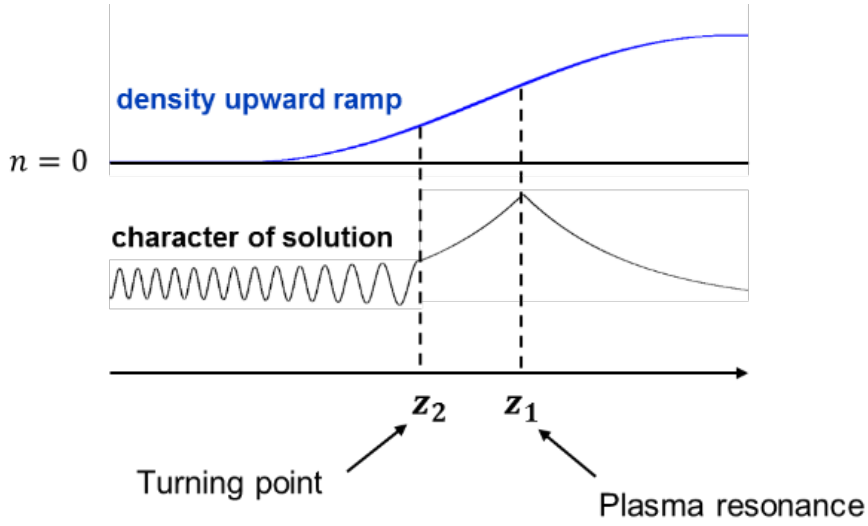

Figure 2.8: Schematic plot for THz generation via resonant transition radiation in the density ramp region. Shown are plasma density profile (blue) and the characteristic solution of the electric field E_r (black). Plasma resonance in the ramp is expected.

$$E_p = -\frac{ik_x}{\epsilon}\frac{\omega_p^2}{\omega^2}\frac{\hat{V}_p}{q_e}\exp\left(ik_z z\right) . \tag{2.14}$$

The particular solution is valid when the density scale length is much longer than the THz wavelength, which is the case considered here. We note the particular solution breaks down at the plasma resonance, $\epsilon(z_1) = 0$, where a more complete solution must be found.

It must be pointed out that this particular solution generates no radiation, which can be verified by substituting Eq. (2.14) into Eq. (2.8). Therefore, the radiated energy is given by,

$$U' = \int_0^\infty d\omega \int_{-\infty}^{\infty} dk_x S_h(z) \ , \tag{2.15}$$

where the spectral density is given in terms of the homogeneous solution,

$$S_h(z) = \frac{c}{16\pi^3}\frac{1}{i}\frac{\omega}{c}\frac{\epsilon}{k^2}\left(E_h^*\frac{dE_h}{dz} - E_h\frac{dE_h^*}{dz}\right) \ , \tag{2.16}$$

where E_h is the solution from Eq. (2.5) by setting $S(z) = 0$. Equation (2.5) also breaks down at the plasma resonance where the local particular and homogeneous solutions couple determining the amplitude of the homogeneous solution.

One can show that $S_h(z)$ is a constant (independent of z) for $z < z_1$, which is further verified by the numerical solutions shown in Fig. 2.10(a). To determine the level of homogeneous solution we expand around the plasma resonance where $\epsilon(z_1) \approx 0$. We take $z_1 = 0$ and the dielectric function can be approximated as $\epsilon \approx -z/L_0 + i\nu/\omega$, where L_0 is the characteristic length defined as,

$$\frac{1}{L_0} = -\frac{dRe\{\omega\}}{dz}\bigg|_{Re\{\epsilon\}=0} \ . \tag{2.17}$$

Near the resonance, the homogeneous version of Eq. (2.5) becomes

$$\frac{d}{dz}\left(z\frac{d}{dz}E_h\right) = 0 \ . \tag{2.18}$$

And the solution of E where $z \to 0^-(z_1^-)$ satisfies the following,

$$E_h = c_< \left(\ln \frac{z}{L_0} + \alpha_< \right) \ . \tag{2.19}$$

An expression of S_h can be obtained by using the above approximation in (2.16),

$$S_h = \frac{1}{16\pi^3} \frac{\omega}{ik_x^2 L_0} \left| c_< \right|^2 \left(\alpha_<^* - \alpha_< \right) \ . \tag{2.20}$$

where $c_<$ and $\alpha_<$ are constants, which are determined by examining the solution of Eq. (2.5) near the plasma resonance including the source. A similar expression for the homogeneous solution for $z > 0$ applies but with different constants, $c_>$ and $\alpha_>$. We now derive an expression for the total solution near the resonance as shown following,

$$\bar{E}_x = \int_z \frac{\Psi dz'}{z' - iZ_\nu} \exp\left(\pm ik_z z' \right) + c \left[\ln \left(\frac{z}{L_0} - i\frac{\nu}{\omega} \right) + \alpha \right] \ , \tag{2.21}$$

where $\Psi = k_z k_z L_0 \hat{V}_p / q_e$, $Z = L_0 \nu / \omega$, c, α are constants to be matched to the homogeneous solution and the integration contour is to be determined. The $\pm$ sign demotes the direction of the laser pulse. In Eq. (2.21), the first term becomes the particular solution associated with the laser pulse far from the resonance and the second term is in the form of the homogeneous solution as described by Eq. (2.19), which presumably will carry the radiation.

Expression (2.20) shows that the Poynting flux is given by the imaginary part of the coefficients $\alpha_>$ and $\alpha_<$. For $z > 0$, the homogeneous solution is evanescent and consequently $\alpha_>$ is real. The integral expression (2.21) relates the coefficients $\alpha_>$ and $\alpha_<$.

We now determine the connection between $\alpha_>$ and $\alpha_<$. If the laser is traveling in the positive-z direction ($+ik_z z$), the upper limit of the limit should be taken to be $z' = i\infty$ to give convergence to the integral. The integration contour is the then of the type shown in the top row of Fig. 2.9. Then for $z > 0$ the path is C as illustrated on the top left of Fig. 2.9. Evaluation of Eq. (2.21) using contour C , one can fix c and α in (2.21) to be $c_>$ and $\alpha_>$.

$$\bar{E}_x = \int_z^{i\infty} \frac{\Psi dz'}{z' - iZ_\nu} \exp\left(ik_z z'\right) + c_> \left[\ln\left(\frac{z}{L_0} - i\frac{\nu}{\omega}\right) + \alpha_>\right] . \tag{2.22}$$

For $z < 0$, the contour is deformed to the one labeled C' and a residue at the pole $z' = iZ_\nu$ is accumulated.

$$\bar{E}_x = \int_z^{i\infty} \frac{\Psi dz'}{z' - iZ_\nu} \exp\left(ik_z z'\right) + \left(2\pi\Psi \exp\left(-k_z Z_\nu\right) + c_> \left[\ln\left(\frac{z}{L_0} - i\frac{\nu}{\omega}\right) + \alpha_>\right]\right) . \tag{2.23}$$

Matching Eq. (2.19) for $z > 0$ and $z < 0$ to Eqs. (2.22) and (2.23) gives

$$c_< \left[\ln\left(\frac{z}{L_0} - i\frac{\nu}{\omega}\right) + \alpha_<\right] = 2\pi\Psi \exp\left(-k_z Z_\nu\right) + c_> \left[\ln\left(\frac{z}{L_0} - i\frac{\nu}{\omega}\right) + \alpha_>\right] . \tag{2.24}$$

Matching the logarithmic and constant parts, the following conditions are obtained,

$$c_< = c_> = \frac{2\pi\Psi \exp\left(-k_z Z_\nu\right)}{\alpha_< - \alpha_>} \ . \tag{2.25}$$

By substituting Eq. (2.19) into Eq. (2.20), finally we obtain an expression for the total radiated energy per unit frequency ω and per unit wavenumber k_x when the laser pulse is incident on an increasing density ramp,

$$S_h = \frac{1}{4\pi} \frac{\omega}{ik_x^2 L_0} \frac{\alpha_<^* - \alpha_<}{\left|\alpha_< - \alpha_>\right|^2} \left|\Psi \exp\left(-k_z Z_\nu\right)\right|^2 \ . \tag{2.26}$$

where $\alpha_<$ and $\alpha_>$ are constants that must be determined by numerical solution of the homogeneous equation.

If the pulse travels from right to left ($k_z < 0$), it propagates through a decreasing density ramp. As a result of $k_z < 0$, the integral in Eq. (2.21) must be carried out on a contour that terminates in the lower half plane as illustrated in Fig. 2.9. The solutions for $z > 0$ and $z < 0$ in this case have no jump since there is no pole (singularity) on the negative image axis (Fig. 2.9). One finds from Eq. (2.24) without the residue contribution $c_> = c_<$ and $\alpha_> = \alpha_<$. Thus $S_h = 0$, meaning that no radiation is generated through the decreasing density ramp. This verifies our simulation results with TurboWAVE [62] in Fig. 2.6(d), where one can see the amount of THz generation through an increasing ramp is far more than that through

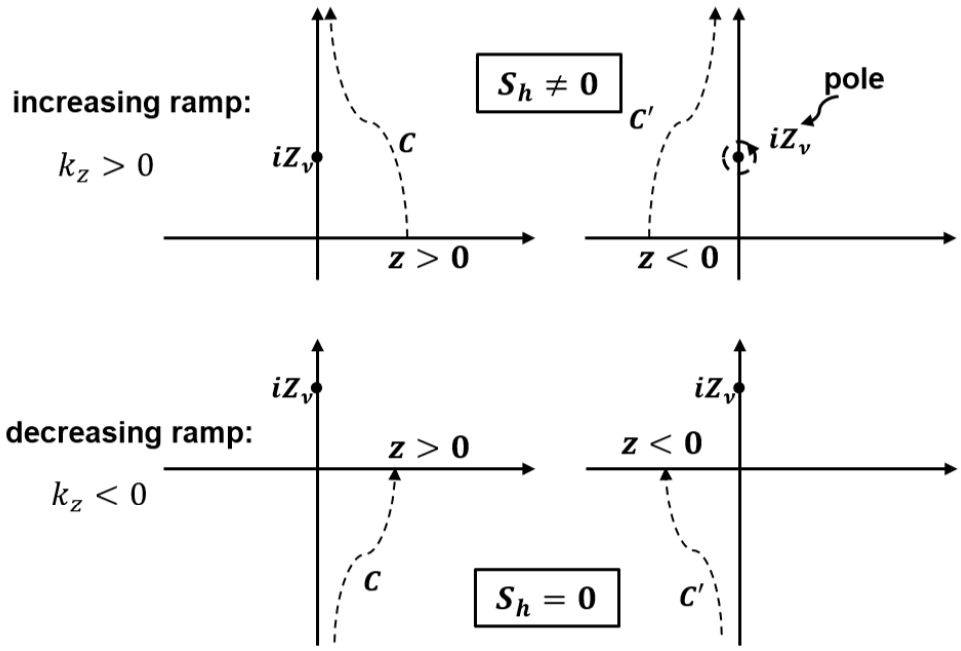

Figure 2.9: Contours for evaluation of the integral in Eq. (2.21) for an increasing (a) and decreasing (b) density ramp.

the decreasing ramp. The physics of this asymmetry between the increasing and decreasing ramps can be explained by a form of phase matching [35, 66]. The phase of the integrand in Eq. (2.21) is given by $\phi + k_z z'$ where $\phi = \tan^{-1}(Z_\nu/z')$ decreases as z' increases. Therefore, if $k_z > 0$, the phase matching condition can be satisfied at a point z' where $k_z + d\phi/dz' = 0$. However, the phase matching condition cannot be satisfied if $k_z < 0$.

To investigate the effect of a density ramp we turn to numerical solutions of Eq. (2.5) for the THz electric field in the case of diffuse density profiles. The details of a numerical method to solve Eq. (2.5) is included in Appendix A. Shown in Fig. 2.10 are the simulation results of the electric field $\bar{E}_x(\omega, k_x)$ at a particular radiation frequency $\omega = 0.8\omega_{p0}$ and wavenumber $k_x = 0.4\omega/c$ where ω_{p0} is the maximum plasma frequency and c is the speed of light in vacuum. The laser properties and electron density remains the same as in Sec. 2.2. Figs. 2.10(a) and 2.10(b) show that the laser pulse propagates through an increasing density ramp ($k_z > 0$) and a decreasing ramp, respectively. This is realized in the solution of Eq. (2.5) not by reflecting the density profile, but rather, by changing the direction of the laser propagation. This in turn is done by making the substitution $\bar{V}_p = \hat{V}_p \exp(ik_z z)$ to $\bar{V}_p = \hat{V}_p \exp(-ik_z z)$ in Eq. (2.5). In both cases, Figs. 2.10(a) and 2.10(b), the field in the uniform density region ($z > 200$ μm) responds to the laser pulse in the form of a wake with a spatial dependence in the form of a wave, $\exp(\pm ik_z z)$. This is the particular solution given by Eq. (2.14).

To better understand the mechanism of radiation generation we plot the Poynting flux, Eq. (2.8). It can be seen that only in the case of an increasing density ramp,

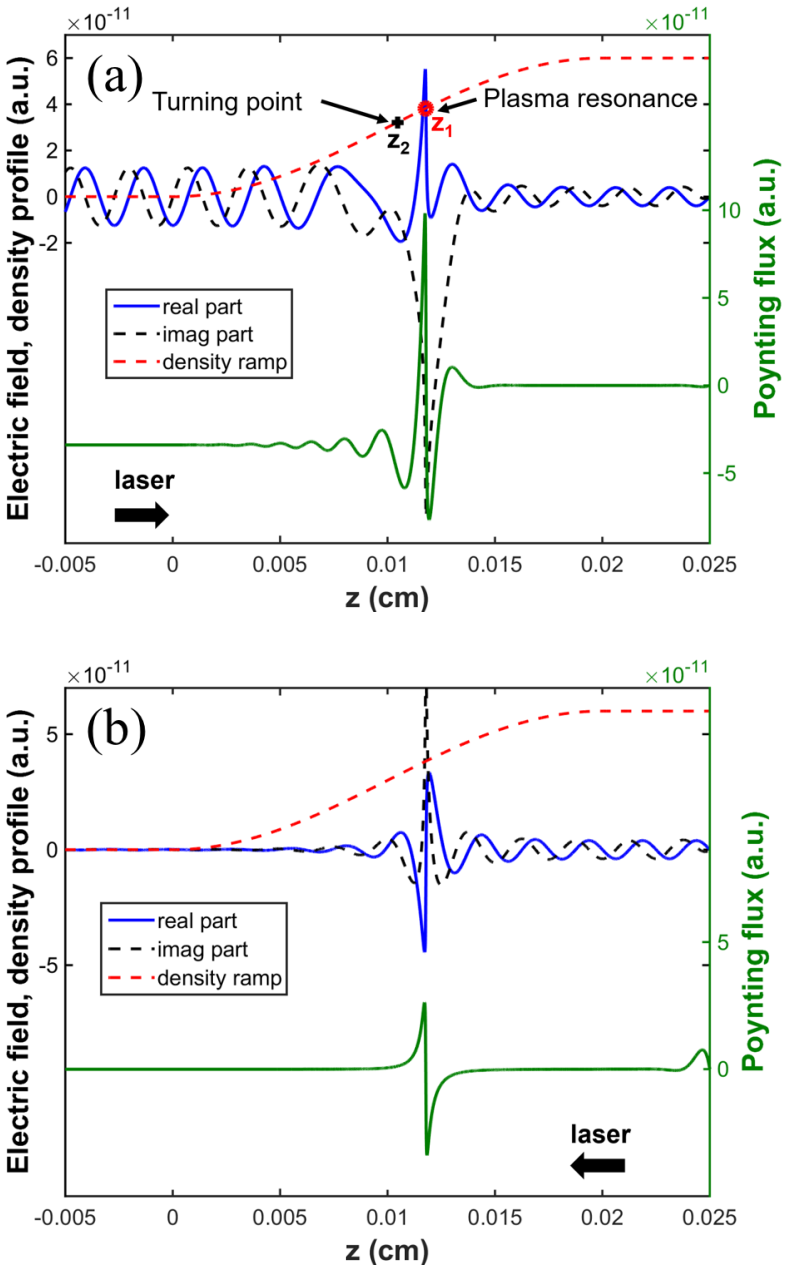

Figure 2.10: THz generation via resonant transition radiation in a diffuse (a) increasing and (b) decreasing density ramp. Shown are numerical result of the electric field described by Eq. (2.5) (real part, blue solid and imaginary part, black dashed), and the electron density profile (red dashed) with a 200 μm ramp length starting at $z = 0$ to $z = 200$ μm . The Poynting flux, described by Eq. (2.8), is also shown (green solid).

Fig. 2.10(a), is there an appreciable power flux leaving the plasma. The behavior of the Poynting flux in Fig. 2.10 shows that the THz radiation is generated at the plasma resonance z_1 , where its frequency matches the local plasma frequency, i.e., the dielectric function $\epsilon(z_1) = 0$. This is evidenced by the jump in Poynting flux that occurs near $z = z_1$. It is shown when the ramp length is much greater than the THz wavelength, the particular and homogeneous solutions of Eq. (2.5) decouple except at the resonance, and the Poynting flux is carried by the homogeneous solution. To escape the plasma, the THz radiation must first tunnel to the turning point z_2, where the wavenumber $k(z_2) = 0$, before it leaves the plasma and propagates into the vacuum. The oscillations in Poynting flux seen for $z < z_1$ are due to the beating of the laser generated particular solution of Eq. (2.5) and the homogeneous solution. This picture will be used to develop a scaling formula subsequently.

As can be seen by comparing Figs. 2.10(a) and 2.10(b) the radiation energy from an increasing ramp is greater than for a decreasing ramp. Further, comparison of the increasing and decreasing density cases displayed in Fig. 2.11 shows that the power radiated in the increasing ramp exceeds that of the sharp boundary radiation, which in turn, exceeds the power radiated in the decreasing ramp. The generation of wake fields in the uniform plasma displayed in Fig. 2.11 is identical since the laser parameters remain the same. This agrees with the PIC simulations discussed in the context of Fig. 2.6 as well as the analytical calculation confirming this phenomena presented in Fig. 2.9.

We now compare the spectra of THz radiation predicted by the PIC simulations and by numerical solution of Eqs. (2.5-2.11). Fig. 2.13 shows the energy

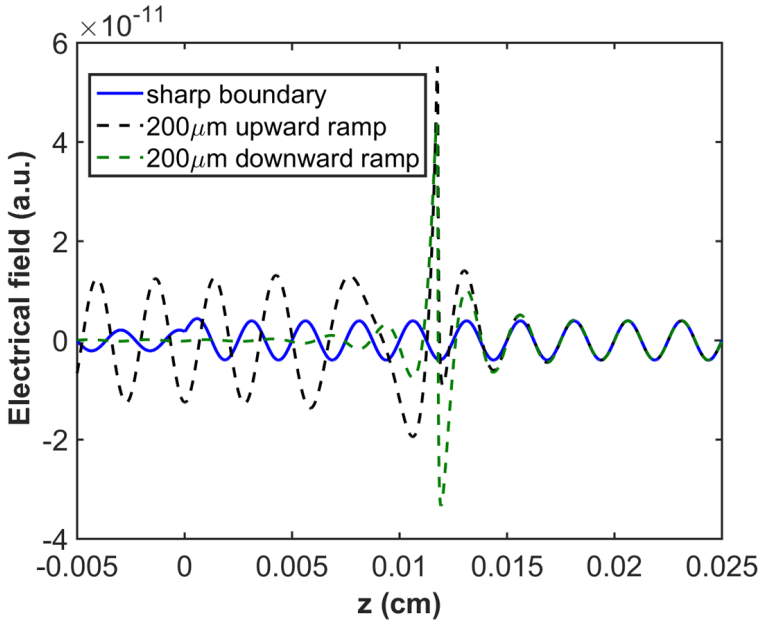

Figure 2.11: Comparison of THz generation in different density ramps. Shown are numerical results of the generated electric field described by Eq. (2.5) in a sharp vacuum-plasma boundary (blue, solid), an upward/increasing density ramp (black dashed) and a downward/decreasing density ramp (green dashed). The density ramp has a 200 μm ramp length between $z = 0$ and $z = 200$ μm.

per unit length and frequency ($dU'/d\omega$ in Eq. (2.7a)) versus frequency for several increasing ramps of varying length.

The curves match closely except for a small interval of frequencies near the maximum plasma frequency. This difference could be due to the finite transverse size of the plasma in the PIC simulations or the slight difference in the density profiles. The PIC simulation has a fifth order polynomial representation of the density profile while the differential equation was solved for a sine-squared profile.

The dependence of the radiated flux, $S_z(\omega, k_x)$ defined by Eq. (2.8), on transverse wavenumber is shown in Fig. 2.13(a) for $\omega_1 = 0.6\omega_{p0}$, where ω_{p0} is the max-

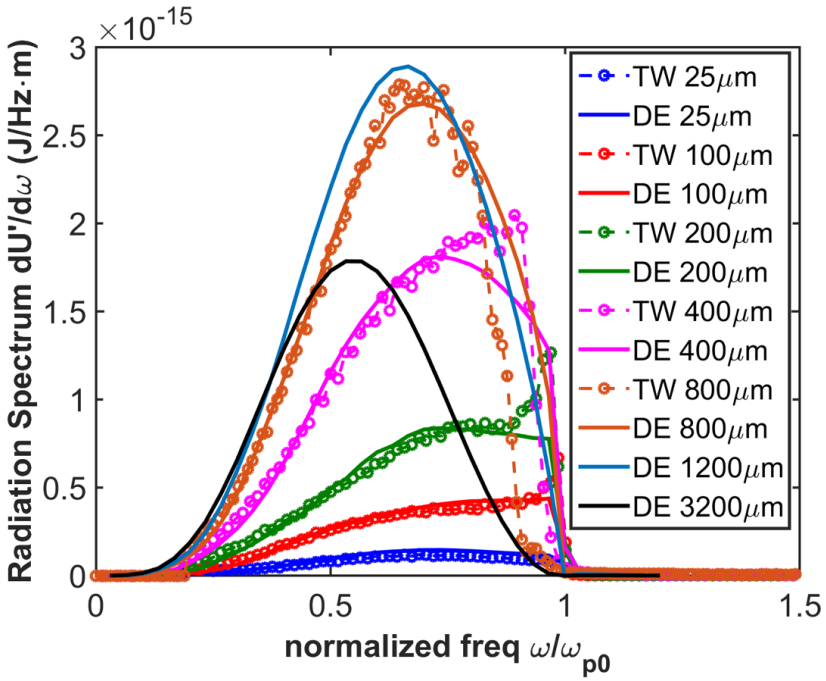

Figure 2.12: Comparisons of radiated spectral density between TurboWAVE and the proposed model for different increasing ramp lengths. Shown are TurboWAVE (TW) simulation results (dash, circle marker) and numerical results from the differential equation (DE) based on our developed model (solid) for different ramp lengths up to 3200 μm . Integration over frequency gives the total amount of radiated energy in 2D geometry; for example, the total energy is 0.1375 J/m for ramp length of 1200 μm , which is an enhancement of $\sim$50 times compared with 0.0027 J/m for the sharp boundary case.

imum plasma frequency. The flux is peaked at a wavenumber that decreases as the ramp length increases. This is shown in Fig. 2.13(b) where the wavenumber for the peak of the flux is plotted versus ramp length. The dependence of the peak wavenumber on scale length is a power law with a best-fit exponent -0.3274. For wavenumbers above the peak value the flux decreases rapidly, and the rate of decrease increases with ramp length.

We now propose a simple scaling formula for the dependence of the radiated THz energy on ramp length based on the picture suggested by Fig. 2.10(a). In our model, THz radiation is first generated by the laser pulse at the plasma resonance $\epsilon(z_1) = 0$, and it must tunnel to the turning point z_2, where $\omega^2\epsilon(z_2) - k^2c^2 = 0$. In the interval $z_2 < z < z_1$ the THz radiation has an imaginary wavenumber $k(z) = \omega^2\epsilon(z)/c^2 - k^2 = i\kappa$. If we assume that the density varies linearly with distance for $z_2 < z < z_1$, then $\epsilon(z) = -(z - z_1 - iZ_\nu)/L_0$ and $z_2 = z_1 - L_0k_x^2c^2/\omega^2$ where L_0 is the characteristic length defined by Eq. (2.17) and $Z_\nu = L_0\nu/\omega$. The THz radiation power escaping the plasma will then have a dependence on parameters due to the tunneling factor

$$S_h \propto \exp\left(-2\int_{z_2}^{z_1}\kappa(z)dz\right) = \exp\left(-\frac{4}{3}k_x^3L_0c^2/\omega^2\right). \tag{2.27}$$

This dependence on transverse wavenumber will apply as long as the turning point z_2 and the plasma resonance z_1 are well separated.This in turn implies k_x^2 is larger than a critical value that is displayed in Fig. 2.13(b).

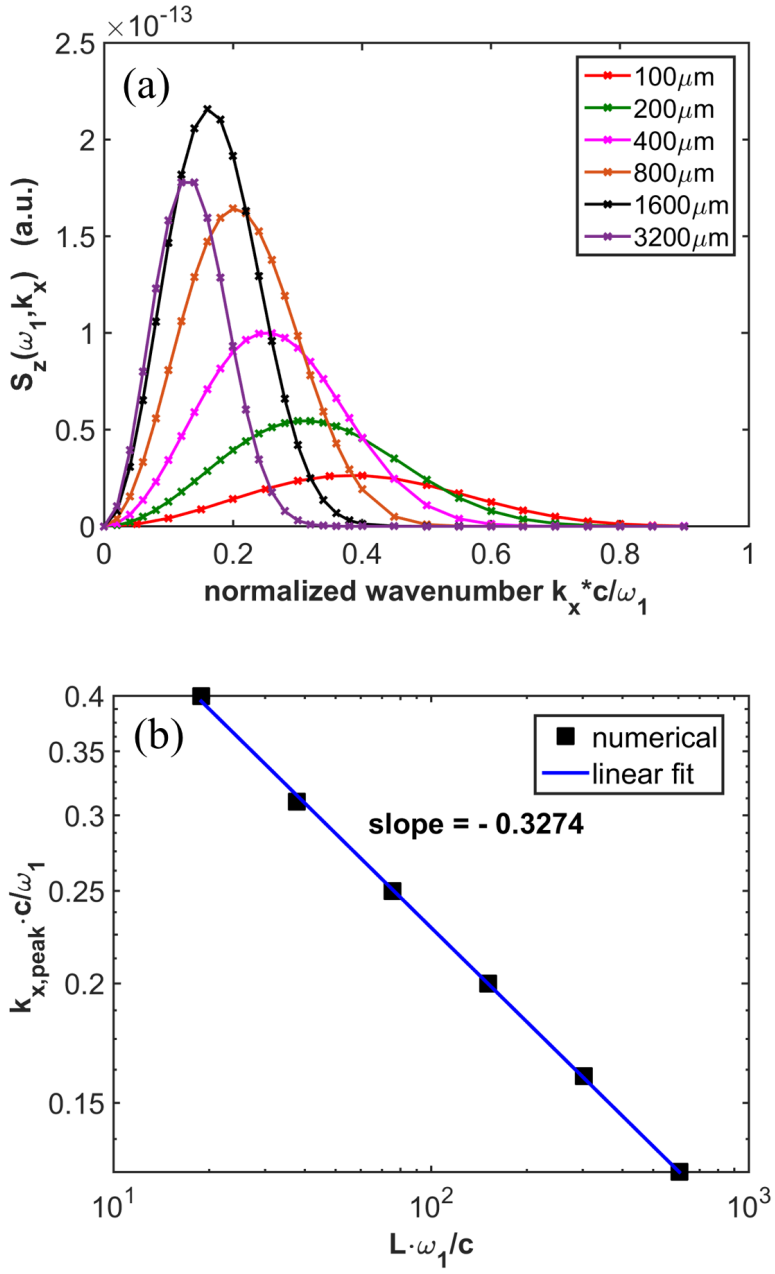

Figure 2.13: (a) Comparisons of Sz (Eq. (2.8)) at a particular radiation frequency $\omega_1 = 0.6\omega_{p0}$ for different increasing ramp lengths. Shown are numerical results of our developed model (solid, cross marker) for different ramp lengths up to 3200 μm. (b) Peak radiation angle (corresponding k_x) agrees with our model $k_{x,peak}c/\omega \sim (c/L_0\omega)^{1/3} << 1$.

To estimate the critical value of the transverse wavenumber we examine the differential equation, Eq. (2.5), for small $k_x^2c^2/\omega^2$ where the turning point z_2 and resonance z_1 are close together. We introduce a new axial coordinate, $\zeta = \mu(z - z_1 - iZ_\nu)$, where μ is a scale factor to be determined. We make the following replacement in Eq. (2.5), $\epsilon = -\zeta(L_0\mu)^{-1}$, $k^2 = -k_z^2\zeta(L_0\mu)^{-1} - k_x^2$ and $dz = d\zeta/\mu$, where $k_z = \omega/c$. This transforms Eq. (2.5) to the following,

$$\frac{d}{d\zeta}\left(\frac{\zeta}{\zeta+\zeta_k}\frac{d}{d\zeta}\bar{E}_x\right) - \frac{k_z^2}{\mu^3 L_0}\zeta\bar{E}_x = \frac{k_z^2}{\mu^2}S(z)\ . \tag{2.28}$$

where $\zeta_k = k_x^2 L_0\mu/k_z^2$ and the source $S(z)$ is given in Eq. (2.5).

We now pick a value of the scale factor μ so that both terms on the left of Eq. (2.28) are the same size, which leads to $\mu = (k_z^2/L_0)^{1/3}$. Next, we notice that the turning point $\zeta = -\zeta_k$ and the resonance $\zeta = 0$ will be close together when $\zeta_k = 1$ or $k_{x,peak}c/\omega \sim (c/L_0\omega)^{1/3} << 1$. This determines the radiation angles (corresponding to $k_{x,peak}$) where the peak of THz radiation exists as shown in Fig. 2.13(a), and is in agreement with the scaling of Fig. 2.13(b).

We also estimate the size of the electric field in this case from Eq. (2.28), $\bar{E}_x \sim (k_z L_0)^{2/3} S$ and the source is evaluated as $S \sim -ik_x k_z^2 \mu^{-2}\hat{V}_p q_e^{-1}\exp(ik_z z)$, therefore we have the following expressions,

$$\bar{E}_x \sim -ik_z^2 L_0 \frac{\hat{V}_p}{q_e}\exp(ik_z z)\ , \tag{2.29a}$$

$$\frac{d\bar{E}_x}{dz} \sim i\mu\bar{E}_x \sim \left(k_z^4 L_0\right)^{2/3}\frac{\hat{V}_p}{q_e}\exp(ik_z z)\ . \tag{2.29b}$$

Using Eqs. (2.29), the peak value of S_z as appears in Fig. 2.13(a) is estimated to be,

$$S_{z,peak} \sim \frac{c}{16\pi^3} k_z^2 \left(k_z L_0\right)^{5/3} \left(\frac{\hat{V}_p}{q_e}\right)^2 . \tag{2.30}$$

The radiated spectral density which is the integral of S_z according to Eq. (2.7a) can be further estimated as the product $S_{z,peak} k_{x,peak}$ and scales as $L_0^{4/3}$. Based on this analysis one would expect the radiated spectral density $dU'/d\omega$ to increase monotonically with density scale length L_0. However, as observed in Figs. 2.7 and 2.13 the radiated spectral density reaches a maximum for $L_0 = 1200$ μm and then decreases. This is explained by the presence of collisional damping. First there is local damping near $z = z_1$ where the THz is generated at the plasma resonance. It is already shown in Eq. (2.26) that the generated radiation is reduced by a factor $T_L = \exp\left(-2\omega Z_\nu/c\right) \sim \exp\left(-\alpha_L \nu L/c\pi\right)$ due to collisions. Another reduction due to damping occurs during propagation from the turning point to vacuum, i.e.,

$$T_P = \exp\left(2\int_{z_2}^{0} \left| Im\left(\sqrt{k^2}\right)\right| dz\right) \sim \exp\left(-\alpha_P \nu L/c\pi\right) . \tag{2.31}$$

Therefore, the scaling formula for the radiated THz spectral density shown in Fig. 2.7 can be approximated as the following,

$$\frac{dU'}{d\omega} = \left(\frac{\omega}{c}\right)^3 \left(\frac{\hat{V}_p}{q_e}\right)^2 \left(\frac{\omega}{c} L_0\right)^{4/3} \exp\left[-\left(\alpha_L + \alpha_P\right) \frac{\nu L}{c\pi}\right] . \tag{2.32}$$

where α_L and α_P both depend on radiation frequency ω. Formula (2.32) matches well with the results based on solution of Eq. (2.5) as well as the PIC simulations shown in Fig. 2.7.

Finally, to further investigate the radiated energy in the decreasing ramp, we conducted PIC simulations using different ramp lengths. As predicted by our model, both PIC simulations and numerical solutions of Eq. (2.5) show that the amount of THz generated dramatically decreases in the case of a decreasing ramp. In fact, one can conclude that the THz generated in the decreasing ramp case is negligible (3 orders of magnitude less) compared with the amount of THz generated in the increasing density ramp case. The cause of this asymmetry is a form of phase matching as discussed previously.

2.4 Conclusions

We have both theoretically and numerically investigated ponderomotively driven resonant THz transition radiation generated at plasma boundaries. Broad-band THz radiation is generated with frequencies up to the maximum plasma frequency. The parameters of the driving pulse as well as the plasma profiles affect the properties of the generated THz radiation. The spectrum and angular distribution of the THz radiation can also be tuned by varying these parameters.

Resonant transition radiation is generated at a diffuse plasma boundary and is preferentially enhanced if the laser pulse propagates through an increasing density

profile. We've developed a model to describe the physical processes in this diffuse plasma case. The THz is generated primarily at the plasma resonance and must tunnel to a turning point before it leaves the plasma and propagates into vacuum. The calculated Poynting flux shows that this process enhances the amount of THz energy efficiently through a density increasing ramp and diminishes THz generation through a decreasing density ramp. A scaling law was developed to allow one to estimate the amount of THz energy generated for different density ramp lengths.

Both numerical solutions of Eq. (2.5) and PIC simulations agree with our model. The amount of THz radiation generated can be dramatically increased compared with that in the sharp vacuum plasma boundary case [64]. As an example, a fixed driver pulse (1.66 J) excites approximately 422.9 μJ of THz radiation in a 1.2 mm increasing density ramp. Thus this mechanism provides the possibly of developing new high power tunable THz sources.

2.5 Appendix A: NUMERICAL METHOD FOR EQUATION (2.5)

In Sec. 2.3, we presented numerical results of solutions for the electric field $\bar{E}x$ determined by Eq. (2.5). Here we present details of the method. Eq. (2.5) can be put in the general form,

$$\frac{d}{dz}\left(p(z)\frac{d}{dz}\bar{E}_x\right) + q(z)\bar{E}_x = S(z)\ , \tag{2.33}$$

where $p(z) = \epsilon(z)/k^2(z)$, $q(z) = \epsilon(z) = 1 - \omega_p^2(z)/\omega(\omega + i\nu)$ and $k^2(z) = \omega^2\epsilon(z)/c^2 -$

k_x^2.

We take $z = 0$ to be the boundary between the plasma and vacuum. One boundary condition is that the field $\bar{E}x$ should be an outgoing wave in vacuum ($z < 0$). Thus for $z < 0$, in vacuum,

$$\bar{E}_x = C_1 \exp\left(-ik_1 z\right) . \tag{2.34}$$

We assume the density is uniform for $z > L$ where L is the ramp length, then

$$\bar{E}_x = C_2 \exp\left(-\kappa z\right) + E_p(z) , \tag{2.35}$$

where C_1, C_2 are two constants to be determined and $k_1^2 = \omega^2/c^2 - k_x^2$ and $\kappa^2 = k_x^2 - \frac{1}{c^2}\left(\omega^2 - \frac{\omega_{p0}^2}{1+i\nu/\omega}\right)$. The function E_p is the particular solution described by Eq. (2.14). The homogeneous solutions are exponentially growing and decaying with z for $z > z_2$ (see Fig. 2.10). Thus, direct integration of Eq. (2.33) for large ramp lengths is subject to errors. To overcome this, we then use the method of variation of parameters by first considering two homogeneous solutions u_1 and u_2 of Eq. (2.33) (taking the source term $S(z) = 0$), which satisfy the following boundary conditions,

$u_1(z)$: $\quad u_1(z) \to 0$ as $z \to +\infty$, and

$u_2(z)$: $\quad u_2(z) \to$ outgoing wave as $z \to -\infty$.

We then write the general solution of Eq. (2.33) in the following form,

$$\bar{E}_x = A_1(z)u_1(z) + A_2(z)u_2(z) \ . \tag{2.36}$$

Since we have introduced two functions, A_1 and A_2, to represent a single unknown, we are free to make up a second relation between them,

$$u_1 \frac{dA_1}{dz} + u_2 \frac{dA_2}{dz} = 0 \ . \tag{2.37}$$

Substituting Eq. (2.36) into Eq. (2.33) and applying the condition (2.37), one arrives at equations for the two functions, A_1 and A_2,

$$\frac{dA_1}{dz} = -\frac{u_2 S}{W} \ , \tag{2.38a}$$

$$\frac{dA_2}{dz} = \frac{u_1 S}{W} \ . \tag{2.38b}$$

The quantity W is the Wronskian defined as,

$$W = p\left(u_1 \frac{du_2}{dz} - u_2 \frac{du_1}{dz}\right) \ , \tag{2.39}$$

and W is independent of z. As an example, shown in Fig. 2.14 is the Wronskian formed from numerical solutions for u_1 and u_2 for a 200 μm increasing density ramp. Other parameters are the same as in Sec. 2.3. The relative variation is within 0.005%.

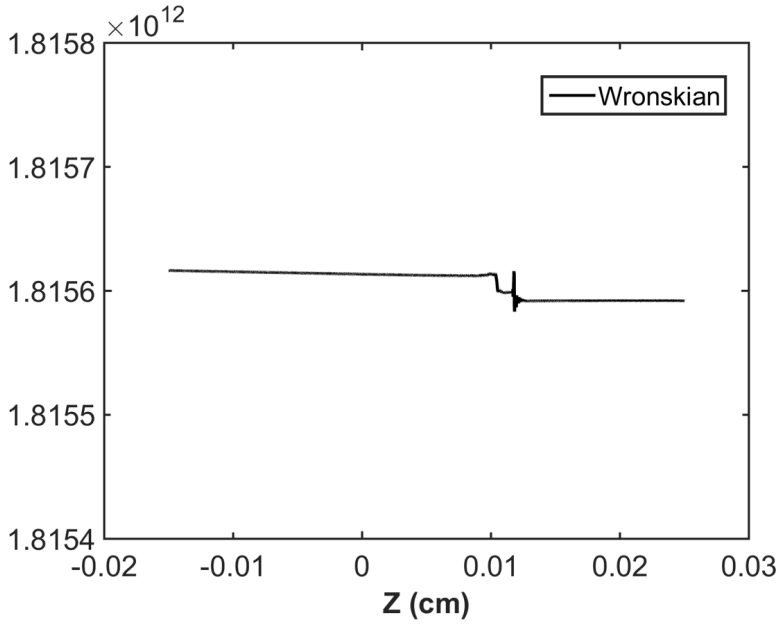

Figure 2.14: Wronskian described by Eq. (2.39) for a 200 μm increasing density ramp.

After obtaining the Wronskian from the simulation, we can further numerically solve for the two coefficient functions, A_1 and A_2, and finally obtain the generated THz field $\bar{E}_x$ in vacuum, $z < 0$. In Sec. 2.3, Fig. 2.10 is an example of the simulation result for a particular radiation frequency and transverse wavenumber. Scanning over all possible radiation frequencies and wavenumbers is conducted to obtain the total radiated THz energy into vacuum using Eq. (2.15).

Chapter 3: High-Power Tunable THz Generation in Corrugated Plasma Waveguides

3.1 Overview

Terahertz radiation (THz) has a wide variety of applications [1] including time domain spectroscopy (TDS) [2], medical and biological imaging [4], remote detection [3] and so on. For example, most airports use millimeter wave/THz scanners for security checking. Research in small-scale, high efficiency terahertz sources has been actively conducted to investigate THz radiation generation by laser pulses propagating in plasmas since it was first demonstrated by Hamster et al. [12, 13]. In this case, the source of the radiation is the current driven by the ponderomotive force of a laser pulse. However, generation of radiation by laser pulse propagating through uniform plasma is generally minimal. In order for these electromagnetic modes to efficiently couple to the driving source which travels at its group velocity, the plasma must be inhomogeneous or a strong background magnetic field is required. A scheme involving laser pulses (or possibly electron beams) propagating through axially corrugated plasma channels has been proposed by Antonsen et at. [33, 67]. This slow wave structure supports electromagnetic modes that have subluminal

phase velocities, thus providing the possibility of phase matching between the excited modes and the driver.

In this chapter we report the theoretical and simulation results of investigating the ponderomotively driven THz generation via the slow wave phase matching process by laser pulses propagating through corrugated plasma waveguides. Such corrugated plasma waveguides support electromagnetic (EM) channel modes with subluminal phase velocities, thus allows the phasing matching between the generated THz modes and the ponderomotive potential associated with laser pulse, making significant THz generation possible. These waveguides have been reported routinely demonstrated in the lab [43, 44] and the experimental set up is shown in Fig. 3.1a. A first Nd:YAG laser is line-focused onto a cluster jet and the hydrodynamic expansion process forms the channel. The periodic structure is created by spatial modulation of laser intensity or the cluster density. A second ultra-short Ti:Sapphire laser pulse is then sent into the channel with some time delay following the channel formation pulse and it drives the terahertz generation. Shown in Fig. 3.1b is a snap shot of the experimentally generated axially modulated plasma density profile. Full format PIC simulations and theoretical analysis are conducted to investigate this slow wave phase matching mechanism. We find the generated THz is characterized by lateral emission from the channel, with a spectrum that may be narrow or broad depending on laser intensities. A range of realistic laser pulse and plasma profile parameters are considered with the goal of maximizing the conversion efficiency of optical energy to THz radiation. As an example, simulation results show a fixed driver pulse (0.55 J) with spot size of 15 μm and pulse duration of 15 fs excites approximately 37.8

mJ of THz radiation in a 1.5 cm corrugated plasma waveguide with an averaged on axis density of $1.4 \times 10^{18}\ cm^{-3}$, conversion efficiency exceeding 8% can be achieved in this case.

The organization of this chapter is as follows. In Sec. 3.2, we introduce the mechanism and provide the principles of generating THz in corrugated plasma waveguides. A mathematical model of the channel is considered and dispersion relation is analyzed to determined the frequency of channel mode excitation. In Section. 3.3, we conduct full format PIC simulations to investigate how to optimize the conversion efficiency from laser pulse energy to THz. In addition, THz spectrum tunability is also discussed. A numerical method to precisely find the mode frequencies and how many modes can escape the plasma is also provided. The dependence of THz radiation on plasma density, driver pulse intensity, laser pulse duration, channel length and other channel parameters is investigated and discussed in detail. Two different types of experimentally demonstrated plasma channels are considered and compared. In Section. 3.4 we present our conclusions and discuss future directions.

3.2 Excitation of THz modes in corrugated plasma channels

3.2.1 Ponderomotive Driver

Our goal is to study the possibility of a high-power, tunable table-top THz source. In order to efficiently generate terahertz radiation by passing an ultra short, intense laser pulse through a corrugated plasma channel, there are a number of con-

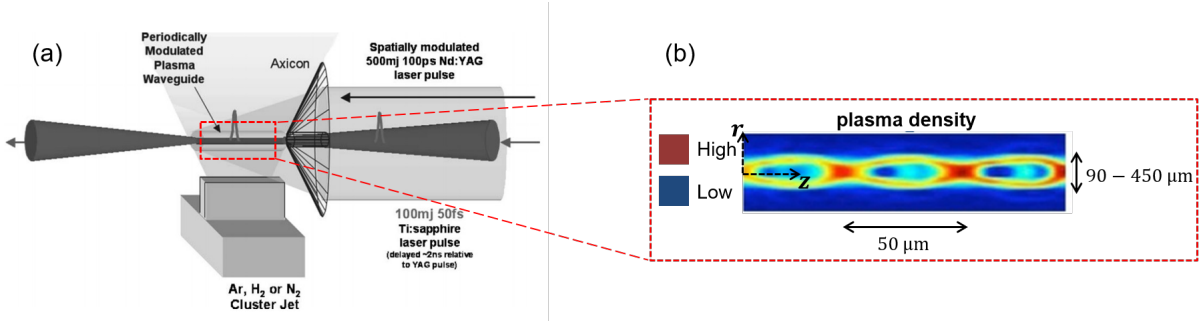

Figure 3.1: (a) Diagram of experimental setup for generation of an axially corrugated plasma channel. To create the plasma structures, a modulated cluster density can be used in conjunction with a uniform formation pulse or one can spatially modulate the formation pulse alternatively. (b) Snapshot of an experimentally generated axially modulated plasma channel (only 3 periods are shown here).

ditions to be satisfied. First, if the interaction takes place in a tenuous plasma, the central frequency of the driver pulse will be significantly higher than the generated electromagnetic waves. The laser pulse produces a cycle-averaged low frequency ponderomotive force on the electrons, which induces an electron current that can produce radiation. The force on electrons is the gradient of the ponderomotive potential of the pulse, $\boldsymbol{F_p} = -\boldsymbol{\nabla} V_p$, where $V_p = mc^2a^2/4$ in terms of the normalized laser vector potential $a = eE_a/mc\omega_0$, m is the electron mass, e is the electron charge and c is the speed of light in vacuum. ω_0 is the laser carrier frequency and E_a is the electric field amplitude with both spatial and temporal distributions. The plasma ions are relatively heavy and can be treated as stationary background during the interaction time scale. The rate at which the ponderomotive force does work on a current is given by

$$P = \int d^3x \boldsymbol{J} \cdot \boldsymbol{\nabla} V_p/q = -\int d^3x V_p \frac{\partial n}{\partial t} \ , \tag{3.1}$$

where $q = -e$ is the electron charge, $\boldsymbol{J}$ is the current and n is the electron density. Eq. (3.1) implies that in order for the laser pulse energy to be efficiently converted into electromagnetic (EM) modes in the perturbation regime, a density perturbation is required. This can be satisfied in an inhomogeneous plasma or a strongly magnetized plasma.

Secondly the phase velocity of the excited channel modes must be phased match to the group velocity of the laser pulse in the plasma to have significant THz emission. In a uniform plasma, the modes typically have superluminal phase velocities by simply regarding the dispersion relation $\omega^2 = k^2c^2 + \omega_p^2$, where $\omega_p = \sqrt{4\pi e^2 n/m}$ is the plasma frequency. However, the phase matching condition is possible in a corrugated plasma channel. The periodicity of the channel makes it a slow wave structure, and the electromagnetic modes of these channels have the Floquet type dispersion relations as discussed in Sec. 3.2.3. The frequencies of the channel modes are determined by the channel parameters and each mode of channel consists of the sum of spatial harmonics [34]. Because of the superposition of spatial harmonics, these EM modes can have subluminal phase velocities. Thus, significant THz emission may be achieved.

3.2.2 Corrugated Plasma Channels

We consider the corrugated plasma waveguides to be cylindrical symmetric, with electron densities described by the following,

$$\frac{n(r,z)}{n_{00}} = \begin{cases} n_0 + (n_1 - n_0)\dfrac{r^2}{r_c^2} & r \le r_c \\ n_1 \dfrac{r_0 - r}{r_0 - r_c} & r_c < r < r_0 \\ 0 & r \ge r_0 \end{cases} \tag{3.2}$$

where n_{00} is a normalization density. The channel has a density modulation period of λ_m and the modulation wavenumber is defined as $k_m = 2\pi/\lambda_m$. Here the axially modulated z dependence is carried through the parameters n_0, n_1, r_c and r_0. The quantity $n_0(z)$ is the normalized on-axis density and $n_1(z)$ is normalized density at $r = r_c$ as shown in Fig. 3.2. The quantities n_0 and n_1 are both axially modulated, $n_0 = 1+\delta \sin(k_m z)$ and $n_1 = \overline{n}_1 + \delta_1 \sin(k_m z)$, respectively. Here δ is the modulation amplitude of the on-axis density n_0. The quantity $\overline{n}_1$ is the average transverse peak density and δ_1 is the modulation amplitude of n_1. The density has a parabolic transverse profile to guide the laser pulse during propagation. The quantity r_c is the radius at which n_1 characterizes the density, and the density then decreases linearly to zero between r_c and r_0. The quantities r_c and r_0 may also be axially modulated. Figs. 3.2a and 3.2b are false color images of two different types of the modeled density profiles, both of them are experimentally demonstrated.

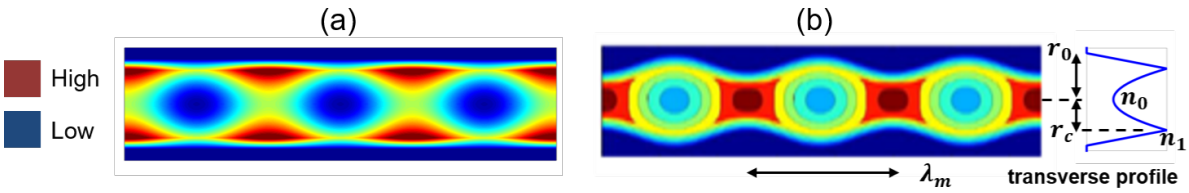

Figure 3.2: False color image of two example electron density profiles generated by Eq. (3.2): (a) a channel with maximum density at lateral edges, with $\delta_1 = \delta = 0.7$, $\overline{n}_1 = 1.3$, $r_c = 30\ \mu m$ and $r_0 = 40\ \mu m$. (b) a channel with maximum density at the center, with $\delta = 0.7$, $\overline{n}_1 = 1.3$, $\delta_1 = 0.1$. Both cut-off radius and channel radius are also modulated as $r_c[\mu m] = 22.5 - 7.5\sin(k_m z)$ and $r_0[\mu m] = r_c + 15$.

3.2.3 Dispersion Relation and Mode Excitation

We assume the plasma is a cold fluid with linear response and consider the radially polarized, azimuthally symmetric TM modes (E_r, E_z, B_θ) of the channel. Following Maxwell's Equations, an approximate wave equation [33, 34] for transverse electric field E_r can be derived

$$\left(-\frac{1}{c^2}\frac{\partial^2}{\partial t^2} + \frac{\partial^2}{\partial z^2} + \frac{1}{r}\frac{\partial}{\partial r} r \frac{\partial}{\partial r} - \frac{1}{r^2} \right) E_r = \frac{\omega_{p0}^2}{c^2}\frac{n(r,z)}{n_{00}} E_r \ , \tag{3.3}$$

where ω_{p0} is the plasma frequency evaluated for the normalization density n_{00}. Here we have assumed $|\boldsymbol{\nabla}\cdot\boldsymbol{E}| << |\boldsymbol{E}|/r_c$. This equation is exact in the case of TE mode with E_r replaced by E_θ.

In the case which the channel is parabolic as $r \to \infty$ and only characterized by the first line of Eq. (3.2), we assume $\delta_1 = \delta$ and consider the γth order of radial

eigenmode of the channel can be described by

$$E_r(r,z,t) = E_0 f(z) H_\gamma\left(\frac{r}{w_{ch}}\right)\exp\left(-\frac{r^2}{w_{ch}^2}\right), \tag{3.4}$$

where w_{ch} is the mode width given by $4/w_{ch}^4 = \omega_{p0}^2(n_1 - n_0)/r_c^2c^2$ and and we require $w_{ch} < r_c$. H_γ is the γth odd polynomial defined as $\sum_{n=1}^{n=2\gamma-1}\alpha_n\left(r/w_{ch}\right)^n$ with coefficients determined by $\alpha_n/\alpha_{n-2} = 4(n-1-2\gamma)/(n^2-1)$, $a_1 = 1$ and $a_0 = 0$. The function $f(z)$ satisfies the following Mathieu equation,

$$\frac{d^2f}{dz^2} + k_0^2 f = \frac{\omega_{p0}^2}{c^2}\delta\sin\left(k_m z\right)f\ , \tag{3.5}$$

Here, the value of k_0 is defined such that

$$\omega^2 = \omega_{p0}^2 + \frac{8\gamma c^2}{w_{ch}^2} + k_0^2c^2\ . \tag{3.6}$$

The dispersion relation is found by solving Eq. (3.5) with Floquet boundary conditions, $f(z+\lambda_m) = \exp\left(ik_z\lambda_m\right)f(z)$. The parameter k_0 depends implicitly on the phase advance per period $k_z\lambda_m$ and can be numerically found [34]. Then $k_0(k_z)$ inserted in Eq. (3.6) gives $\omega(k_z)$ the dispersion relation.

Shown in Fig. 3.3 is the dispersion relation for the lowest ($\gamma = 1$) radial mode of the model channel. The dependence of ω on phase advance demonstrates the characteristic periodicity of frequencies in k space for periodic structures. The laser

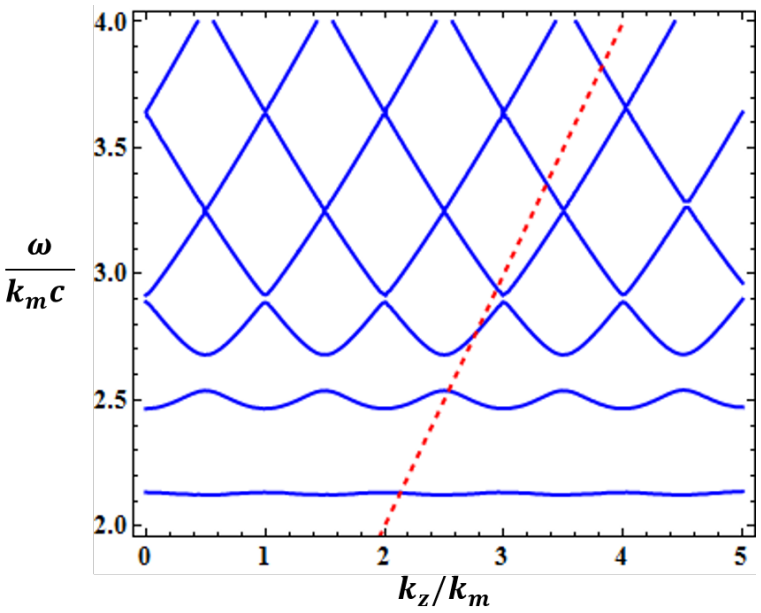

Figure 3.3: Dispersion relation curves of the lowest (fundamental) radial mode of a corrugated channel evaluated by Eq. (3.6) with $n_{00} = 1.4 \times 10^{18}\ cm^{-3}$, $\delta_1 = \delta = 0.9$, $\overline{n}_1 = 3$ and $r_c = 30\ \mu m$. The straight line (red) corresponds to the laser pulse moving at the speed of light, $\omega = k_z c$.

pulse, represented by a straight line in the plot, moves at its group velocity ($v_g \simeq c$) in the plasma channel. At places where the dashed pulse line and the dispersion relation curve intersect, phase matching occurs, and THz excitation can be expected of these frequencies.

Equations (3.5) and (3.6) apply as long as $w_{ch} < r_c$. Eq. (3.6) is a good approximation of the dispersion relation regarding the axially average density profile and assuming the transverse parabolic shape extends to infinity. However, to determine the exact frequencies of the excited modes, one can numerically evaluate the wave equation Eq. (3.3) using an exact electron density profile. A discussion of the more accurate calculation of dispersion relation, including the comparison with Eq. (3.6) is provided in Sec. 3.3.1.

3.3 Simulation Results

3.3.1 Radial eigenmodes

In this section, we discuss the numerical method to calculate the exact frequencies of the modes. Assuming the channel is axially uniform, Eq. (3.3) can be rewritten as,

$$\left(\frac{1}{r}\frac{\partial}{\partial r}r\frac{\partial}{\partial r} - \frac{1}{r^2}\right)E_r + \left(k_c^2 - k_p^2(r)\right)E_r = 0\,, \tag{3.7}$$

where the cut off wavenumber k_c of EM modes and plasma wavenumber k_p, are defined as, $k_c^2 = \omega^2/c^2 - k_0^2$ and $k_p^2(r) = \omega_p^2(r)/c^2$, respectively. Boundary conditions imply E_r vanishes on axis, i.e., $E_r(r = 0) = 0$. Outside the channel, $n(r > r_0) =$

Table 3.1: Exact values of numerically calculated k_c and estimation from Eq. (3.6) for different radial modes.

Mode number	$k_c[\mu m^{-1}]$, exact	$k_c[\mu m^{-1}]$, Eq. (3.6)
1st	0.30195	0.3024
2nd	0.36384	0.3652

0, thus Eq. (3.7) becomes the Bessel's differential equation. The field E_r outside the channel must match the properties of an outgoing wave. Thus it takes the form of the first kind Hankel function $H_1^{(1)}(k_c r)$, which asymptotically behaves as $E_r \sim \frac{1}{\sqrt{r}} \exp(ik_c r)$. The boundary condition allows us to know the ratio of E_r to its derivative outside the channel, and we can numerically integrate Eq. (3.7) using the shooting method to determine the k_c values that satisfy the on axis boundary condition $E_r(0) = 0$. Appendix A provides more details of this calculation.

The calculation of k_c for radial eigenmodes is displayed in Table 3.1 and match closely with the estimation $k_c = \sqrt{\omega_{p0}^2/c^2 + 8\gamma/w_{ch}^2}$ from Eq. (3.6).

3.3.2 PIC simulation results

3.3.2.1 THz Mode Excitation

THz generation in corrugated plasma waveguides is simulated using the full format PIC code TurboWAVE [62]. The simulations, performed in 2D planar geometry, employ a finite sized plasma channel illuminated by an ultra short, intense laser pulse incident from the vacuum. Figure 3.4(a) displays an example for a plasma channel of 10 periods with modulation wavelength $\lambda_m = 50\ \mu m$. To quantify the

radiation emitted from the plasma channel, we calculate the Poynting flux through each prescribed surface outside the plasma region, which captures the emission in the forward, backward and lateral directions. The 2D simulations are performed in the lab frame. The domain size is $102.4k_n^{-1} \times 374.8k_n^{-1}$ with 1024×20480 cells in the x and z directions, respectively, where $k_n^{-1} = 2.01115\ \mu m$ is the normalization used in the simulation. A laser pulse with central wavenumber $\lambda = 800\ nm$, duration $\tau_{FWHM} = 50\ fs$ and spot size 15 μm traverses the plasma channel from left to right. The normalized vector potential $a_0 = 0.4$ (pulse energy $U_L = 66\ mJ$) with a_0 defined as $a_0 = eE_0/mc\omega_0$, where E_0 is the peak field amplitude and ω_0 is the laser central frequency. Fig. 3.4(b) shows a false color image of the transverse component of Poynting flux P_x after the laser pulse traverses the channel. The plasma wave excitation can be observed as the rapid oscillations inside the channel and the alternate positive and negative values of the Poynting flux indicate a small average flux. However, at both lateral boundaries, one can observe the THz emission as the red and blue streaks denoting the lateral Poynting flux. The forward and backward radiation that is also observed at both the left and right ends of the channel in Fig. 3.4(b) is the resonant transition radiation due to inhomogeneity of plasma described previously[36, 65]. As we discussed in Sec. 3.2, the lateral THz emission that is not observed in uniform plasmas [36] is a result of to the excitation of subluminal EM modes in the modulated channel.

To further investigate the spectrum of the lateral THz emissions, the radiated energy per unit length U' through each diagnostic surface in Fig. 3.4(a) can be obtained in the form of a spectral density in $(\omega, \boldsymbol{r})$, where $\boldsymbol{r}$ denotes the 2D spatial

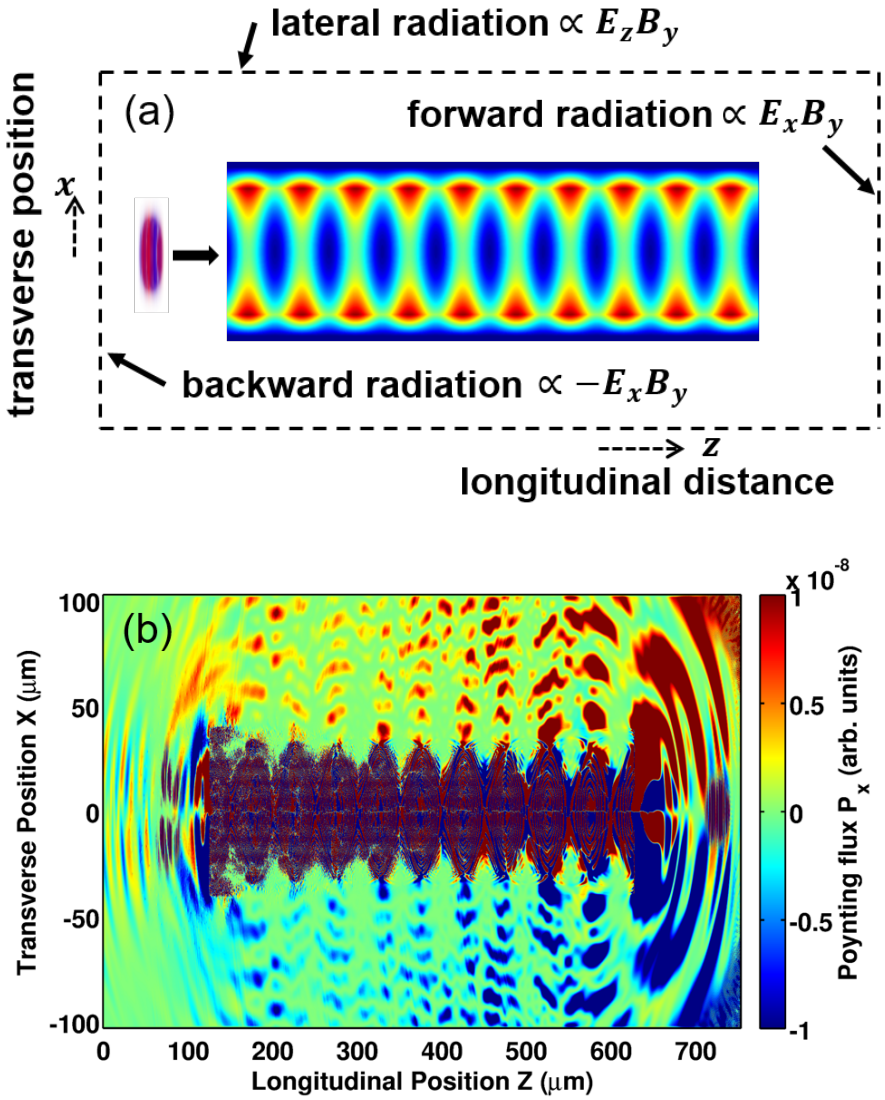

Figure 3.4: (a) Diagram of simulation set up. The diagnostic box is set outside the plasma channel and the Poynting flux through each surface is calculated. The plasma channel consists of 10 modulation periods with the following parameters: $\lambda_m = 50\ \mu m$, $n_{00} = 1.4 \times 10^{18}\ cm^{-3}$, $\delta_1 = \delta = 0.9$, $\overline{n}_1 = 3$, $r_c = 30\ \mu m$ and $r_0 = 40\ \mu m$. (b) A snap shot of the transverse component of Poynting flux $E_z B_y$ in PIC simulations after the laser propagates through the channel from left to right, with bright and dark streaks indicating lateral THz radiation is generated.

coordinates (x, z),

$$\frac{dU'}{d\omega} = \int dA\hat{\boldsymbol{n}} \cdot \boldsymbol{S}(\omega, \boldsymbol{r}) \tag{3.8a}$$

$$U' = \int_0^\infty d\omega \frac{dU'}{d\omega} \ , \tag{3.8b}$$

where $\hat{\boldsymbol{n}}$ is the unit vector normal to surface A. The spectral density is given by,

$$\boldsymbol{S}(\omega, \boldsymbol{r}) = \frac{c}{8\pi^2}\big(\boldsymbol{E}(\omega, \boldsymbol{r}) \times \boldsymbol{B}^*(\omega, \boldsymbol{r}) + c.c.\big) \ . \tag{3.9}$$

Therefore, to quantify THz radiation emitted across each diagnostic surface, we calculate the z component of the spectral density, S_z, for the left and right diagnostic boundaries and the x component, S_x, for the lateral boundary. Figure 3.5(b) is the radiated spectral density from the PIC simulations. The low frequency, broad-band THz radiation observed at the entrance of the channel also shown in Fig. 3.5(a) is the resonant transition radiation [36], however, lateral THz radiation [37] is also observed in the corrugated plasma channel and characterized by a coherent, narrow band spectrum as shown in Fig. 3.5(c). The frequencies of the first three excited THz modes based on our simplified model are 13.18 THz, 15.3 THz and 16.5 THz, respectively, as predicted by the phase matching condition in Fig. 3.3. In this case, the simulation shows that THz leaves the channel, creating a intensity pattern with maxima at the 9 separate locations along the longitudinal distance in Fig. 3.5(b) where the fundamental mode emits.

Figure 3.6(a) shows the spatial and temporal evolution of the Poynting flux

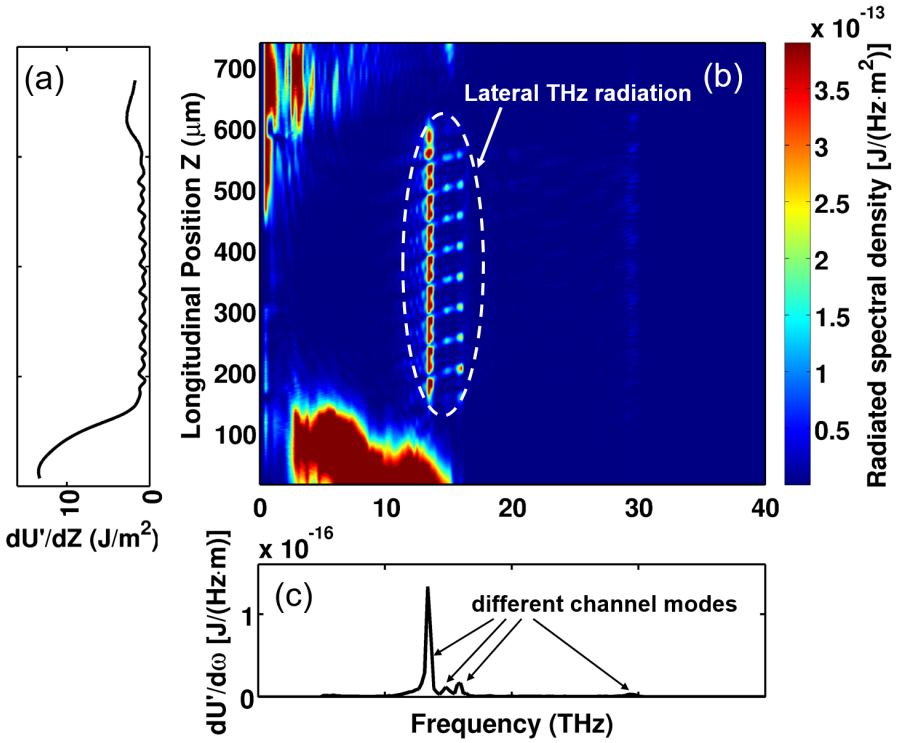

Figure 3.5: (a) Radiated THz energy across the lateral diagnostic boundary shows two different mechanisms of generating THz. (b) Simulation results of radiated THz spectral density across the lateral diagnostic boundary using the same channel parameters in Fig. 3.4(a) and $a_0 = 0.4$. Besides the low frequency, broad band THz radiation when laser pulse crosses the plasma interface, lateral THz radiation is also observed. (c) Radiated THz spectrum (only channel modes are considered in this plot) shows different channel modes are excited. The frequency of each excited mode matches well with the phase matching condition in Fig. 3.3.

P_x across the lateral boundary. As the driver pulse propagates through the channel, EM modes in the THz range are excited and escape the channel. Also observed in simulation results is that the lateral THz radiation propagates approximately perpendicularly to the lateral boundary. Shown in Fig. 3.6(b) is a typical temporal profile of the excited THz mode, with amplitude built up in a few THz cycles and then decreasing.

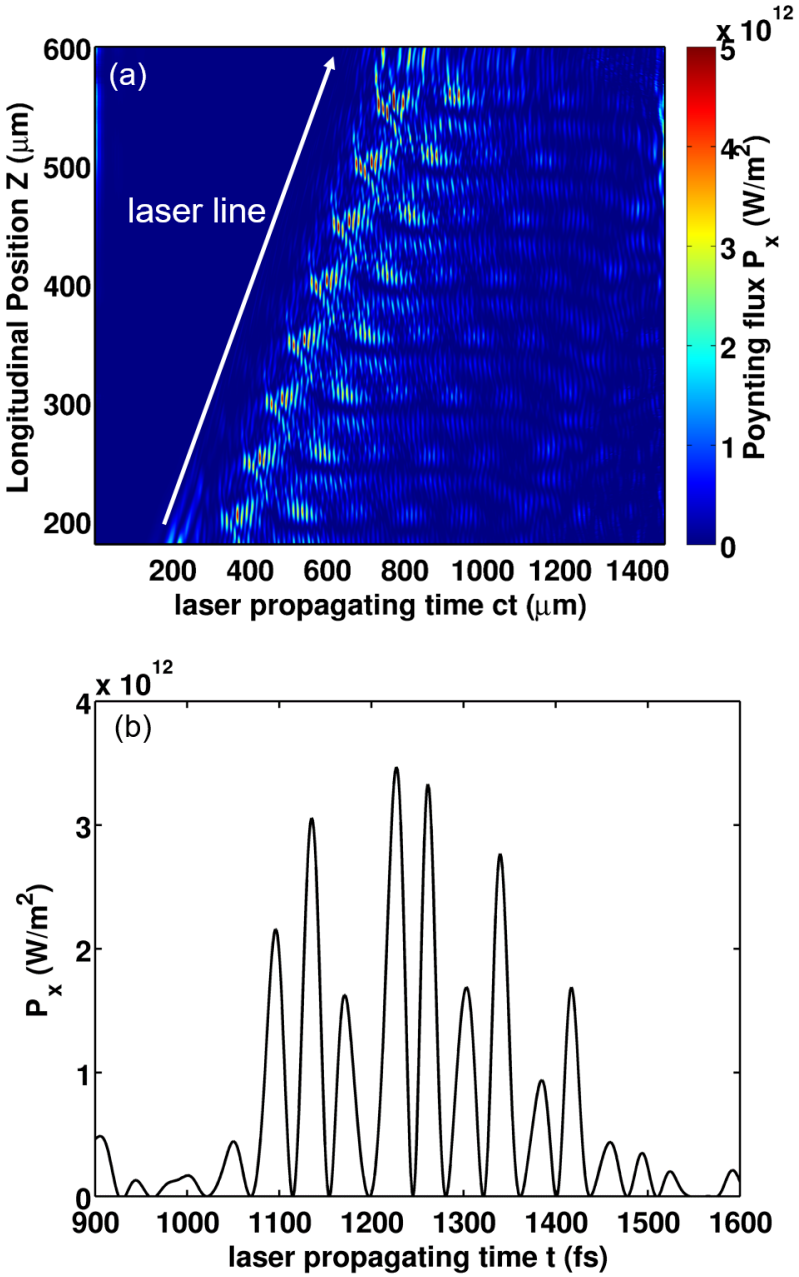

Figure 3.6: (a) False color image of the spatial and temporal evolution of Poynting flux P_x across the lateral diagnostic boundary from PIC simulations. Lateral THz emission of channel modes is observed. (b) A typical temporal profile of the excited THz mode, with frequency ∼12.5 THz.

3.3.2.2 Dependence on Plasma Density

Terahertz generation via the slow wave phase matching process depends on plasma density. As shown in Fig. 3.7(a), THz radiation generated from SWPM peaks around plasma density of $1.75 \times 10^{17}\ cm^{-3}$ for the parameters we used in the simulation. The fundamental mode of the channel contributes dominantly to the THz radiation for all the plasma densities considered in Fig. 3.7(a). As discussed in Ref. [33], the energy extracted from the driver pulse is essentially converted into both electromagnetic radiation (EM) and plasma waves (PW). Fig. 3.7(b) displays the radiated spectral density $dU'/d\omega$, as the plasma density is reduced, the frequency of the fundamental mode decreases, and most importantly, the ratio of the generation of electromagnetic radiation at these frequencies over plasma waves increases. In particular, at the averaged on axis density around $1.75 \times 10^{17}\ cm^{-3}$, the THz generation peaks at the fundamental frequency of 6.6 THz corresponding to the local maxima of coupling. This means more energy extracted from the driver pulse is converted into THz radiation due to the fact that the central channel density is tending low and the excitation of plasma waves becomes small.

3.3.2.3 Dependence on Laser Intensity

Ponderomotively driven radiation is expected to scale quadratically as the laser intensity, i.e., $a_0^4/\gamma^2 \sim a_0^4/(1 + a_0^2)$. From the simulation results shown in Fig. 3.8, one can see THz radiation can be enhanced by increasing the laser intensity. However, for larger a_0, the THz radiation is enhanced above the scaling

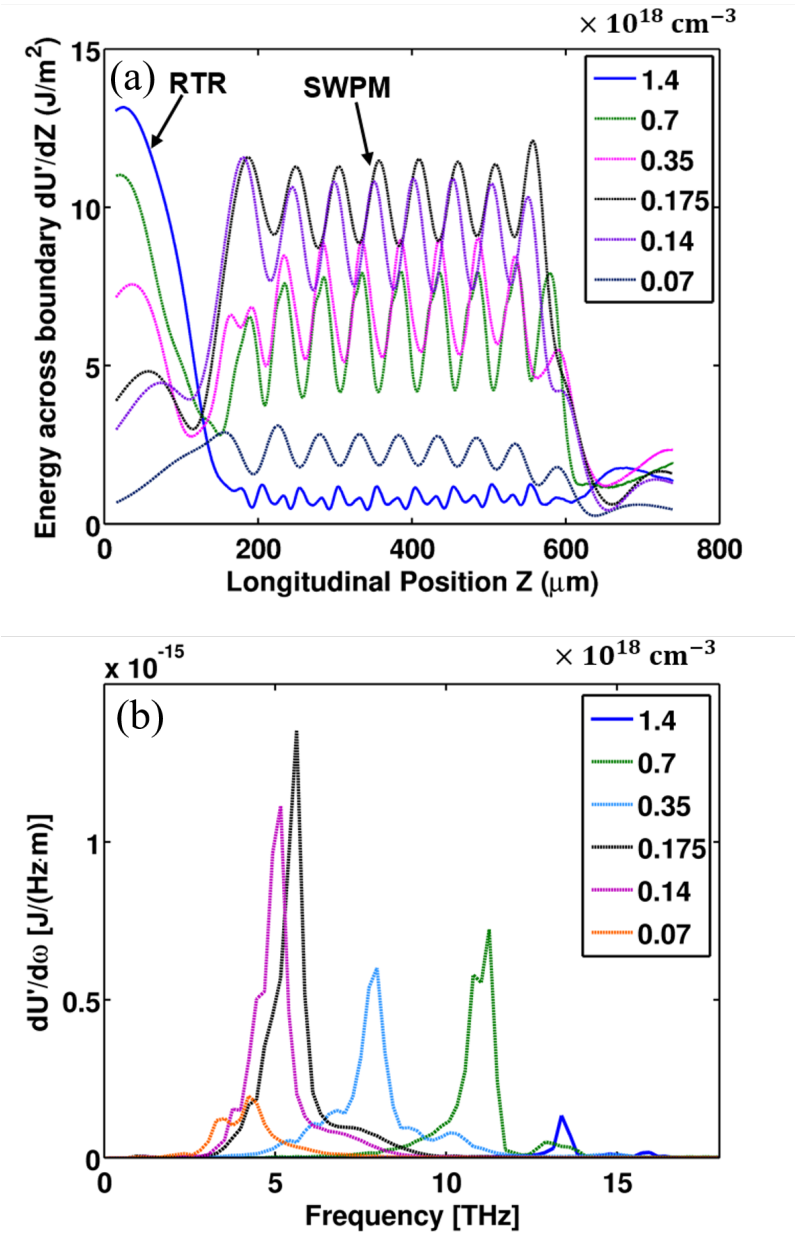

Figure 3.7: (a) THz radiation for different plasma densities. Simulation results include the broad band THz generated by resonant transition radiation (RTR) at the side end of plasma channel and the narrow band THz generated by the slow wave phase matching (SWPM) process as we discussed in this paper. For the latter case, when density is reduced until the optimal density $1.75 \times 10^{17}\ cm^{-3}$, more THz radiation leaks out the channel. (b) Radiated spectral density $dU'/d\omega$ of THz shows that as plasma density decreases, the frequency of excited THz decreases while at the same time, more THz radiation is generated until the optimal density $1.75 \times 10^{17}\ cm^{-3}$ is reached.

estimate. This enhancement phenomenon is accompanied by a change in the spectrum as illustrated by the comparisons in Fig. 3.8. We find that in this case higher order channel modes are excited by nonlinear currents and interference between higher order modes is also observed. According to the simulation results, one can conclude that all excited channel modes are enhanced simultaneously by increasing laser intensities. However, the enhancement rate for higher order modes is more rapid than lower order modes, resulting the evident higher order modes excitation as shown in Fig. 3.8(c).

Our goal is to optimize the efficiency of the optical laser pulse energy converted to THz. Channel lengths in our simulations are limited by computation time, so we are not able to simulate every channel long enough to substantially deplete the laser pulse. We define an alternate efficiency that is the fraction the depleted laser energy transferred to THz, $\eta = E_{THz}/|\Delta E_{Laser}|$. By maximizing this efficiency, less power is expended driving the plasma oscillations, thus freeing it to drive THz over longer distances. We note that this efficiency does not depend on the laser intensity for $a_0 < 1$ based on the linear theory that both E_{THz} and ΔE_{Laser} scale as a_0^2. However, for large a_0, higher order THz modes are excited by nonlinear currents, which enhances the efficiency scaling. We've achieved an energy conversion efficiency of approximate 3% for the THz generation as displayed in Fig. 3.9 and this could be further optimized by varying the corrugated plasma density profiles. For example, the conversion efficiency for the weakly relativistic case can be efficiently enhanced by finding an optimum plasma density as discussed in Fig. 3.7(a). As laser propagates through the channel, the vector potential increases, which also

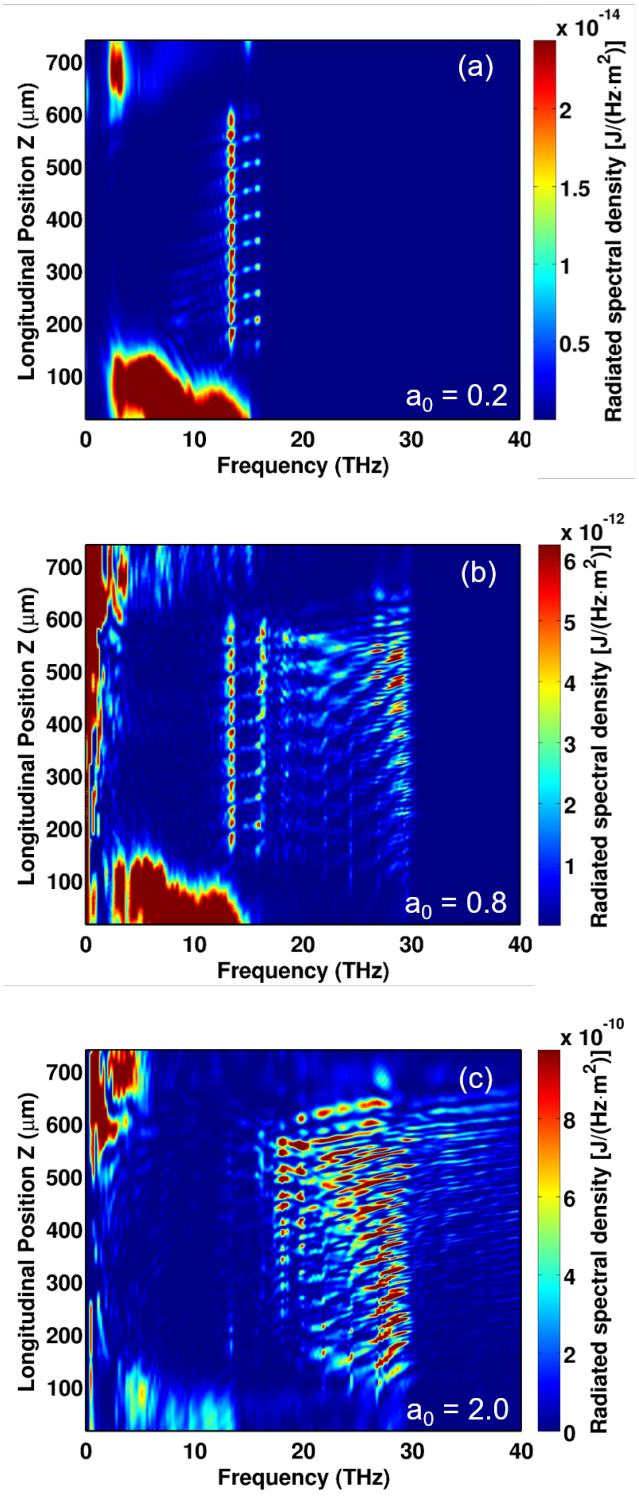

Figure 3.8: Radiated THz spectrum across the lateral diagnostic boundary for different laser intensities (a) $a_0 = 0.2$ (pulse energy 16.7 mJ) (b) $a_0 = 0.8$ (pulse energy 0.267 J) (c) $a_0 = 2.0$ (pulse energy 1.66 J). All other parameters remain the same in the simulation. As laser intensity increases, more THz energy is generated. In addition, high order channel modes are excited as well.

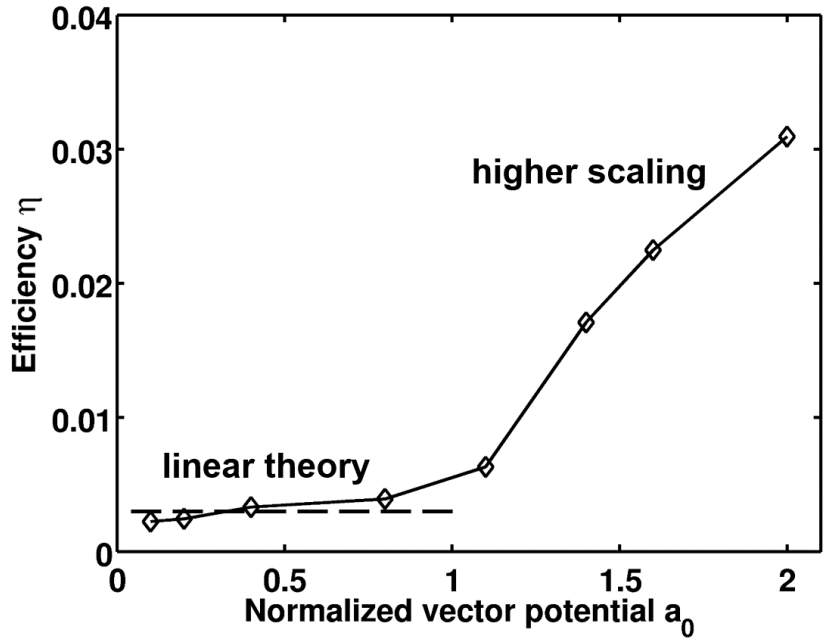

Figure 3.9: Efficiency $\eta = E_{THz}/\left|\Delta E_{laser}\right|$ for different laser intensities. Same channel parameters as shown in Fig. 3.4(a) are used. For $a_0 < 1$, η is independent of a_0 as expected. However, for $a_0 > 1$, scaling is enhanced since higher order channel modes are excited due to nonlinear currents.

contributes to the enhancement of conversion efficiency. Such phenomena will be discussed in detail in Sec. 3.3.2.5.

3.3.2.4 Dependence on Laser Pulse Duration

Since the frequencies of the channel modes are determined by the plasma profiles, the pulse duration does not affect the THz mode frequency but does determine the amplitude of the driving current at each frequency. Suppose the laser pulse has a Gaussian temporal profile $\exp[-(t-z/c)^2/\tau_p^2]$ with $2\sqrt{ln(2)}\tau_p$ as the pulse duration (FWHM), the amplitude of the ponderomotive driver at a mode frequency ω is

given by $\tau_p \exp(-\omega^2\tau_p^2/4)$, which has a peak value when $\omega\tau_p = \sqrt{2}$. Therefore, the value of τ_p can be adjusted to excite a specific range of channel mode frequencies. For the fundamental mode of 13.18 THz, the value is $\tau_p = 16.9$ fs corresponding to a FWHM pulse duration of 28.4 fs. The simulation results further verify our estimation. Shown in Figs. 3.10(a)-3.10(c) are the radiated THz spectra crossing the lateral diagnostic boundary for pulse durations of 100 fs, 30 fs, and 15 fs, respectively. The normalized vector potential $a_0 = 0.4$ remains the same for all 4 cases. For the case of a 100 fs laser pulse as shown in Fig. 3.10(a), the amplitude of the ponderomotive driver for any channel mode is small, therefore minimal THz generation is observed. For the fundamental mode (13.18 THz) of the same plasma channel, the desired pulse duration is 30 fs and the simulation result in Fig. 3.10(b) shows that the most amount of THz radiation at this frequency is generated. In addition, higher order radiation is observed as the pulse duration is shortened to 15 fs shown in Fig. 3.10(c), where there is an enhancement of the channel mode near 20 THz. Figure 3.11 displays a comparison of the radiated spectral density $dU'/d\omega$ for these pulse durations, showing the dependence on pulse duration.

3.3.2.5 Scaling with Channel Length

As the laser pulse propagates through the plasma channel, the pulse energy will be depleted and converted into both electromagnetic radiation and plasma waves [33, 40, 68–70]. Spectral red shift [71, 72] of the driver pulse is also observed in simulations. For example, the energy of a laser pulse with $a_0 = 2.0$ and pulse

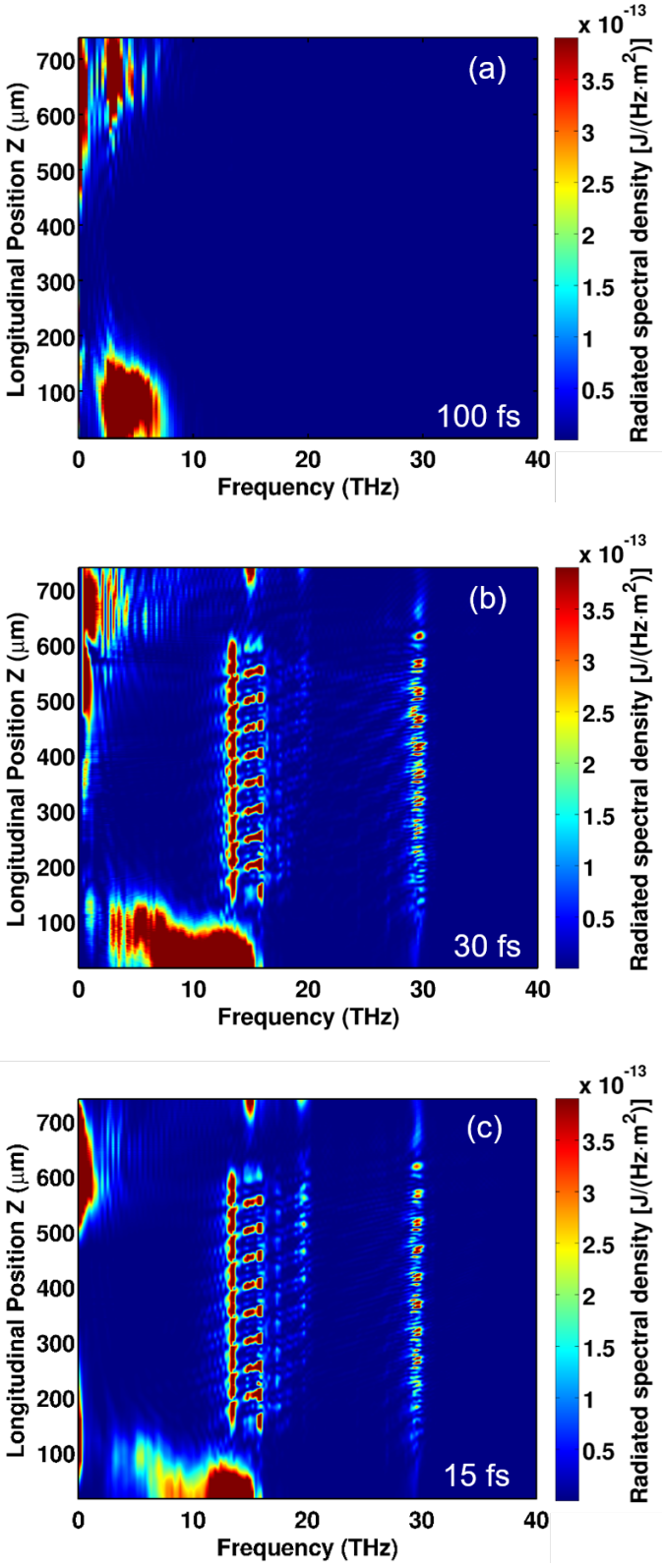

Figure 3.10: Radiated THz spectrum across the lateral diagnostic boundary for different laser pulse durations (a) 100 fs (b) 30 fs (c) 15 fs.

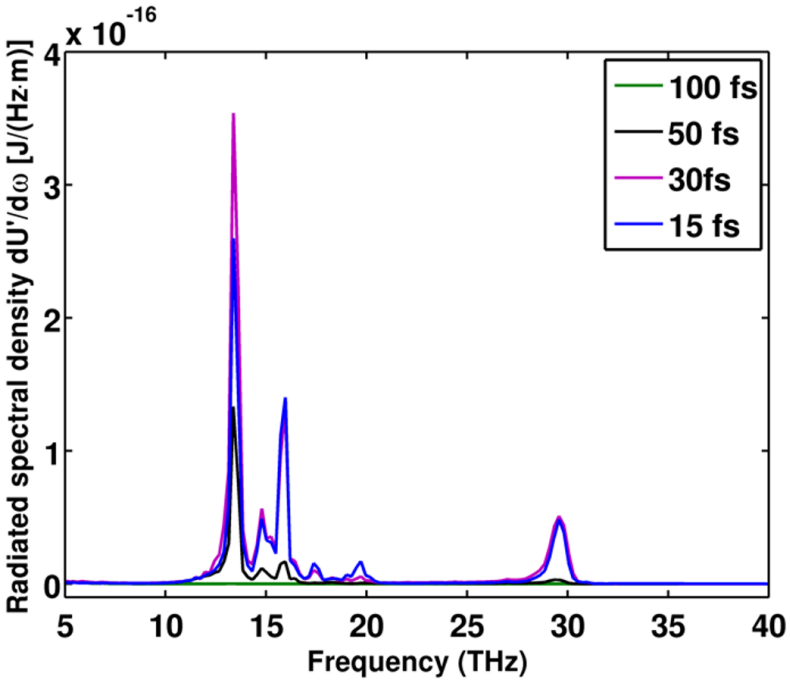

Figure 3.11: Displayed is the comparison of radiated spectral density for these pulse durations as shown in Fig. 3.10.

duration of 15 fs propagating through the 10 period channel shown in Fig. 3.4(a), will depleted by 1.12%. At the same time the central frequency shifts from 375 THz to 371 THz. Consistent with action conservation, as the pulse depletes, the normalized vector potential a_0 associated with the laser pulse increases and the laser pulse changes shape. This accounts for the results shown especially in Fig. 3.8(c) where evident enhancement of THz is generated at the tail of the channel. In order to maximize generation of THz radiation, the pulse energy must be efficiently depleted within the length of the channel. The depletion length L_{dp} for a pulse with duration matched to the plasma period is given [69] by $L_{dp} = 17.4 k_l^2 k_p^{-3} a_0^{-2}$ in the weakly relativistic regime ($a_0 << 1$) and $L_{dp} = 8.7 k_l^2 k_p^{-3}$ in the relativistic regime ($a_0 >> 1$), where k_l is the central wavenumber of the laser pulse and $k_p = \omega_{p0}/c$. These formulas give, for laser pulses of normalized vector potential $a_0 = 0.4$ and $a_0 = 2.0$, depletion length of 53 cm and 4.25 cm, respectively. The averaged on axis density of the channel is $1.4 \times 10^{18}\ cm^{-3}$.

The pulse evolution in the laser frame in 2D planar geometry can be estimated by the following calculation. Assume the laser vector potential has the following term,

$$A = \hat{A}\left(\boldsymbol{x}_\perp, \xi, t\right) \exp\left(-ik_0\xi\right) + c.c.\ , \tag{3.10}$$

where $\hat{A}$ is the slowly varying envelope and $\xi = ct - z$. The wave equation is then described by,

$$\left[-\frac{\partial^2}{c^2\partial t^2}+\frac{2}{c}\frac{\partial}{\partial t}\left(ik_0-\frac{\partial}{\partial\xi}\right)+\nabla_\perp^2\right]\hat{A}=\frac{\omega_p^2(\xi,t)}{c^2}\hat{A}\,. \tag{3.11}$$

One can define a time the wave action as

$$I=Re\left\{\int\frac{d^2x_\perp d\xi}{2\pi c}\hat{A}^*\left[k_0+i\frac{\partial}{\partial\xi}+i\frac{\partial}{c\partial t}\right]\hat{A}\right\}\,. \tag{3.12}$$

The $\partial/\partial t$ term can be neglected since k_x^2, $\omega_p^2 << k_z^2$ [72]. The wave action defined in Eq. (3.12) is the conserved during the pulse propagation. On the other hand, the energy stored in the laser pulse is given by,

$$U_L=\int\frac{d^2x_\perp d\xi}{2\pi}\left|\left(k_0+i\frac{\partial}{\partial\xi}\right)\hat{A}\left(\boldsymbol{x}_\perp,\xi,t\right)\right|^2 \tag{3.13a}$$

$$=\int\frac{d^2x_\perp d\xi}{2\pi}\left|\frac{\partial}{\partial\xi}A\left(\boldsymbol{x}_\perp,\xi,t\right)\right|^2\,. \tag{3.13b}$$

Since the electromagnetic fields associated with the pulse are (E_x, B_y, E_z) and according to Maxwell's Equations the vector potential can be estimated $B_y = -\partial A_x/\partial z = \partial A_x/\partial\xi$. Applying a Fourier transform to the above Eqns. (3.12) and (3.13a) and using Parseval's Theorem, one can obtain the following expressions of wave action and pulse energy in frequency domain,

$$I=Re\left\{\int\frac{d^2x_\perp}{2\pi c}\int\frac{dk}{2\pi}\frac{1}{k}\left|\overline{B}\left(\boldsymbol{x}_\perp,k,t\right)\right|^2\right\}\,. \tag{3.14}$$

$$U_L = \int \frac{d^2 x_\perp}{2\pi} \int \frac{dk}{2\pi} \left| \overline{B}_y \left(\boldsymbol{x}_\perp, k, t \right) \right|^2 \ . \tag{3.15}$$

To study this, we simulate an 800 nm laser pulse of duration 15 fs, transverse spot size of 15 μm and $a_0 = 2.0$ (pulse energy 0.55 J). The channel parameters remain the same as in Fig. 3.4(a), except the channel length is extended to 1.5 cm. The simulation is conducted with a moving window of length 750 μm to collect all the possible THz emission after incidence of the pulse. Simulation domain has a size of $102.4 k_n^{-1} \times 374.8 k_n^{-1}$ with 1024×20480 cells in the x and z directions, respectively, where $k_n^{-1} = 2.01115$ μm is the normalization used in the simulation. The energy stored in the laser pulse is displayed in Fig. 3.12(a) as a function of distance. Within the propagation distance of 1.5 cm, 80% of the pulse energy is depleted. Fig. 3.12(b) displays the radiated THz energy versus propagation distance. The rate (dU'/dz) of THz energy generation increases with distance as the normalized vector potential a_0 increases during propagation due to the action conservation [40, 68, 71, 72]. As a result, after the propagation of 1.5 cm, more than 8% of the total pulse energy is converted into THz radiation.

We also investigate the laser pulse evolution during the propagation. For example, the pulse properties, i.e., spatial shape and frequency, are displayed in Fig. 3.13 at three different locations (initial, 4.5 mm, 7 mm) as shown in Fig. 3.16(a). The temporal profiles of on axis magnetic field B_y at these different locations displayed in Fig. 3.13 indicate that the front of the laser pulse is preferentially eroded during the interaction with the plasma channel. Since the laser pulse is well guided by

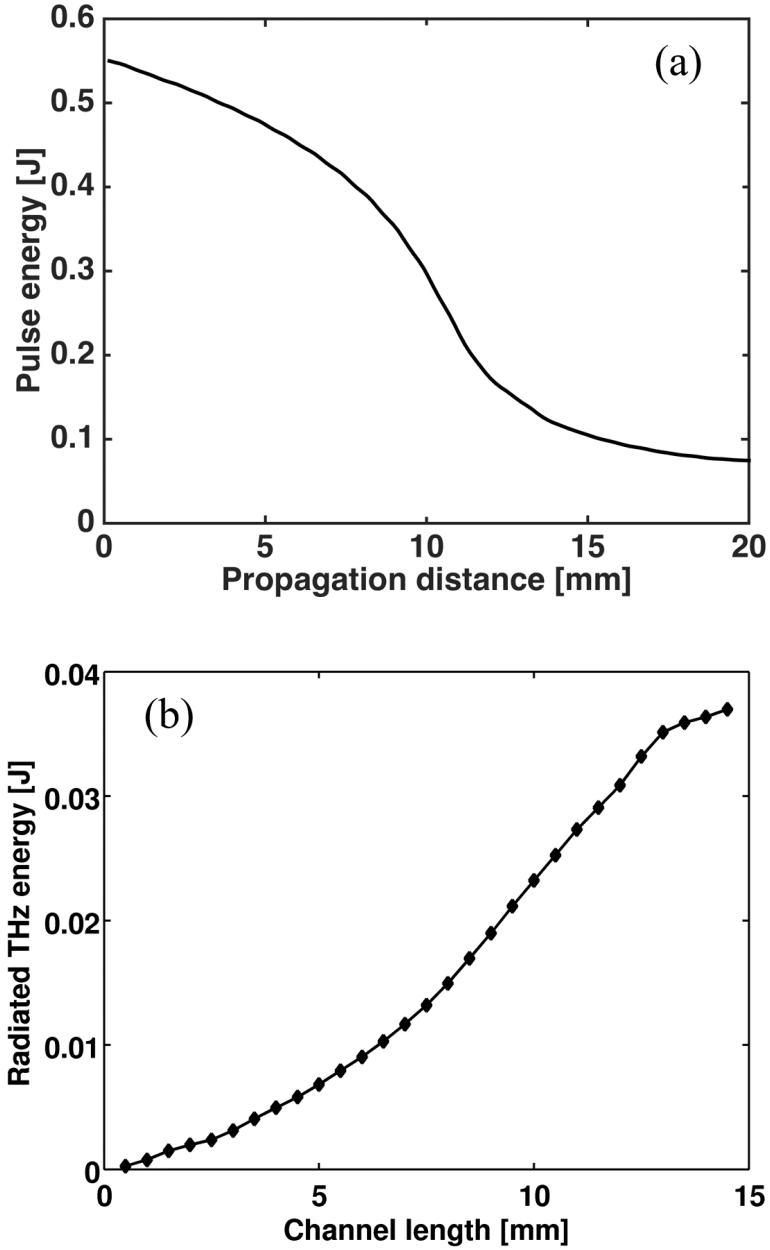

Figure 3.12: (a) Pulse energy depletion of an initial laser with $a_0 = 2.0$ (0.55 J) during the propagation in a corrugated plasma channel. Simulation result shows that around 80% of the energy stored in the laser pulse is depleted within the propagation distance of 1.5 cm.(b) Scaling of Radiated THz energy versus plasma channel length.

the channel structure, the transverse profiles still retain a Gaussian shape after the propagation. However, one can notice from the simulation that the on axis peak field B_y increases during the interaction. On the other hand, as shown in Fig. 3.14(b), a red shift is observed during the propagation. Therefore, the normalized vector potential, as defined by $a = eE_0/m_e c\omega_0$, increases during the propagation in the plasma channel as long as the wave action is conserved. One may expect that the more THz radiation is generated per distance toward the end. The wave action during the propagation in the same corrugated plasma channel is also displayed in Fig. 3.15. The wave action can be considered as conserved within the propagation distance of 1 cm. However, beyond that distance, the laser pulse is strongly modified and depleted after 1 cm; the action then drops quickly.

To illustrate the scaling shown in Fig. 3.12(b) in detail, we calculated the radiated THz energy dU'/dZ at three different locations with the same channel length as displayed in Fig. 3.16(b). As a result of the increase of a_0 and spectral modification of the driver pulse, more THz is generated during the propagation despite of the same channel length. Furthermore, the radiated spectral density shown in Fig. 3.16(c) shows that broader spectrum of THz is expected at a forward/later channel location.

For comparison, THz generation using a relatively low intensity laser pulse with pulse duration of 30 fs, transverse spot size of 15 μm and $a_0 = 0.4$ (pulse energy 44.5 mJ) is also simulated. In this case, we found the optimum plasma density for short propagation distance (10 periods) is $1.4 \times 10^{17}\ cm^{-3}$ as shown in Sec. 3.3.2.2. The lower plasma density and laser intensity lead to a much longer

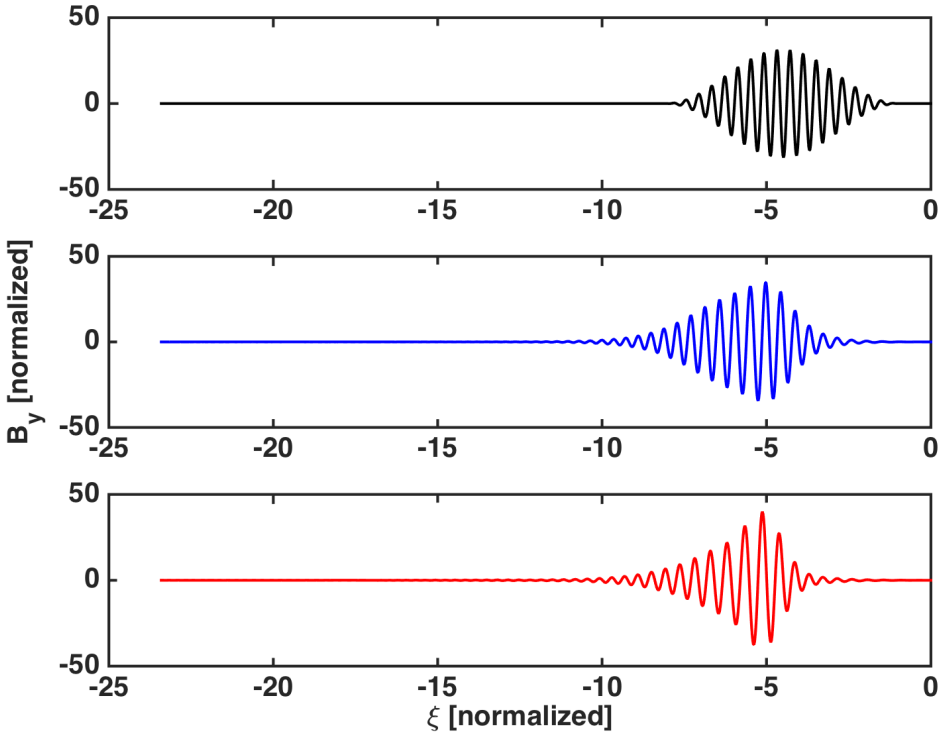

Figure 3.13: Temporal profiles of on axis magnetic field B_y of the pump laser at the three different locations (initial, 4.5 mm, 7 mm) of the channel as displayed in Fig. 3.16(a) indicate that the front of the laser pulse is preferentially eroded during the interaction with the plasma channel.

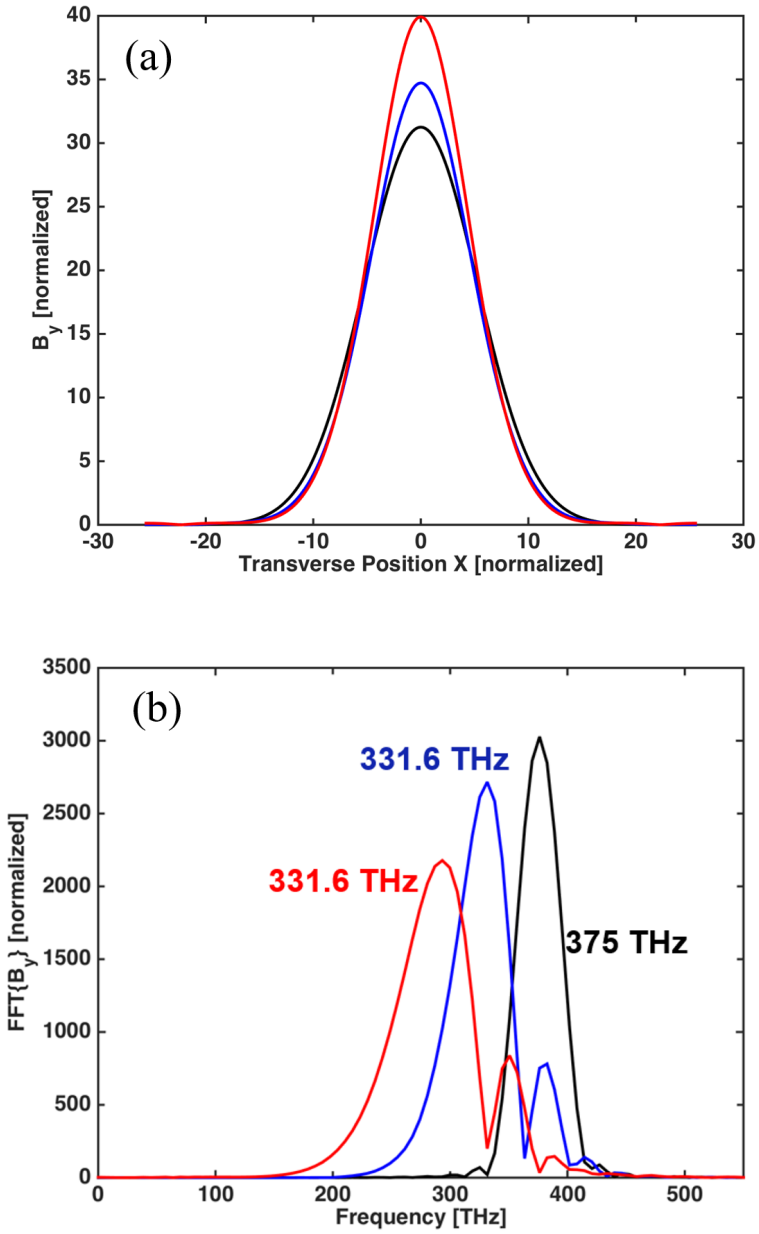

Figure 3.14: (a) Transverse profiles of the magnetic field B_y of the pump laser at the three different locations (initial, 4.5 mm, 7 mm) remain a good Gaussian shape since the pulse is well guided by the channel structure. However, the peak filed on axis increases. (b) Fourier transform of the magnetic field B_y of the pump laser shows spectral modification of the pulse, the central frequency shifts from the initial 375 THz to 331.6 THz within a propagation distance of 7 mm.

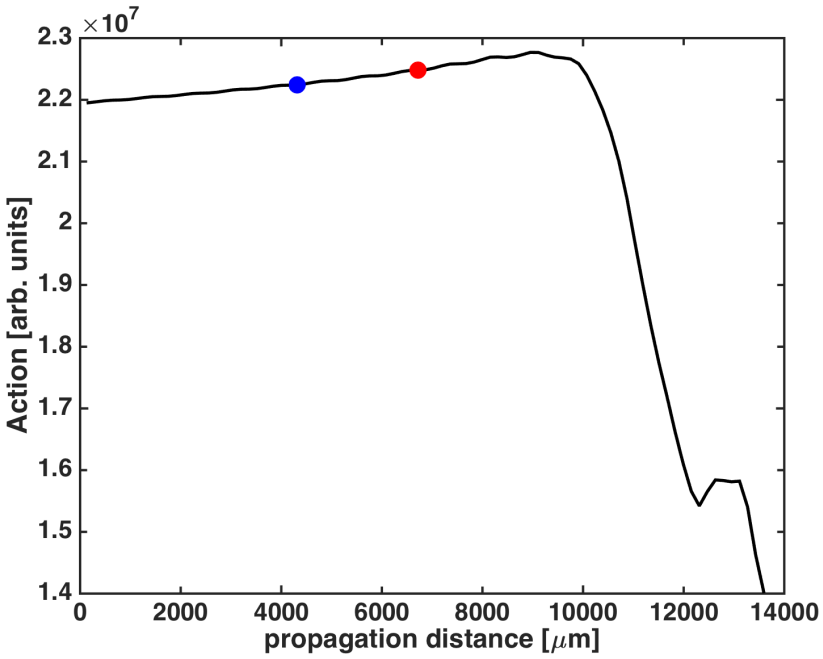

Figure 3.15: Wave action defined in Eq. (3.12) as a 800nm laser pulse with pulse duration of 15 fs, transverse spot size of 15 μm and $a_0 = 2.0$ propagates through the same corrugated plasma channel in Fig. 3.2a.

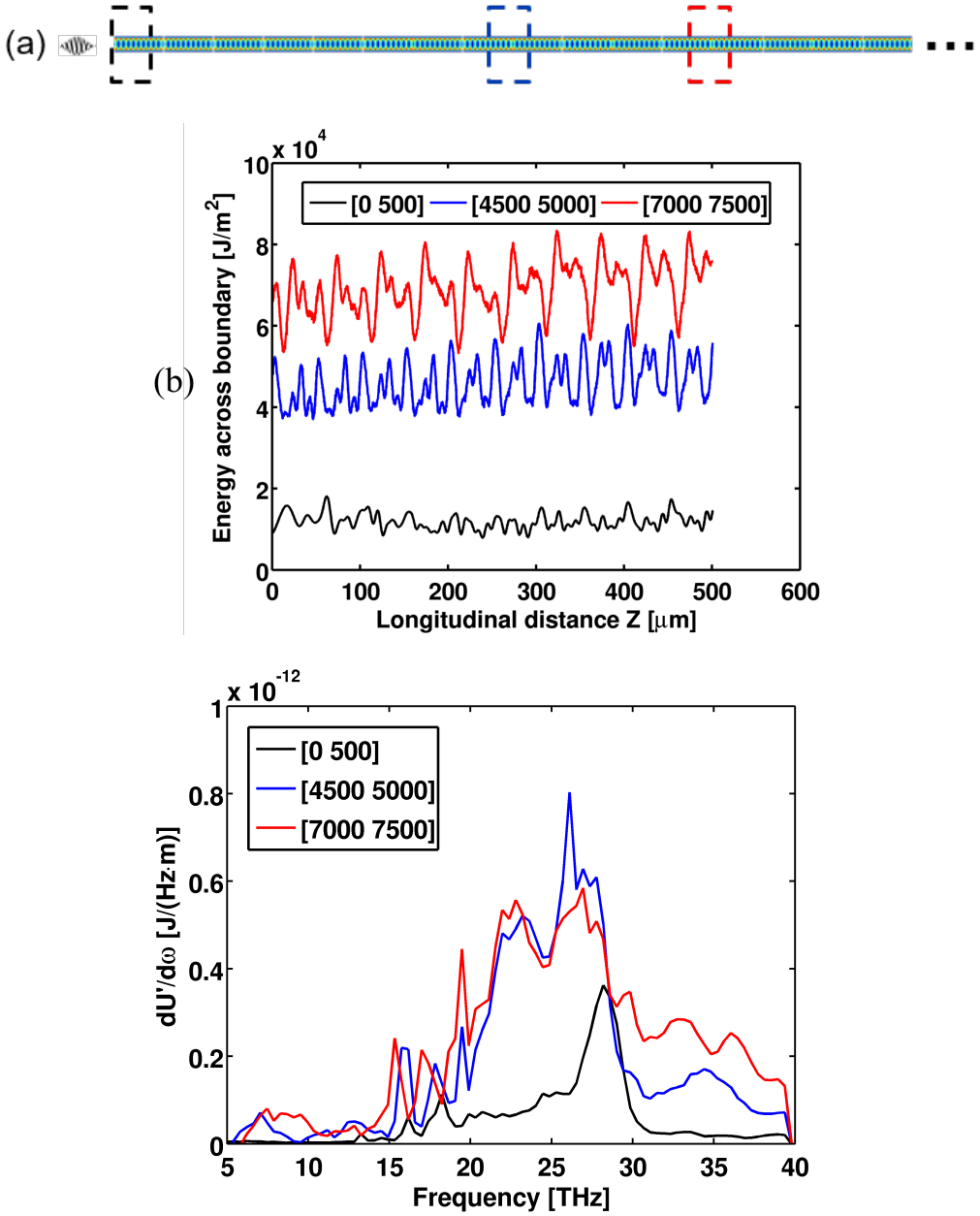

Figure 3.16: (a) Investigate THz generation during the pulse propagation in a corrugated plasma channel at three different locations, 0-500 μm (black), 4500-5000 μm (blue), and 7000-7500 μm (red), respectively. (b) Radiated THz energy dU'/dZ at these three different locations. The x axes are shifted to 0-500 μm so that the three simulation results can be aligned. The increase of a_0 explains why more THz is generated during the propagation despite of the same channel length. (c) Radiated spectral density dU'/dω for the corresponding three locations shows that the THz spectrum becomes broader during the propagation.

pulse depletion length than for that of the previous case displayed in Fig. 3.12(b). Consequently, due to computational restrictions, we were not able to simulate a channel long enough to substantially deplete the pulse energy. Instead, we simulate pulse propagates through a corrugated plasma channel for a distance of 1.5 cm. The simulation result displayed in Fig. 3.17(a) indicates that only 10% of the energy stored in the laser pulse is depleted within the same distance. The different steps are oscillations in beam radius due to the mismatch between the transverse pulse width and the guiding structure. Shown in Fig. 3.17(b) is the radiated THz energy versus plasma channel length. About 50 μJ of THz energy is generated within a 1.5 cm interaction distance. As a result, it can be concluded that the conversion efficiency for $a_0 = 0.4$ is much lower than that of a higher intensity pulse. In addition, a much longer plasma channel is needed to deplete the pulse energy for $a_0 = 0.4$.

3.3.2.6 Other parameters

It has been discussed [34] that the mode width w_{ch}, channel characteristic radius r_c and r_0, density modulation amplitude and modulation period will all affect the spectrum and excitation of THz modes. In this section, we consider another corrugated plasma channel as shown in Fig. 3.2b. This channel has a maximum local density in the center, which in contrast, the channel we considered in previous sections has the maximum local density at the lateral edges. The channel has the same 10 periods with modulation wavelength of 50 μm, other channel parameters are $\delta = 0.7$, $\overline{n}_1 = 1.3$, $\delta_1 = 0.1$. In order to match the density profile shown in Fig. 3.1b,

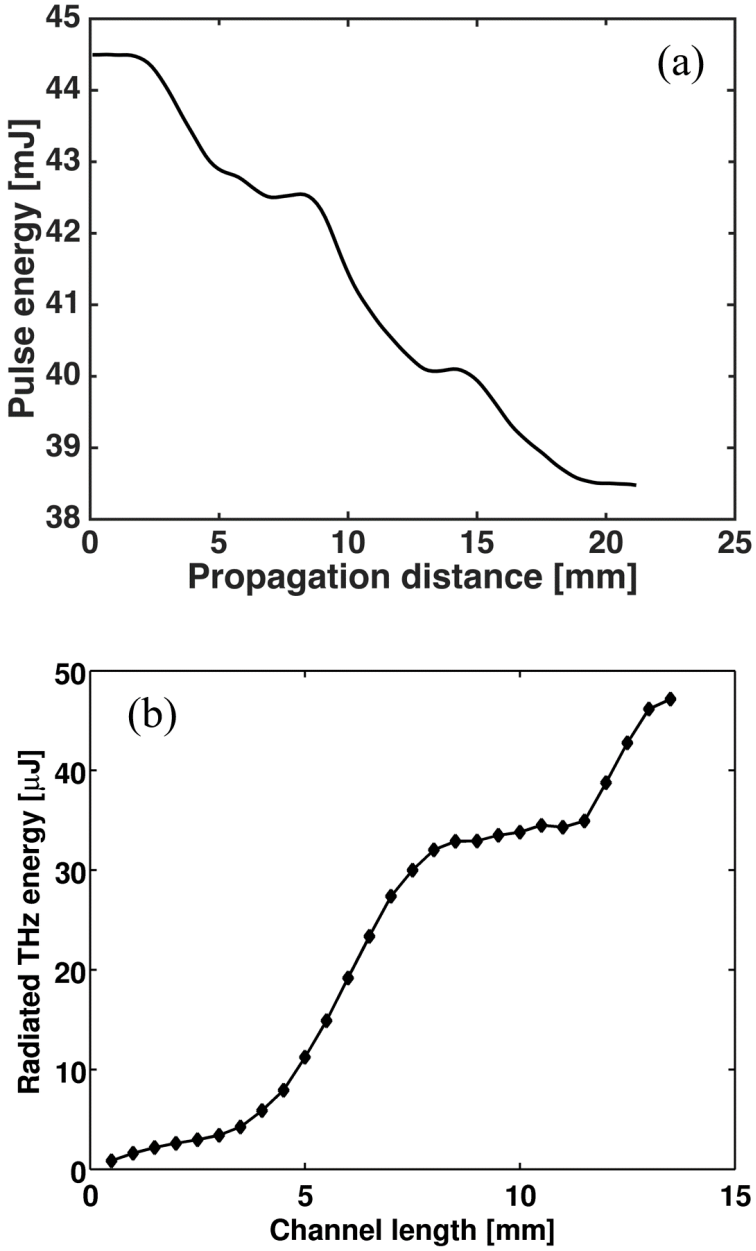

Figure 3.17: (a) Pulse energy depletion of an initial laser with $a_0 = 0.4$ (44.5 mJ) during the propagation in a corrugated plasma channel. Simulation result shows that only 10% of the energy stored in the laser pulse is depleted within the propagation distance of 1.5 cm. (b) Scaling of Radiated THz energy versus plasma channel length indicates that only 1.1% of the depleted laser energy is concerted into THz radiation in this case.

both cut-off radius and channel radius are also modulated as $r_c[\mu m] = 22.5 - 7.5\cos(k_m z)$ and $r_0[\mu m] = r_c + 15$. Simulation results of two different laser pulses propagating through the same channel are presented in Fig. 3.18(a) and 3.18(b), with normalized vector potential $a_0 = 0.4$ and $a_0 = 2.0$, respectively. Both laser pulses have the same transverse spot size of 15 μm and pulse duration (FWHM) of 50 fs with a central wavenumber of 800 nm. Figure 3.18(a) shows narrow band THz radiation is excited around the fundamental frequency of 13.6 THz. The amount of generated THz energy as well as the calculated THz conversion efficiency for this channel displayed in Table 3.2 is significantly higher than the case shown in Fig. 3.5 using the same laser pulse. This could be explained by the excitation of a higher electron current since the driver pulse encounters more electrons due to the local density maximum on axis for the density profile shown in Fig. 3.2b. In addition, the axially averaged density profile has a lower radial barrier that allows the generated THz waves to escape the channel. For a higher intensity laser pulse with $a_0 = 2.0$, the generated THz shown in Fig. 3.18(b) is characterized by a different spectrum compared with Fig. 3.8(c). Although the amount of THz energy is enhanced for both cases, the spectrum is still confined in a relatively narrow band fundamental frequency while in the case of Fig. 3.8(c), higher order THz modes are significantly generated and consequently modify the spectrum.

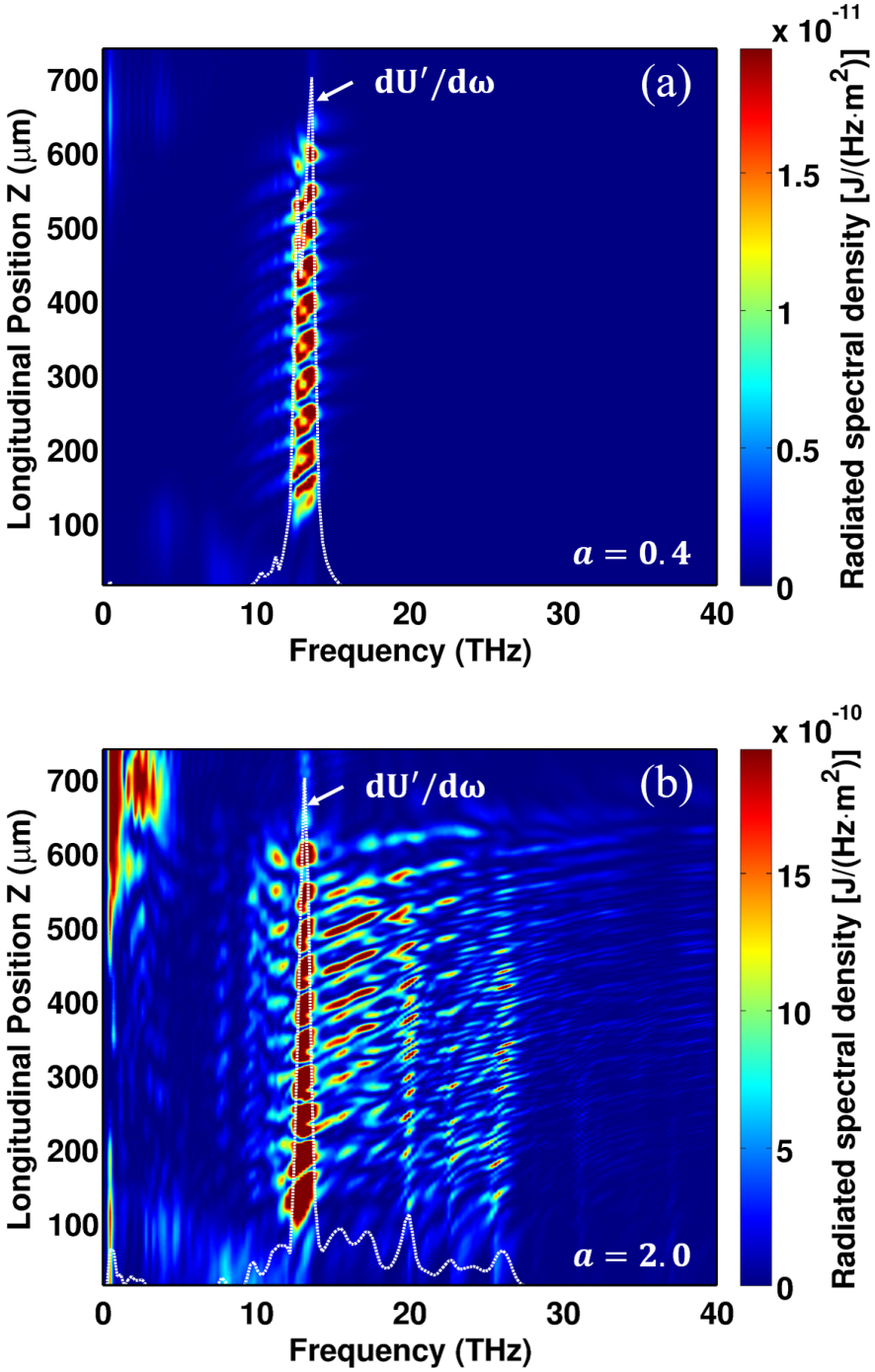

Figure 3.18: False color image of radiated THz spectrum across the lateral diagnostic boundary for two different laser pulses (a) $a_0 = 0.4$ (b) $a_0 = 2.0$. The integral over all boundary locations yields to the total THz spectrum dU'/dz and is also included in the plot (white, dashed). The plasma density profile used in the simulations is shown in Fig. 3.2b and has a local maximum in the center of the channel. Simulation result shows that an ideal narrow band THz spectrum is excited and higher THz energy is preferentially generated in this type of channel.

3.4 Conclusions and Discussions

We have investigated a mechanism by which an intense, ultrashort laser pulse can ponderomotively drive THz radiation in an underdense corrugated plasma waveguide. These slow wave periodic structures have been generated experimentally and can support electromagnetic modes that can couple with the currents ponderomotively driven by the laser pulse. This provides the possibility of generating significant THz radiation. We presented a mathematical model for the corrugated plasma waveguides, from which the dispersion relation of the channel modes is derived, enabling prediction of the generated THz frequencies. Theoretical analysis and Full format PIC simulations are conducted to study the THz generation in corrugated plasma waveguides. Our study is the first to study the nonlinear regime including generation of nonlinear plasma wakes and self-consistent evolution of the driving laser pulse. A range of laser pulse parameters and plasma channel structures are considered with the goal of maximizing the conversion efficiency of optical pulse energy to THz.

Table 3.2 displays the simulation results for different driver pulse parameters and plasma densities for two types of corrugated channels displayed in Fig. 3.2. Most of the simulations were conducted using a 10 period channel (0.5 mm in length) to investigate the conversion efficiency of the depleted optical pulse energy to generated THz. For these simulations, the pulse energy only depletes a small percentage within 0.5 mm. Only few longer runs with substantial pulse energy depletion were conducted. Simulating long propagation distances of 1.5 cm is included in Table 3.2.

More THz energy is generated using the channel type shown in Fig. 3.2b. A laser pulse with higher intensity, i.e., larger a_0 and shorter pulse duration, also contributes to more THz generation. It is found an optimum lower plasma density enables more THz radiation to escape the channel, however, since the excited THz modes depends on the channel structures according to the dispersion relation discussed in Sec. 3.2.3, lower plasma density also modifies the generated THz spectrum. In addition, to efficiently deplete the pulse energy into the plasma within a shorter channel, a higher plasma electron density is preferred. Therefore, we choose a laser pulse with $a_0 = 2.0$ and pulse duration of 30 fs. The same channel shown in Fig. 3.2b is used with an averaged on axis electron density of $1.4 \times 10^{18}\ cm^{-3}$ except the channel length is extended to 1.5 cm. The simulation result as displayed in Table 3.2 shows after the laser pulse propagates through the channel for 1.5 cm, around 48% of the pulse energy is depleted. At the same time, 16 mJ of THz energy with a narrow spectrum is generated. The conversion efficiency is around 3% and less than the case shown in Sec. 3.3.2.5. The is probably due to the fact that the channel displayed in Fig. 3.2b no longer remains a transverse parabolic structure for optical guiding. In fact, laser energy leaks laterally and the wave action is not conserved as the laser pulse propagates through the channel. Therefore, the normalized vector potential a_0 decreases with the propagation distance and less THz energy is generated.

In order for the present mechanism to be a useful high power source of THz radiation, the spectrum should have flexible tunability. Since the excited THz is the channel modes of the corrugated plasma structure, all the parameters used in Eq. (3.2) can be tuned to modify the THz spectrum, more specifically, tuning the

Table 3.2: Comparison of generated THz energy for different laser intensities and density profiles.

Channel Type	a_0	pulse duration [fs]	on-axis density [$\times 10^{18}$ cm^{-3}]	channel length [mm]	energy depletion into the channel	THz energy [mJ]	efficiency η
Fig. 3.2b	0.4	30	1.4	0.5	0.033%	0.0016	12.03%
	0.4	50	1.4	0.5	0.024%	0.0013	8.17%
	0.4	50	0.14	0.5	0.006%	4.68e-4	11.7%
	2.0	30	1.4	15	48%	16	3%
	2.0	50	1.4	0.5	0.4%	0.6493	9.84%
Fig. 3.2a	0.4	30	0.14	15	10.11%	0.048	1.11%
	0.4	50	1.4	0.5	0.0175%	3.36e-5	0.28%
	2.0	15	1.4	15	81.8%	38	8.44%
	2.0	50	1.4	0.5	0.39%	0.2	3.25%

averaged on axis density n_{00} is the easiest way in the experiment. For example, a lower density $n_{00} = 1.75 \times 10^{18}\ cm^{-3}$ can enhance the THz generation as well as decreasing the THz frequency for the case of a driving pulse with $a_0 = 0.4$. At lower laser intensities, for example $a_0 = 0.4$, only lower frequency of the channel modes is efficiently excited and thus a narrow band spectrum (0.4 THz in FWHM band width) is generated. However, at higher laser intensities ($a_0 = 2.0$), higher order channel modes are excited by nonlinear currents and strongly modify the THz spectrum. Laser pulse duration also contributes to the enhancement of a specific THz frequency by the maximizing the amplitude of the ponderomotive driver. Since the generated THz waves emit laterally, one can use an axicon mirror to focus the THz radiation to one direction for practical uses. Overall, the present mechanism using realistic corrugated plasma structures in this paper provides a potential higher power source of THz with tunable spectrum and a very high conversion over 8% efficiency is achieved.

3.5 Appendix A: CALCULATING THE RADIAL EIGENMODES

To calculate the radial eigenmodes numerically for a arbitrarily given transverse density profile, one can numerically evaluate E_r by Eq. (3.7) using shooting method given a set of parameter $k_\perp$ and determine what $k_\perp$ satisfies the on axis boundary condition $E_r(0) = 0$. For mathematical simplicity we set $\Phi = rE_r$, $\beta(r) = k_p^2(r)$ and Eq. (3.7) yields to,

$$\frac{\partial^2 \Phi}{\partial r^2} - \frac{1}{r}\frac{\partial \Phi}{\partial r} + \left(k_c^2 - \beta(r)\right)\Phi = 0 \; . \tag{3.16}$$

One can also find as $r \to 0$, $\Phi \sim a \cdot r^2 + b$, therefore the on axis boundary condition is satisfied if $b \to 0$. The finite difference (FD) shooting method can be implemented by,

$$\Phi_{j-1} = -\frac{\Phi_{j+1}(2j-1) + 2j\left[h^2(k_c^2 - \beta_j) - 2\right]\Phi_j}{1+2j} \; , \tag{3.17}$$

where h is the step size.

To find out the number of different radial modes, i.e., k_c, can be supported by the channel with finite transverse size, one can scan the parameter k_c in Eq. (3.17) and apply the Nyquist Theory illustrated in Fig. 3.19. $F(s)$ is an analytic function in a closed region of complex plane s given as left. As s travels on the path on the s plane in the clockwise direction, $F(s)$ encircles the origin on the complex plane N times,

$$N = Z - P \; , \tag{3.18}$$

where Z and P denote the number of zeros and poles of function $F(s)$ in the closed region, respectively. For our shooting method, as shown in Eq. (3.17), $\Phi(0)$ has no poles and the result yields to $N = Z$.

Fig. 3.20 shows that for a given density profile, $\Phi(0)$ encircles origin twice as k_c

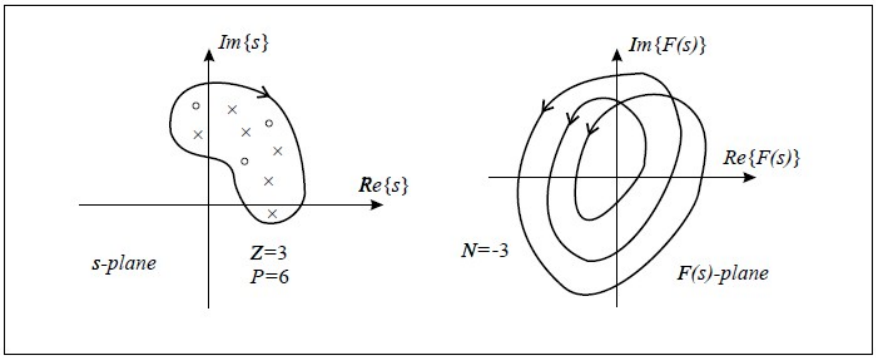

Figure 3.19: Nyquist Theory: Cauchy's principle.

scans from 0.301 μm^{-1} to 0.402 μm^{-1}, which implies that the channel can support two radial eigenmodes according to Cauchy's principle. Further one can apply linear interpolation to narrow the range of k_c for each mode and find the exact value of k_c in which the field satisfies the boundary condition. Fig. 3.21(a) and 3.21(b) are two figures indicating the range of k_c during the interpolation to find the exact value k_c for first and second radial eigenmodes, respectively.

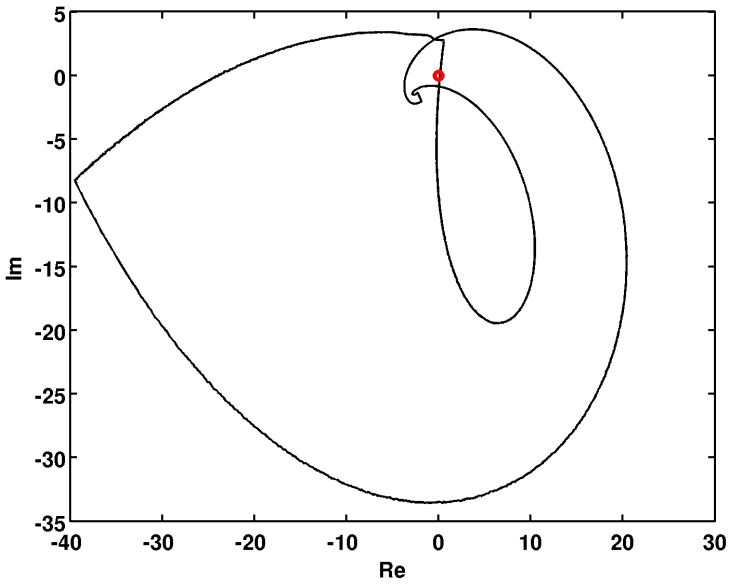

Figure 3.20: $\Phi(0)$ encircles origin (red dot) twice as k_c scans from 0.301 μm to 0.402 μm. The density profile in this case is: $n_{00} = 1.4\times10^{18}\ cm^{-3}$, $\delta_1 = \delta = 0.9$, $\overline{n}_1 = 3$, $r_c = 30\ \mu m$ and $r_0 = 40\ \mu m$.

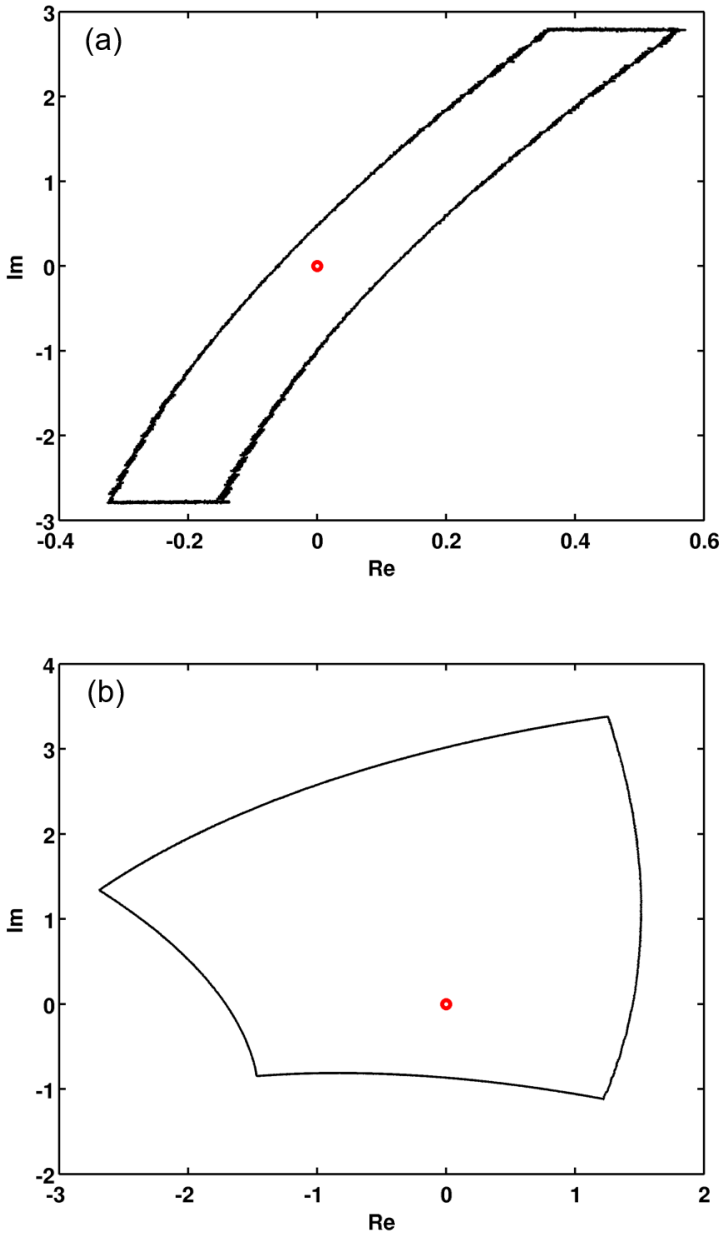

Figure 3.21: (a) k_c of the fundamental radial mode is found to between 0.301 μm^{-1} and 0.303 μm^{-1}. (b) k_c of the second order radial mode is found to between 0.36 μm^{-1} and 0.37 μm^{-1}. Applying linear interpolation can help narrow the range of k_c and we find $k_c = 0.30195$ μm^{-1} for the first radial mode and $k_c = 0.3638$ μm^{-1} for the second radial mode.

Chapter 4: Summary and Conclusions

We have investigated two different mechanisms of ponderomotively driven THz generation in inhomogeneous plasmas: (i) a resonant transition radiation (RTR) mechanism occurring as a pulse crosses a plasma boundary and (ii) a slow wave phase matching mechanism (SWPM) that occurs in corrugated plasma channels. The two mechanisms are fundamentally different in two aspects although they are both based on laser plasma interactions. THz generated by resonant transition radiation originates from the varying density at the plasma boundary while THz generated in axially modulated plasma channels is enabled by the subluminal channel modes supported by these slow wave structures, which can be phase matched to the laser ponderomotive potential. The former mechanism generates backward broad band THz with maximum frequency close to the maximum of the plasma frequency while the latter is characterized by lateral emission and a coherent, narrow band, tunable spectrum. Since most of the laser pulse energy can be depleted as the pulse propagates through the channel, the latter mechanism provides possibilities of THz generation with higher power and conversion efficiency.

In the chapter entitled Terahertz Generation via Resonant Transition Radiation (RTR) in A Plasma Density Gradient, we have both theoretically and nu-

merically investigated ponderomotively driven resonant THz transition radiation generated at plasma boundaries. Broad-band THz radiation is generated with frequencies up to the maximum plasma frequency. The parameters of the driving pulse as well as the plasma profiles affect the properties of the generated THz radiation. The spectrum and angular distribution of the THz radiation can also be tuned by varying these parameters.

Resonant transition radiation is generated at a diffuse plasma boundary and is preferentially enhanced if the laser pulse propagates through an increasing density profile. We've developed a model to describe the physical processes in this diffuse plasma case. The THz is generated primarily at the plasma resonance and must tunnel to a turning point before it leaves the plasma and propagates into vacuum. The calculated Poynting flux shows that this process enhances the amount of THz energy efficiently through a density increasing ramp and diminishes THz generation through a decreasing density ramp. A scaling law was developed to allow one to estimate the amount of THz energy generated for different density ramp lengths.

Both numerical solutions of the wave equation and PIC simulations agree with our model. The amount of THz radiation generated can be dramatically increased compared with that in the sharp vacuum plasma boundary case. As an example, a fixed driver pulse (1.66 J) excites approximately 422.9 μJ of THz radiation in a 1.2 mm increasing density ramp. Thus this mechanism provides the possibly of developing new high power tunable THz sources.

The second mechanism is studied in detail in Chapter 3, High-Power Tunable THz Generation in Corrugated Plasma Waveguides. We have investigated the

mechanism by which an intense, ultrashort laser pulse can ponderomotively drive THz radiation in an underdense corrugated plasma waveguide. These slow wave periodic plasma structures have been routinely demonstrated experimentally and can support subluminal channel modes to be further phase matched with the driver pulse, thus providing possibility of generating significant THz radiation. We proposed a complete mathematical model for the corrugated plasma waveguides and the dispersion relation of the channel modes is derived to predict the generated THz frequency. A numerical method is developed to precisely calculate the radial eigenmodes of the excited wave and how many modes can be confined by the channel. Full format PIC simulations conducted in 2D planar geometry show that evident THz radiation is generated. A range of laser pulse parameters and plasma channel structures are considered with the goal of maximizing the conversion efficiency of optical pulse energy to THz.

Two different types of axially modulated plasma channels are considered, one has the maximum density at the lateral edges and another has the maximum density at the center of the channel. Both two types of channels can be created experimentally. The channel with the maximum density at the lateral edges is more suitable for laser guiding purposes, especially for higher laser intensities (larger a_0). Therefore most of the laser pulse energy can be guided inside the channel during the propagation and more of the pulse energy can be converted into THz radiation. The channel with the maximum density at the center is better to excite the narrow fundamental THz modes and the enhancement of THz radiation is observed especially for the laser pulses with lower intensities (small a_0).

Most of the simulations are conducted using a complimentary 10 periods channel to investigate the conversion efficiency of the depleted optical pulse energy to generated THz, although the pulse energy only depletes a small percentage within 0.5 mm. We then define an alternate efficiency that is the fraction the depleted laser energy transferred to THz, $\eta = E_{THz}/|\Delta E_{Laser}|$. By maximizing this efficiency, less power is expended driving the plasma oscillations, thus freeing it to drive THz over longer distances. We note that this efficiency does not depend on the laser intensity for $a_0 < 1$ based on the linear theory that both E_{THz} and ΔE_{Laser} scale as a_0^2. More THz energy is generated using the channel type which has a maximum density at the center. A laser pulse with higher intensity, i.e., larger a_0 and shorter pulse duration, also contributes to more THz generation. It is found an optimum lower plasma density enables more THz radiation to escape the channel, however, since the excited THz modes depends on the channel structures according to the dispersion relation, lower plasma density also modifies the generated THz spectrum. In addition, to efficiently deplete the pulse energy into the plasma, a higher plasma electron density is preferred. Therefore, we choose a laser pulse with $a_0 = 2.0$ and pulse duration of 30 fs. Both two channel types are considered with an averaged on axis electron density of $1.4 \times 10^{18}\ cm^{-3}$. These simulations are computational expensive and due to the computational restrictions, we were only able to simulate a number of long propagation distance of 1.5 cm which can substantially deplete the pulse energy. For the channel with a maximum density at the center, after the laser pulse propagates through the channel for 1.5 cm, around 48% of the pulse energy is depleted. At the same time, 16 mJ of THz energy with a narrow spectrum

is generated. In this case, the laser pulse is not well guided since the channel no longer sustains a parabolic density profile in the transverse plane. For the channel with a density maximum at the lateral edges, the laser pulse can be well guided and most of the pulse energy is depleted into the channel instead of lateral leaking. Simulation result shows a fixed driver pulse (0.55 J) with spot size of 15 μm and pulse duration of 15 fs excites approximately 37.8 mJ of THz radiation in a 1.5 cm corrugated plasma waveguide with on axis average density of 1.4×10^{18} cm^{-3}, conversion efficiency exceeding 8% can be achieved in this case.

Bibliography

[1] M. Sherwin, C. Schmuttenmaer, and P. Bucksbaum, in *Report of a DOE-NSF-NIHWorkshop, Arlington, VA, 2004 (unpublished)*, Vol. 12 (2004) p. 14.

[2] M. C. Nuss and J. Orenstein, in *Millimeter-Wave Spectroscopy of Solids*, edited by G. Gruener Springer Verlag, Heidelberg, 1997, and references therein.

[3] D. M. Mittleman, R. H. Jacobsen, and M. C. Nuss, IEEE J. Sel. Top. Quantum Electron. **2**, 679 (1996).

[4] D. M. Mittleman, M. Gupta, R. Neelamani, R. G. Baraniuk, J. V. Rudd, and M. Koch, Applied Physics B: Laser and Optics **68**, 1085 (1999).

[5] M. C. Kemp, P. Taday, B. E. Cole, J. Cluff, A. J. Fitzgerald, and W. R. Tribe, in *AeroSense 2003* (International Society for Optics and Photonics, 2003) pp. 44–52.

[6] K. Kawase, Optics and photonics news **15**, 34 (2004).

[7] B. Ferguson and X. C. Zhang, Nat. Materials **1**, 26 (2002).

[8] D. Dragoman and M. Dragoman, Progress in Quantum Electronics **28**, 1 (2004).

[9] W. R. Tribe, D. A. Newnham, P. F. Taday, and M. C. Kemp, in *Integrated Optoelectronic Devices 2004* (International Society for Optics and Photonics, 2004) pp. 168–176.

[10] Y. P. Gousev, I. Altukhov, K. Korolev, V. Sinis, M. Kagan, E. Haller, M. Odnoblyudov, I. Yassievich, and K.-A. Chao, Appl. Phys. Lett. **75**, 757 (1999).

[11] B. S. Williams, S. Kumar, Q. Hu, and J. L. Reno, Optics Express **13**, 3331 (2005).

[12] H. Hamster, A. Sullivan, S. Gordon, W. White, and R. W. Falcone, Phys. Rev. Lett. **71**, 2725 (1993).

[13] H. Hamster, A. Sullivan, S. Gordon, and R. Falcone, Phys. Rev. E **49**, 671 (1994).

[14] T. Nakazato, M. Oyamada, N. Niimura, S. Urasawa, O. Konno, A. Kagaya, R. Kato, T. Kamiyama, Y. Torizuka, T. Nanba, Y. Kondo, Y. Shibata, K. Ishi, T. Ohsaka, and M. Ikezawa, Phys. Rev. Lett. **63**, 1245 (1989).

[15] U. Happek, A. J. Sievers, and E. B. Blum, Phys. Rev. Lett. **67**, 2962 (1991).

[16] E. Budiarto, J. Margolies, S. Jeong, J. Son, and J. Bokor, IEEE J. Sel. Top. Quantum Electron. **32**, 1839 (1996).

[17] C. Vicario, A. V. Ovchinnikov, S. I. Ashitkov, M. B. Agranat, V. E. Fortov, and C. P. Hauri, Opt. Lett. **39**, 6632 (2014).

[18] X. Wu, C. Zhou, W. R. Huang, F. Ahr, and F. X. Kärtner, Opt. Express **23**, 29729 (2015).

[19] J. A. Fülöp, Z. Ollmann, C. Lombosi, C. Skrobol, S. Klingebiel, L. Pálfalvi, F. Krausz, S. Karsch, and J. Hebling, Opt. Express **22**, 20155 (2014).

[20] W. P. Leemans, C. G. R. Geddes, J. Faure, C. Tóth, J. van Tilborg, C. B. Schroeder, E. Esarey, G. Fubiani, D. Auerbach, B. Marcelis, M. A. Carnahan, R. A. Kaindl, J. Byrd, and M. C. Martin, Phys. Rev. Lett. **91**, 074802 (2003).

[21] K.-Y. Kim, A. Taylor, J. Glownia, and G. Rodriguez, Nat. Photonics **2**, 605 (2008).

[22] A. Gopal, S. Herzer, A. Schmidt, P. Singh, A. Reinhard, W. Ziegler, D. Brömmel, A. Karmakar, P. Gibbon, U. Dillner, T. May, H.-G. Meyer, and G. G. Paulus, Phys. Rev. Lett. **111**, 074802 (2013).

[23] L. Wartski, J. Marcou, and S. Roland, IEEE Transactions on Nuclear Science **20**, 544 (1973).

[24] T. Ludlam, E. Platner, V. Polychronakos, M. Deutschmann, W. Struczinski, C. Fabjan, W. Willis, I. Gavrilenko, S. Maiburov, A. Shmeleva, *et al.*, Nuclear Instruments and Methods **180**, 413 (1981).

[25] J. Van TIlborg, C. B. Schroeder, E. Esarey, and W. P. Leemans, Laser and Particle Beams **22**, 415 (2004).

[26] W. P. Leemans, J. Van Tilborg, J. Faure, C. G. R. Geddes, C. Tóth, C. B. Schroeder, E. Esarey, G. Fubiani, and G. Dugan, Phys. Plasmas **11**, 2899 (2004).

[27] C. B. Schroeder, E. Esarey, J. van Tilborg, and W. P. Leemans, Phys. Rev. E **69**, 016501 (2004).

[28] J. van Tilborg, C. B. Schroeder, C. V. Filip, C. Tóth, C. G. R. Geddes, G. Fubiani, R. Huber, R. A. Kaindl, E. Esarey, and W. P. Leemans, Phys. Rev. Lett. **96**, 014801 (2006).

[29] K. Y. Kim, J. H. Glownia, A. J. Taylor, and G. Rodriguez, Opt. Express **15**, 4577 (2007).

[30] K. Y. Kim, A. J. Taylor, J. H. Glownia, and G. Rodriguez, Nature Photonics **2**, 605 (2008).

[31] K. Y. Kim, Phys. Plasmas **16**, 056706 (2009).

[32] L. A. Johnson, J. P. Palastro, T. M. Antonsen, and K.-Y. Kim, Phys. Rev. A **88**, 063804 (2013).

[33] T. M. Antonsen, J. P. Palastro, and H. M. Milchberg, Phys. Plasmas **14**, 033107 (2007).

[34] A. J. Pearson, J. Palastro, and T. M. Antonsen, Phys. Rev. E **83**, 056403 (2011).

[35] Z.-M. Sheng, K. Mima, J. Zhang, and H. Sanuki, Phys. Rev. Lett. **94**, 095003 (2005).

[36] C. Miao, J. Palastro, and T. M. Antonsen, Phys. Plasmas **23**, 063103 (2016).

[37] C. Miao, J. P. Palastro, A. J. Pearson, and T. M. Antonsen, in *2015 40th International Conference on Infrared, Millimeter, and Terahertz waves (IRMMW-THz)* (2015) pp. 1–2.

[38] W. L. Kruer, in *The Physics of Laser Plasma Interactions* (Addison-Wesley, Redwood City, Cal., 1988) p. 39.

[39] E. Esarey, C. B. Schroeder, and W. P. Leemans, Rev. Mod. Phys. **81**, 1229 (2009).

[40] P. Mora and T. M. Antonsen Jr, Phys. of Plasmas **4**, 217 (1997).

[41] V. Ginzburg and I. M. Frank, Sov. Phys. JETP **16**, 15 (1946).

[42] H. Conrads and M. Schmidt, Plasma Sources Science and Technology **9**, 441 (2000).

[43] B. D. Layer, A. York, T. M. Antonsen, S. Varma, Y.-H. Chen, Y. Leng, and H. M. Milchberg, Phys. Rev. Lett. **99**, 035001 (2007).

[44] G. A. Hine, A. J. Goers, L. Feder, J. A. Elle, S. J. Yoon, and H. M. Milchberg, Opt. Lett. **41**, 3427 (2016).

[45] A. G. York, H. M. Milchberg, J. P. Palastro, and T. M. Antonsen, Phys. Rev. Lett. **100**, 195001 (2008).

[46] S. J. Yoon, J. P. Palastro, and H. M. Milchberg, Phys. Rev. Lett. **112**, 134803 (2014).

[47] S. J. Yoon, A. J. Goers, G. A. Hine, J. D. Magill, J. A. Elle, Y.-H. Chen, and H. M. Milchberg, Opt. Express **21**, 15878 (2013).

[48] J. P. Palastro, T. M. Antonsen, S. Morshed, A. G. York, and H. M. Milchberg, Phys. Rev. E **77**, 036405 (2008).

[49] S. J. Yoon, J. P. Palastro, D. Gordon, T. M. Antonsen, and H. M. Milchberg, Phys. Rev. ST Accel. Beams **15**, 081305 (2012).

[50] J. M. Dawson, Rev. Mod. Phys. **55**, 403 (1983).

[51] C. K. Birdsall and A. B. Langdonr, in *Plasma Physics via Computer Simulation* (McGraw-Hill, 1985).

[52] K. S. Yee *et al.*, IEEE Trans. Antennas Propag **14**, 302 (1966).

[53] C. D. Decker, W. B. Mori, and T. Katsouleas, Phys. Rev. E **50**, R3338 (1994).

[54] C. A. Coverdale, C. B. Darrow, C. D. Decker, W. B. Mori, K.-C. Tzeng, K. A. Marsh, C. E. Clayton, and C. Joshi, Phys. Rev. Lett. **74**, 4659 (1995).

[55] C. D. Decker, W. B. Mori, K. Tzeng, and T. Katsouleas, Phys. Plasmas **3**, 2047 (1996).

[56] S. V. Bulanov, F. Pegoraro, and A. M. Pukhov, Phys. Rev. Lett. **74**, 710 (1995).

[57] C. Benedetti, A. Sgattoni, G. Turchetti, and P. Londrillo, IEEE Trans. Plasma Sci. **36**, 1790 (2008).

[58] K. J. Bowers, B. Albright, L. Yin, B. Bergen, and T. Kwan, Phys. Plasmas **15**, 055703 (2008).

[59] R. A. Fonseca, L. O. Silva, F. S. Tsung, V. K. Decyk, W. Lu, C. Ren, W. B. Mori, S. Deng, S. Lee, T. Katsouleas, *et al.*, in *International Conference on Computational Science* (Springer, 2002) pp. 342–351.

[60] K. Amyx, in *Proceedings of the GPU Technology Conference, San Jose, California* (2012).

[61] J.-L. Vay, C. Geddes, E. Esarey, C. Schroeder, W. Leemans, E. Cormier-Michel, and D. Grote, Phys. Plasmas **18**, 123103 (2011).

[62] D. F. Gordon, IEEE Trans. Plasma Sci. **35**, 1486 (2007).

[63] D. F. Gordon, B. Hafizi, and M. H. Helle, Journal of Computational Physics **267**, 50 (2014).

[64] L. M. Gorbunov and A. A. Frolov, Plasma Physics Reports **32**, 850 (2006).

[65] C. Miao, J. P. Palastro, and T. M. Antonsen, in *Proceedings of 6th International Particle Accelerator Conference* (JACoW, WEPWA068, 2015) p. 2661.

[66] Z.-M. Sheng, K. Mima, and J. Zhang, Phys. Plasmas **12**, 123103 (2005).

[67] T. M. Antonsen, Phys. Plasmas **17**, 073112 (2010).

[68] T. M. Antonsen Jr and P. Mora, Phys. Rev. Lett. **69**, 2204 (1992).

[69] B. Shadwick, C. Schroeder, and E. Esarey, Phys. Plasmas **16**, 056704 (2009).

[70] C. Benedetti, F. Rossi, C. B. Schroeder, E. Esarey, and W. P. Leemans, Phys. Rev. E **92**, 023109 (2015).

[71] W. Zhu, J. P. Palastro, and T. M. Antonsen, Phys. Plasmas **20**, 073103 (2013).

[72] W. Zhu, J. P. Palastro, and T. M. Antonsen, Phys. Plasmas **19**, 033105 (2012).